약학박사 학위논문

Renal clearable zwitterionic cyclodextrin nanocarrier: Optimizing the structure for enhancing colorectal cancer targetability

신장 배설 가능한 양쪽이온성 사이클로덱스트린 나노 전달체: 대장암 표적성 향상을 위한 구조 최적화

2023 년 8 월

서울대학교 대학원

약학과 약제과학 전공

백 민 준

Renal clearable zwitterionic cyclodextrin nanocarrier: Optimizing the structure for enhancing colorectal cancer targetability

신장 배설 가능한 양쪽이온성 사이클로덱스트린 나노 전달체: 대장암 표적성 향상을 위한 구조 최적화

지도 교수 김 대 덕

이 논문을 약학박사 학위논문으로 제출함

2023 년 6 월

서울대학교 대학원

약학과 약제과학 전공

백 민 준

백민준의 약학박사 학위논문을 인준함

2023 년 7 월

위 원 장 _____ 정 석 재 _____ (인)

부위원장 _____ 이 우 인 _____ (인)

위 원 _____ 이 재 영 _____ (인)

위 원 _____ 김 기 택 _____ (인)

위 원 _____ 김 대 덕 _____ (인)

Abstract

Renal clearable zwitterionic cyclodextrin nanocarrier: Optimizing the structure for enhancing colorectal cancer targetability

Min-Jun Baek

Department of Pharmaceutical Sciences

The Graduate School

Seoul National University

The ultimate goal of tumor-targeted drug delivery system (DDS) is not only to maximize the retention of anticancer agents to tumor tissue, but also to minimize their off-target distribution to normal tissues. Since the enhanced permeability and retention (EPR) phenomenon was discovered in 1986, non-renal clearable size has long been the primary criterion in the design of tumor targeted nanoparticles (NPs). Recently, however, it has been reported that

non-renal clearable NPs were not able to efficiently deliver anticancer drugs to tumor (< 1%) and also caused severe accumulation of NPs in normal organs, including liver, lung and spleen. Since the off-target accumulation induces prolonged exposure of NPs and loaded anticancer agents to normal tissues, it could raise long-term toxicity concerns, which impede the clinical translation of the large NPs. Therefore, it is important to develop biocompatible nanocarriers that can enhance tumor targetability as well as reduce off-target accumulation of nanocarriers and/or loaded therapeutic agents. In this thesis work, β-cyclodextrin-based renal clearable organic nanocarriers was developed to address the major challenges of the conventional large NPs. Although cyclodextrin (CD)-based renal clearable nanocarriers have high potential for clinical translation in targeted cancer therapy, their optimal designs for enhanced tumor retention and reduced off-target accumulation have rarely been proposed. Therefore, optimum structure of renal clearable zwitterionic CD, hepatkis-(6-deoxy-6-((phenylboronic acid-tetraethyleneglycol-L-glutamic acid N^{α}-sulfobetaine)-octaethyleneglycol-caproamide))-β-cyclodextrin (PBA-(ZW)-CD), was developed for tumor selective drug delivery. Twenty CD derivatives harboring different charged moieties and spacers were synthesized, followed by screening based on their colloidal stability. The resulting five candidates were complexed with adamantyl sulfocyanine 7 and evaluated for biodistribution, through which PBA-(ZW)-CD was selected as the optimized structure. Then, PBA-(ZW)-CD inclusion complexes of doxorubicin and ulixertinib were fabricated, and

their enhanced tumor accumulation (vs. free doxorubicin, 2.0-folds; vs. free ulixertinib, 2.1-folds), facilitated elimination (vs. free doxorubicin, 15.2% remaining in the heart and below the detection limit (<200 ng g^{-1}) in muscle, respectively; vs. free UXT, 17.7% and 7.4% in the liver and kidney, respectively), and tumor penetration comparable to free drugs were verified *via* mass spectrometry (LC-MS/MS and MALDI-MSI). Improved antitumor efficacy of PBA-(ZW)-CD/drug-assisted combination therapy was demonstrated in heterotopic and orthotopic CRC models (vs. free drug combination, tumor size reduction by 52.0% and 76.2%, respectively), supporting PBA-(ZW)-CD could be a promising CRC-targeted nanoplatform.

Keywords: cyclodextrin, renal clearable, zwitterionic, tumor retention, off-target accumulation, colorectal cancer

Student Number: 2017-24147

Table of Contents

List of Tables

List of Figures

according to the method described in *2.3. biodistribution studies of CD derivatives.* In lateral view images, as the whole-body fluorescence signals gradually decreased, the kidney signals became dominant. Meanwhile, supine view images revealed that the fluorescence intensity gradually increased in the bladder, implying the renal excretion of SCy7-PBA-(ZW)-CD. (D) Cumulative urinary excretion of SCy7-PBA-(ZW)-CD exceeded 80% of the initial dose (ID) within 4 h, reaching 95.2 ± 5.2% ID at 24 h, suggesting the preferential renal clearance of PBA-(ZW)-CD. (E) In an *ex vivo* imaging study, the SCy7-PBA-(ZW)-CD signal was mainly observed in the kidneys with negligible signals (*i.e.*, autofluorescence level) detected in other organs, including the lungs, liver, and spleen at 120 h. Abbreviations: H, heart; Lu, lungs; Li, liver; Sp, spleen; Mu, muscles; S.I, small intestine; L.I, large intestine; and Ki, kidneys. (F) Kidney signals also decreased linearly (fluorescence intensity (a.u.) = –61.4 × elapsed time (h) + 9613.8; R^2 = 1.000), expected to reach the autofluorescence level within 136.3 h. Collectively, these results indicate that PBA-(ZW)-CD structure can evade mononuclear phagocyte system uptake (reduced distribution to the liver, lungs, and spleen), minimize the non-specific tissue binding, and be readily excreted *via* kidneys. 109

1. Introduction

1.1. Nanoparticle-based tumor targeted drug delivery system

In spite of emerging various medical therapies for cancer treatment, chemotherapy is still mainstay and a widely used option for most anticancer therapy, along with surgery, radiation therapy and immunotherapy [1-5]. However, cytotoxic chemotherapeutic drugs lack specificity and cause toxic side-effects to healthy tissues, which often limited the use of chemotherapeutic drugs [6-8]. Therefore, control of delivering chemotherapeutic drugs to tumor with high selectivity have been a ultimate goal of tumor-targeted drug delivery system. Ever since it has been discovered that macromolecules and nanosized particles can be preferentially accumulated in tumors by enhanced permeability and retention (EPR) effect, the EPR effect started the avenue of nanomedicine in the field of tumor-targeted delivery system [9]. Design of conventional EPR-based nanoparticles (NPs) requires non-renal clearable size to ensure long blood circulation time and selective tumor accumulation through micron-sized gaps that exist between tumor endothelial cells [10]. Traditionally, it has been considered that long systemic circulation of NPs with high plasma concentration could increase accumulation of NPs to tumor by enhanced permeability effect, while limit extravasation of NPs from normal blood

vessels, thereby reducing exposure of loaded drugs to normal tissues. Based on the EPR theory, numerous drug delivery systems (DDSs) in nano-scale (10–200 nm), including liposomes, mesoporous silica NPs, gold NPs, iron NPs, polymeric NPs, have been developed over the past three decades to control delivery of anticancer drugs to solid tumors [11-15]. A liposome-encapsulated anthracyclines formulation (Doxil®, 80-100 nm) is one of clinically approved NPs which is based on conventional EPR theory. Actually, the liposomal formulation increased plasma half-life of doxorubicin and reduced cardiotoxicity of doxorubicin (DOX) by changing pharmacokinetics and tissue distribution of DOX [16]. The clinical approval of Doxil® hold great promise for a broad range of NPs for antitumor therapy. Recently, however, the EPR-based NPs faced several critical challenges that should be carefully addressed for clinical application.

1.2. Limitations of EPR-based tumor targeted nanoparticles

Although numerous EPR-based NPs have repeatedly been confirmed EPR effect in preclinical tumor xenografted animal models, the majority of anticancer nanomedicines have failed to prove enhanced antitumor efficacy and reduced toxicity in clinical trials. And it has been reported that the efficacy and toxicity profiles of the clinically approved nanomedicines are inconsistent in human patients [17]. These inconsistent results provoked

vigorous discussion regarding importance and existence of EPR effects in human patients. Also, questions to extravasation mechanism and effectiveness of conventional large NPs have been strongly raised [18-21]. In addition to skepticism of EPR effect, the EPR-based conventional NPs showed several limitations, hindering clinical translation of NPs, in preclinical animal study.

Low tumor targeting efficiency is one of the major limitations of the EPR-based conventional NPs. A recent meta-analysis of preclinical data revealed that only 0.7% (median) of the intravenously injected NPs accumulated in tumor tissue [19]. Although the tumor targeting efficiency of the NPs could be significantly higher than conventional formulations of chemotherapeutics, the absolute tumor targeting efficiency is far from satisfactory [22]. For the EPR-mediated NPs accumulation to tumor, blood vessels of the tumor area should be leaky. However, many types of tumors, especially human tumors, are known to have insufficient leakiness, resulting limited extravasation of NPs into tumor tissue [23-25].

Limited penetration into deep tumor site is another major challenge of conventional large NPs [26]. After extravsation of NPs from blood vessels, NPs should be penetrated into the tumor cores to reach cancer cells distant from the vascularature. However, elevated interstitial fluid pressure (IFP) and solid stress caused by high cellular density and dense extracellular matrix (ECM) prevent diffusion of large NPs in tumor microenvironment [27]. It is well known that extravasated NPs are mainly accumulated in the peripheral

area of tumors, and large NPs showed limited tumor penetration compared to smaller counterparts [28]. Poor penetration of the large NPs may cause drug resistance and tumor recurrence, as well as compromise the efficacy of anticancer agents [29].

One critical limitation related clinical application of the EPR-based conventional NPs is off-target accumulation. Since only less than 1% of intravenously administered NPs reach to tumor and the NPs are barely excreted from the body, most of injected NPs remain in the body [19, 30]. In general, for NPs larget than the kidney filtration threshold, the elimination is performed by tissue-resident macrophages, monocytes, and dendritic cells belonging to the mononuclear phagocyte system (MPS) [31]. Although the steric barrier created by PEGylation or zwitterionization can enhancing blood circulation time of NPs by stealth effect, the anti-fouling polymers does not specifically prevent size-dependent interaction of NPs with the MPS [30, 32, 33]. The MPS uptake not only decrease the plasmal concentration of NPs, but also induce severe accumulation of NPs and loaded cytotoxic cargos in normal organs. Since the accumulation of NPs can cause long-term toxicity concerns, off-target effect is considered as the major hurdle for NPs' clinical application [34]. Actually, despite remarkable progress in the field of tumor targeted NPs, only a few injectable medical nanomedicines are currently available for cancer diagnosis and treatment. This is mainly due to potential toxicity concerns caused by off-target accumulation and long-term retention of NPs in normal organs [35-40]. The uncontrolled distribution profiles are

mainly is attributed to the non-renal clearable particle size, which is a primary prerequisite of conventional EPR-based NPs [35, 36, 39-41]. The limitations inspired paradigm shift from non-renal clearable NPs to renal clearable nanocarriers for tumor-targeted imaging and drug delivery [31, 42-48].

1.3. Renal clearable nanocarriers for drug delivery

Elimination of NCs from body is important for clinical application of nanomaterials. The excretion of NCs in reasonable time can reduce exposure of NCs to normal cells, thereby prevents tissue damage and toxicity. Major excretion pathways that can be utilized for NCs excretion are renal and hepatic pathway. Compared to slow hepatobiliary excretion (weeks to months), renal excretion is preferred because of rapid elimination (hours to days) with minimum cellular internalization and metabolism [36]. With a limited clinical translation rate of old-school NCs, there was a paradigm shift towards renal clearable ultrasmall nanoplatform [31, 42-48], which has several advantages compared to its non-renal clearable counterpart: (1) rapid elimination of NCs distributed to off-target tissue *via* urinary excretion, (2) high tumor vascular permeability, and (3) highly reduced uptake by mononuclear phagocyte system (MPS) [28, 31, 49]. These favorable features allow high-dose administration of cytotoxic cargo molecules with increased tumor selectivity, resulting in enhanced efficacy and minimized adverse

effects [28, 31, 50-54]

However, renal clearable NCs are neither free from drawbacks that hamper clinical translation. One major issue is residual toxicity caused by trace amounts of injected NCs [55, 56]. In case of NPs made by inorganic materials, even though the size of NPs is smaller than kidney filtration threshold, they are not excreted completely through urinary system and retained in the body for several months to years, which raised long term toxicity concerns [36]. Notwithstanding the short-term biocompatibility, long-term or lifetime exposure to undegradable foreign materials (*e.g.*, silica and metal) discourages clinical use [57, 58]. Therefore, a non-toxic and biodegradable organic material, β-cyclodextrin, was used for developing renal-clearable nanocarrier system in this thesis.

1.4. Cyclodextrin-based nanocarriers for tumor targeted delivery

Cyclodextrins (CDs) are cyclic oligosaccharides which consist of at least 6-glucose units linked with α-(1, 4) glycosidic bonds [59]. Natural CDs comprise α-, β-, and γ-CDs which have 6, 7, or 8 glucopyranose units in one molecule, respectively. The nature CDs can be produced by enzymatic degradation of starch [60]. The CDs are water-soluble by its hydrophilic outer surfaces, and the hydrophobic inner cavity of CD allows the CDs to interact with various hydrophobic molecules, forming noncovalent inclusion

complexes [61]. The CDs-guest complexation involves the removal of solvent molecules from hydrophobic cavity followed by replacement of guest molecules by forming Vander Waal forces and hydrogen bond interactions [62]. The formation of inclusion complexes can change the physicochemical and biological properties of guest molecules [63]. Since three nature CDs consist of different number of glucopyranose units, each CD has different cavity size. The cavity size of α-CD is insufficient to interact with many small chemical drugs, and γ-CD has weaker affinity to guest molecules than β-CD. Therefore, β-CD derivatives have been widely used as pharmaceutical excipients for preparing CD/guest inclusion complexes [64-68]. However, pristine β-CD has a lower solubility compared with α- and γ-CD due to the strong internal hydrogen bond interaction that created by the secondary hydroxyl groups [69]. In order to improve the solubility and toxicity of pristine β-CD, hydroxypropyl and sulfonate group can be chemically conjugated to the β-CD. The resulting biocompatible hydroxyproyl (HP)-β-CD and sulfobutylether (SBE)-β-CDs are widely used as excipients for parenteral delivery system [70].

In addition to unique physicochemical properties and biocompatibility, many functional groups on CD allows chemical modification to CD molecules [71]. The pristine β-CDs have three types of hydroxyl functional groups, including reactive 6-OH groups on the upper rim and less accessible acidic 2-OH and 3-OH groups on the lower rim. The different reactivity of the hydroxyl groups enables regioselective

modification of β-CDs [72]. Over the past few decades, a great effort has been devoted to developing β-CD-based drug delivery system through various chemical modifications [52, 64, 68, 73-76]. The size of β-CD derivatives can be adjusted from ~1.6 nm (pristine β-CDs) to several hundred nanometers by optimizing synthesis method. The β-CD derivatives, especially smaller than kidney filtration threshold (6~8 nm), can be efficiently cleared from systemic circulation through urinary excretion system [77-79]. Based on highly renal clearable property of β-CD unit, several renal clearable NPs or optical probes have been recently developed [78, 80, 81].

As one drug delivery system for anticancer therapy, renal-clearable NCs, namely H-Dots, composed of biodegradable organic materials including β-cyclodextrin (CD)-grafted polylysine, were reported by Kang et al., demonstrating efficient tumor-targeted drug delivery with low background tissue retention [53, 82]. However, the tumor selectivity of these NCs is mainly due to their significantly reduced residence time in normal tissues, not the augmented tumor-homing ability. This suggests that by extending the tumor retention of renal-clearable organic NCs, much higher tumor selectivity can be achieved.

As a one strategy for enhancing tumor-homing ability of NCs, tumor targeting ligands can be introduced to renal clearable NC structure. Although targeting ligands can improve cellular internalization of NCs [83, 84], this so-called active targeting strategy does not always ensure improved selectivity, unexpectedly inducing opsonization and consequent non-target accumulation,

primarily *via* MPS uptake [85-90]. Therefore, delicate tailoring of the optimal NC structure is required for clinical success, balancing the targeting efficiency and off-target accumulation of renal-clearable NCs, which has yet to be investigated.

1.5. Renal clearable cyclodextrin nanoplatforms for anticancer drug delivery to colorectal cancer

Colorectal cancer (CRC) is the third most commonly diagnosed cancer, with the second highest mortality rate and a constantly increasing incidence rate [91]. Although optimal surgical resection is a basic treatment for patients with locoregional CRC, there is still high risk of tumor recurrence after surgery [92]. Therefore adjuvant chemotherapy (ACT) after surgical resection is a current mainstay of Stage II and III CRC treatment, resulting in improved overall survival and disease-free survival [93]. Despite its effectiveness, ACT is often limited by the severe toxicity of chemotherapeutic agents, such as 5-fluorouracil, irinotecan, and oxaliplatin [94, 95]. To avoid the adverse effects of single-drug therapy, combination therapy with small doses of various drugs, such as FOLFIRI, FORFOX, CAPEOX, Optimox, and CONcePT, has been established as the standard regimen for CRC treatment to attain synergistic anticancer efficacy. However, such drug amalgamation still has not fully resolved the toxicity concerns [96], which warrants the development of

innovative modalities to improve or replace existing ACT regimens [97].

In this work, novel designs of renal clearable CD nanoplatforms were investigated to promote tumor retention, without causing any off-target accumulation of imaging and therapeutic agents in CRC treatment. The relationship between structural design and target-to-background selectivity was elucidated by synthesizing 20 CD derivatives by varying the structures of the spacer and functional groups. Systematic evaluation of the CD library in terms of colloidal stability and *in vivo* distribution revealed a fine-tuned zwitterionic CD derivative, hepatkis-(6-deoxy-6-((phenylboronic acid-tetraethyleneglycol-l-glutamic acid N^{α}-sulfobetaine)-octaethyleneglycol-caproamide))-β-cyclodextrin (PBA-(ZW)-CD), as the optimal structure for targeted CRC therapy. Forming stable inclusion complexes, a fluorophore (adamantyl sulfocyanine 7) and two chemotherapeutic agents (doxorubicin and ulixertinib) were successfully loaded into PBA-(ZW)-CD for CRC imaging and treatment, respectively. Moreover, thorough evaluations were performed to verify whether these CD nanoplatforms facilitated the (1) selective delivery of imaging and chemotherapeutic agents to CRC tissues with substantially reduced off-target accumulation, (2) rapid clearance of NCs *via* the renal route, and (3) improvement of the efficacy and safety of CRC treatment.

2. Materials and Methods

2.1. Materials

O-(benzotriazol-1-yl)-N,N,N',N'-tetramethyluronium hexafluorophosphate (HBTU), N-([dimethylamino]-1H-1,2,3-triazolo-[4,5-b]pyridin-1-ylmethylene)-N-methylmethanaminium hexafluorophosphate N-oxide (HATU), 3-aminophenylboronic acid, 6-(Boc-amino)caproic acid, lithium hydroxide, trifluoroacetic acid (TFA), triethylamine (TEA), N,N-diisopropylethylamine (DIPEA), N-(3-dimethylaminopropyl)-N'-ethylcarbodiimide hydrochloride (EDC·HCl), 2-(N-morpholino)ethanesulfonic acid (MES), succinic anhydride, betaine hydrochloride, glycolic acid, alizarin red S (ARS), 3-acetamindophenylboronic acid, fluorescamine, and l-serine were purchased from Sigma-Aldrich Co. (St. Louis, MO, USA). N-Boc-l-glutamic acid α-methyl ester was purchased from Santa Cruz Biotechnology (Dallas, TX, USA). t-Boc-N-amido-PEG_n-acids (n = 4, 8, and 12) were purchased from BroadPharm (San Diego, CA, USA). Heptakis-(6-amino-6-deoxy)-β-cyclodextrin (CD) heptahydrochloride was obtained from Cyclodextrin Shop (Tilburg, Netherlands). Doxorubicin (DOX) free base was purchased from MedKoo Biosciences, Inc. (Morrisville, NC, USA). Ulixertinib (UXT) was purchased from MedChemExpress (Monmouth Junction, NJ, USA).

Deuterium oxide (D_2O) and dimethyl sulfoxide-d_6 (DMSO-d_6) were purchased from Cambridge Isotope Laboratories (Tewksbury, MA, USA). Dialysis membranes (Spectra/Por 7 Dialysis Tubing; molecular weight cut-off [MWCO]: 1 kDa) were obtained from Repligen Corporation (Waltham, MA, USA). Roswell Park Memorial Institute (RPMI) 1640 cell culture medium, penicillin–streptomycin, and fetal bovine serum (FBS) were obtained from Thermo Fisher Scientific (Waltham, MA, USA). N-hydroxysuccinimide esters of sulfocyanine 5 and 7 (SCy5-NHS and SCy7-NHS, respectively) were purchased from LumiProbe (Hunt Valley, MD, USA). All other reagents used were of analytical grade.

2.2. Synthesis and characterization of CD derivatives

Nuclear Magnetic Resonance (NMR) Spectroscopy and Mass Spectrometry (MS)

Proton and rotating frame Overhauser enhancement spectroscopy (ROESY) NMR spectra were acquired using a JNM-ECZ400s (JEOL, Tokyo, Japan). Mass spectra of compounds with molecular weights lower than 1,000 Da were obtained using an Agilent Technologies 6430 Triple Quad LC/MS system (electrospray ionization [ESI]-MS; Agilent Technologies, Santa Clara, CA, USA). Mass spectra of the CD derivatives were recorded using a Voyager-

DE STR Biospectrometry Workstation (matrix-assisted laser desorption/ionization time-of-flight MS; Applied Biosystems Inc., Waltham, MA, USA) with 2,5-dihydroxybenzoic acid (DHB) as the matrix.

*Synthesis of Compounds **1** and **3***

For the synthesis of compound **1**, *N*,*N*-dimethylglycine ethyl ester (1,700 μL, 2.0 mmol) was dissolved in anhydrous dichloromethane (DCM), followed by the addition of 1,3-propane sultone (1600 mg, 13.1 mmol). The mixture was stirred at room temperature (RT) for 48 h under a nitrogen atmosphere. The mixture was filtered and the residue was washed with DCM to yield **1** as a white solid. The product was dried under reduced pressure (88% yield) and used directly in the next step without further purification. ^{1}H-NMR (400 MHz, D_2O, δ): 4.19 (s, 2H), 4.17 (m, 2H), 3.59 (m, 2H), 3.17 (s, 6H), 2.83 (t, 2H), 2.10 (m, 2H), and 1.15 (t, 3H). ESI-MS: *m/z* 254.1 $[M + H]^+$. Similarly, methyl 3-(dimethylamino)propionate (1,717 μL, 12.0 mmol) was dissolved in anhydrous DCM, and 1,3-propane sultone (1,600 mg, 13.1 mmol) was added to prepare compound **3**. The mixture was stirred at RT for 48 h under a nitrogen atmosphere. The product was filtered, washed with DCM, and dried under vacuum before use (86% yield). ^{1}H-NMR (400 MHz, D_2O, δ): 3.6 (s, 3H), 3.56 (t, 2H), 3.35 (m, 2H), 2.98 (s, 6H), 2.84 (m, 4H), and 2.09 (m, 2H). ESI-MS: *m/z* 254.1 $[M + H]^+$.

*Synthesis of Compounds **2** and **4***

Compounds 2 and 4 were prepared by the ester hydrolysis of 1 and 3, respectively. Briefly, 1 or 3 dissolved in double-deionized water (DDW) was added with 2 equivalents of LiOH powder and stirred for 4 h. The completion of the reaction was confirmed using ESI-MS. After neutralizing the reaction mixture with 1 mol L–1 aqueous HCl, the products were directly used as zwitterionic moieties without further purification. ESI-MS: m/z 226.0 [M + H]+ for 2 and m/z 240.1 [M + H]+ for 4.

*Synthesis of Compound **5***

N-Boc-L-glutamic acid α-methyl ester (1,305 mg, 5.0 mmol) and HATU (2,298 mg, 6.0 mmol) were dissolved in anhydrous *N*,*N*-dimethylformamide (DMF). The mixture was added with DIPEA (3,040 μL, 17.5 mmol) and stirred for 30 min, to which 3-amino phenylboronic acid monohydrate (1,155 mg, 7.5 mmol) dissolved in anhydrous DMF was added and stirred for 30 h at RT under a nitrogen atmosphere. The mixture was then diluted with DCM and washed thrice with 0.5 mol L^{-1} aqueous HCl and DDW. The organic layer was dried over $MgSO_4$, filtered, and vacuum-dried to obtain compound **5** as a white solid (yield: 73%). ^{1}H-NMR (400 MHz, DMSO-d_6/D_2O, δ): 7.64 (1H, s), 7.47 (1H, d), 7.37 (1H, d), 7.25 (1H, t), 3.94 (1H, m), 3.55 (3H, s), 2.32 (2H, t), 1.98 (1H, m), 1.82 (1H, m), and 1.22 (9H, s).

*Synthesis of Compound **6***

Compound **5** (1,387 mg, 3.65 mmol) was dissolved in 40 mL of methanol/DDW (50:50, v/v), added to LiOH powder (175 mg, 7.3 mmol), and stirred for 4 h. The mixture was neutralized by adding 1 mol L^{-1} aqueous HCl and dried under reduced pressure. The resulting powder was dissolved in DDW and washed thrice with DCM to remove the non-polar impurities. The water layer was then acidified by adding 1 mol L^{-1} aqueous HCl and extracted with ethyl acetate. The organic layer was dried over $MgSO_4$, filtered, and freeze-dried to obtain the acid form of compound **6** as a white solid (yield: 69%). ^{1}H-NMR (400 MHz, DMSO-d_6/D_2O, δ): 7.72 (s, 1H), 7.55 (d, 1H), 7.37 (d, 1H), 7.22 (t, 1H), 3.78 (m, 1H), 2.26 (t, 2H), 1.95 (m, 1H), 1.75 (m, 1H), and 1.27 (s, 9H). ESI-MS: *m/z* 365.1 $[M - H]^-$.

*Synthesis of Compound **7***

t-Boc-*N*-amido-PEG_4-acid (1,000 mg, 2.74 mmol) and HATU (1,249 mg, 3.29 mmol) were dissolved in anhydrous DMF. DIPEA (1,670 μL, 9.6 mmol) was added to the reaction mixture. After 30 min of stirring, 3-amino phenylboronic acid monohydrate (637 mg, 4.11 mmol) was added and stirred for 30 h at RT under a nitrogen atmosphere. The purification step was the same as that used for the *Synthesis of Compound **5***, yielding **7** as a yellow

liquid (yield: 84%). ^{1}H-NMR (400 MHz, DMSO-d_6, δ): 9.82 (s, 1H), 7.10-7.95 (m, 6H), 6.7 (s, 1H), 3.65 (m, 2H), 3.43-3.47 (s, 12H), 3.12 (s, 1H), 3.0 (m, 2H), 2.65 (s, 2H), 2.50 (m, 2H), and 1.32 (s, 9H).

*Synthesis of Compound **8***

Compound **7** (1,110 mg, 2.3 mmol) dissolved in DCM (15 mL) was mixed with TFA (15 mL) in an ice bath, and the mixture was further stirred at RT for 1 h. When the reaction was complete, as monitored using TLC (DCM:MeOH = 10:1, v/v), the solvent was removed under reduced pressure. The evaporated residue was washed thrice with cold ether (20 mL) and dried under vacuum. The yellow solid product was directly used in the next step without further purification.

*Synthesis of Compound **9***

DIPEA (973 µL, 5.6 mmol) was added to *N*-Boc-l-glutamic acid α-methyl ester (417 mg, 1.6 mmol) and HATU (760 mg, 2 mmol), dissolved in anhydrous DMF, and the mixture was stirred for 30 min. Compound **8** (994 mg, 2 mmol), dissolved in anhydrous DMF, was added to the reaction mixture and stirred for 30 h at RT under a nitrogen atmosphere. The purification procedure was the same as that used for the *Synthesis of Compound **5***, which yielded **9** as a yellow liquid (75% yield). ^{1}H-NMR (400 MHz, DMSO-$_{d6}$/D_2O,

δ): 7.73 (s, 1H), 7.57 (d, 1H), 7.39 (d, 1H), 7.22 (t, 1H), 3.87 (m, 1H), 3.64 (t, 2H), 3.55 (s, 3H), 3.41-3.45 (m, 12H), 3.32 (t, 2H), 3.11 (t, 2H), 2.50 (m, 2H), 2.07 (t, 2H), 1.84 (m, 1H), 1.49 (m, 1H), and 1.28 (s, 9H).

*Synthesis of Compound **10***

Compound **9** (750 mg, 1.2 mmol) was dissolved in 40 mL of methanol/DDW (50:50, v/v), and LiOH powder (57.6 mg, 2.4 mmol) was added. After the reaction was completed, monitored via TLC (DCM:MeOH = 10:1, v/v), the mixture was neutralized by adding 1 mol L^{-1} aqueous HCl and dried under reduced pressure. The resulting product was reconstituted with DDW and washed thrice with DCM to remove the non-polar impurities. Next, the water layer was acidified by adding 1 mol L^{-1} aqueous HCl, from which the acidic form of the product was extracted with ethyl acetate. The organic layer was dried over $MgSO_4$, filtered, and evaporated under vacuum to obtain compound **10** as a yellow liquid (yield: 69%). ^{1}H-NMR (400 MHz, DMSO-d_6/D_2O, δ): 7.73 (s, 1H), 7.58 (d, 1H), 7.39 (d, 1H), 7.22 (t, 1H), 3.80 (m, 1H), 3.63 (t, 2H), 3.41–3.45 (m, 12H), 3.31 (t, 2H), 3.11 (t, 2H), 2.50 (m, 2H), 2.09 (t, 2H), 1.85 (m, 1H), 1.67 (m, 1H), and 1.28 (s, 9H). ESI-MS: *m/z* 612.2 $[M - H]^-$.

General procedure for Boc deprotection of CD intermediates

Boc-protected intermediate compounds were added to acetonitrile/TFA (50:50, v/v) and stirred for 1.5 h at RT. The resulting solution was concentrated under reduced pressure and dialyzed against MeOH/DDW (90:10, v/v) for 12 h using a dialysis membrane (MWCO: 1 kDa; Cellu·Sep, Membrane Filtration Products, Inc., Seguin, TX, USA). The dialysis product was dried under vacuum.

General procedure for HBTU amide coupling

A carboxylic-acid-containing compound (1.2 equiv.) and HBTU (1.5 equiv.) were dissolved in 5 mL of anhydrous DMF. DIPEA (4.2 equiv.) was then added to the mixture and stirred for 30 min at RT. Amine-containing compounds (1 equiv.) dissolved in anhydrous DMSO was added to the reaction mixture, followed by stirring at RT for 48 h under nitrogen atmosphere. The resulting solution was dialyzed against MeOH/DDW (90:10, v/v) for 60 h using a dialysis membrane (MWCO: 1 kDa; Cellu·Sep, Membrane Filtration Products, Inc.).

*Synthesis of Compounds **11** and **12***

Compound **11** was prepared by conjugating compound **6** to heptakis (6-deoxy-6-amino)-β-cyclodextrin heptahydrochloride, using the *General procedure for HBTU amide coupling*. Boc of **11** was then deprotected

according to the *General procedure for boc deprotection of CD intermediates*, which yielded compound **12** as a yellow solid (yield: 61%).

*Synthesis of Compounds **13**–**20***

Compounds **13** and **14** were prepared by conjugating heptakis (6-deoxy-6-amino)-β-cyclodextrin heptahydrochloride and *t*-Boc-*N*-amido-PEG_n-acid (n = 4 and 8, respectively), using the general procedure for HBTU coupling. Boc groups of **13** and **14** were removed according to the *General procedure for boc deprotection of CD intermediates* to yield TFA salts of **15** and **16**, respectively, which were used in the next step without further purification. Compounds **17** and **18** were prepared by conjugating **6** with **15** and **16**, respectively, using the *General procedure for HBTU amide coupling*. Boc groups of **17** and **18** were deprotected using the method described above, resulting in compounds **19** and **20**, respectively.

*Synthesis of Compounds **21–26***

Compound **21** was prepared by conjugating heptakis (6-deoxy-6-amino)-β-cyclodextrin heptahydrochloride and 6-(Boc-amino)hexanoic acid, using the *General procedure for HBTU amide coupling*. Then, **22** was obtained by deprotecting the Boc groups of **21**, following the *General procedure for Boc deprotection of the CD intermediates*. *t*-Boc-*N*-amido-PEG_n-acid (n = 8 and

12) was conjugated to **22** using the *General procedure for HBTU amide coupling* to yield **23** and **24**. Compounds **25** and **26** were prepared by the removal of Boc groups from **23** and **24**, respectively, according to the *General procedure for Boc deprotection of CD intermediates*.

*Synthesis of Compounds **27–30***

Compound **27** was synthesized by introducing **6** into **26,** following the *General procedure for HBTU amide coupling*. Similarly, **29** was prepared by conjugating **10**–**25**. Then, the Boc groups of **27** and **29** were removed using the *General procedure for Boc deprotection of CD intermediates* to yield **28** and **30**, respectively.

*General procedure for sulfobetaine conjugation (Synthesis of **CD 1**, **2**, **6**, **7**, **11**, **12**, **16**, and **17**)*

Sulfobetaine (compound **2** or **4**; 14 equiv.), EDC·HCl (21 equiv.), NHS (21 equiv.), and amine-containing CD derivative (compound **12**, **19**, **20**, or **30**; 1 equiv.) were dissolved in a co-solvent of MES buffer (pH 6) and DMSO (70:30, v/v) and stirred at 40 °C for 24 h. The pH of the reaction mixture was adjusted to 7 and stirred at the same temperature for another 24 h. The resulting solution was dialyzed against MeOH/DDW (50:50, v/v) using a

dialysis membrane (MWCO: 1 kDa; Cellu·Sep, Membrane Filtration Products, Inc.) for 60 h.

*General procedure for amidation of succinic anhydride (Synthesis of **CD 3**, **8**, **13**, and **18**)*

Succinic anhydride (10 equiv.), TEA (20 equiv.), and amine-containing CD derivative (compound **12**, **19**, **20**, or **30**; 1 equiv.) was dissolved in anhydrous DMSO and stirred at RT for 48 h under a nitrogen atmosphere. The resulting solution was subjected to dialysis against MeOH/DDW (90:10, v/v) for 60 h using a dialysis membrane (MWCO: 1 kDa; Cellu·Sep, Membrane Filtration Products, Inc.).

*General procedure for betaine hydrochloride or glycolic acid conjugation (Synthesis of **CD 4**, **5**, **9**, **10**, **14**, **15**, **19**, and **20**)*

Betaine hydrochloride and glycolic acid (10 equiv.), EDC·HCl (12 equiv.), NHS (12 equiv.), TEA (30 equiv.), and amine-containing CD derivative (compound **12**, **19**, **20**, or **30**; 1 equiv.) were dissolved in anhydrous DMSO and stirred at RT for 48 h under a nitrogen atmosphere. The resulting solution was purified using the dialysis method described in the *General procedure for amidation of succinic anhydride* section.

Turbidimetric analysis of CD derivatives

The colloidal stability of CD derivatives in phosphate-buffered saline (PBS) or FBS was evaluated using a turbidity assay. Briefly, each CD derivative powder sample was added to PBS or FBS to prepare a 1 mmol L^{-1} solution. The degree of aggregation was evaluated by measuring the absorbance at 600 nm (OD_{600}) using a UV-vis spectrophotometer (EMax Precision Microplate Reader, Molecular Devices Corp., Sunnyvale, CA, USA) [98]. The OD_{600} values of the PBS and FBS solutions were normalized to that of the DDW/DMSO (50:50, v/v) solution of the corresponding CD derivatives to correct the molecular absorbance.

Degree of phenylboronic acid conjugation

CD derivatives dissolved in MeOH (0.5 mg mL^{-1} for compound **11** and 1 mg mL^{-1} for compounds **17**, **18**, **27**, and **29**; 100 µL) was vortex-mixed with PBS (100 µL) and then with ARS in DMSO (1 mmol L^{-1}, 100 µL) for 1 h. Similarly, 3-acetamidophenylboronic acid solutions (0.05–0.3 mg mL^{-1} in MeOH), prepared as standard samples, were vortex-mixed with PBS and ARS solution for 1 h. An aliquot (100 µL) of each mixture was transferred to a 96-well plate, and the absorbance at 465 nm was measured using a UV-vis spectrophotometer (EMax Precision Microplate Reader, Molecular Devices Corp.).

Quantification of residual amines after charged moiety conjugation

Each CD derivative solution in PBS (1 mg mL^{-1}, 200 μL) was vortex-mixed with the same volume of fluorescamine solution in DMSO (2.5 mg mL^{-1}) for 1 h. L-Serine dissolved in PBS (5–100 nmol mL^{-1}) was prepared as a standard sample. Similarly, each L-serine solution was vortex-mixed with the same volume of fluorescamine solution for 1 h. Fluorescence intensity of each sample was measured using a SpectraMax M5 multimode microplate reader (λex/λem = 395/495 nm; Molecular Devices Corp.).

2.3. Biodistribution studies of CD derivatives

Preparation of near-infrared fluorescence (NIRF) dye-loaded inclusion complexes

Adamantyl sulfocyanine 7 (ACy7) was synthesized by adding 1-adamantylamine (1.1 mg, 0.007 mmol) and TEA (1 μL, 0.007 mmol) to SCy7-NHS (5 mg, 0.0056 mmol) dissolved in anhydrous DMSO. The mixture was monitored by ESI-MS and stirred at RT until SCy7-NHS was completely consumed, followed by 48 h of lyophilization to remove excess volatile impurities including 1-adamantylamine and TEA. The lyophilized

product was washed with acetonitrile and dried under vacuum to yield ACy7 (yield: 82%). ACy5 was synthesized using the same method as described above, except that SCy5-NHS was used. To prepare ACy7 inclusion complexes, CD derivatives (1 μmol) and ACy7 (1.2 μmol) were agitated in DDW for 24 h, followed by dialysis against DDW in a dialysis membrane (MWCO: 3.5 kDa; Cellu·Sep, Membrane Filtration Products, Inc.) for 24 h to remove excess ACy7. The dialysis product was lyophilized to obtain the CD/ACy7 powder. The absorbance of the CD/ACy7 solution was measured at 740 nm to calculate ACy7 content.

Cellular uptake in HT-29 cells

HT-29 cells (Korean Cell Line Bank, Seoul, Republic of Korea) were cultured in RPMI 1640 supplemented with 10% FBS (v/v) and 1% penicillin-streptomycin (v/v) at 37 °C in a 5% CO_2 atmosphere with a relative humidity of 95%. HT-29 cells were seeded onto four-chamber culture slides (BD Falcon, Bedford, MA, USA) at a density of 1×10^5 cells/well. After one day of incubation at 37 °C, the cells were treated with free ACy7 or PBA-(ZW)-CD/ACy7 (as ACy7, 10 μmol L^{-1}) and incubated for 2 h. To verify the PBA–sialic acid interaction, free sialic acid (500 μmol L^{-1}), a competitive inhibitor, was pre-incubated with the cells for 15 min before PBA-(ZW)-CD/ACy7 treatment. The cells were washed thrice with PBS (pH 7.4), fixed with 4% (w/v) formaldehyde solution, and treated with 4′,6-diamidino-2-phenylindole

(DAPI; H-1200, Vector laboratories, Inc., Newark, CA, USA) and Fluoroshield (ImmunoBioScience Corp., Mukilteo, WA, USA). Fluorescence images were acquired using a fluorescence microscope (THUNDER Imager Live Cell & 3D Assay, Leica Biosystems, Wetzlar, Germany). For flow cytometry analysis, HT-29 cells were seeded in 6-well plates at a density of 3×10^5 cells/well. The treatment schedule and reagent conditions were the same as those used in the fluorescence microscopy assay, except that free ACy5 and PBA-(ZW)-CD/ACy5 were used. The ACy5 fluorescence signal of HT-29 cells was measured using FACSCalibur (BD Biosciences, San Jose, CA, USA).

Animal models

Male BALB/c nude mice (5 weeks old; Nara Biotech, Seoul, Republic of Korea) were maintained in a light-controlled room at a temperature of 22 ± 2 °C and relative humidity of 55 ± 5% (Animal Center for Pharmaceutical Research, College of Pharmacy, Seoul National University, Seoul, Republic of Korea). The animal study protocol (SNU-200630-1-1) was approved by the Animal Care and Use Committee of Seoul National University. A heterotopic HT-29 tumor xenograft mouse model was established by injecting HT-29 cells (2×10^6 cells per mouse) into the right hind limb region of the mice. HT-29 cells (Korean Cell Line Bank) were cultured using the method described above. Th

e tumor volume (V, mm^3) was calculated using the following formula: V (mm^3) = 0.5 × longest diameter × (shortest diameter)^2. The orthot opic xenograft model was established according to a previously report ed method [99]. Briefly, under isoflurane anesthesia, the peritoneal cav ity of the mice was opened carefully to expose the cecum. HT-29 cel l suspension (2.0×10^6 cells, 20 μL) was inoculated into the subserosa l layer of the cecum walls. After inoculation, continuous suturing was performed to close the peritoneum and abdominal wall.

NIRF imaging studies of CD/ACy7 inclusion complexes in HT-29 tumor xenograft model

NIRF imaging was performed using a heterotopic xenograft model. After the tumor volume exceeded 200 mm^3, free ACy7 or ACy7 inclusion complexes of **CD 16**–**20** dissolved in normal saline were injected into the tail vein of mice at an ACy7 dose of 1 μmol kg^{-1}. Whole-body scanning was performed at 0.17, 0.5, 1, 2, 4, 8, and 24 h post-injection using an IVIS Spectrum In Vivo Imaging System (PerkinElmer, Waltham, MA, USA), followed by *ex vivo* imaging of the major organs and tumor tissues using the same instrument. *Ex vivo* imaging studies were performed using an orthotopic xenograft model. Four weeks after inoculation, the same dose of free ACy7 or ACy7 inclusion complexes of **CD 16**–**20** was administered intravenously. The mice were

sacrificed 24 h post-injection, from which the muscle, small intestine, colon, and cecum with tumors were dissected for *ex vivo* NIRF imaging.

Pharmacokinetic evaluation of CD/ACy7 inclusion complexes

BALB/c nude mice (5 weeks old; Nara Biotech) were intravenously injected with ACy7 or PBA-(ZW)-CD/ACy7 (as ACy7, 1 μmol kg^{-1}). Blood samples (~50 μL) were collected from the retro-orbital vein using heparinized capillary tubes (Fisher Scientific, Pittsburgh, PA, USA) at 1, 5, 15, 30, 60, 120, and 240 min post-injection under isoflurane anesthesia (staggered sampling). Blood samples were centrifuged at 16,000 × *g* for 5 min, and plasma samples (supernatant, 20 μL) were transferred to microsample tubes. The fluorescence intensities of the plasma samples were measured using an NIRF imaging system (VISQUE InVivo Smart-LF, Vieworks Co., Ltd., Anyang, Republic of Korea). The pharmacokinetic parameters of ACy7 were calculated by fitting a two-compartment model using WinNonlin software (version 5.0.1; Pharsight, CA, USA). For the evaluation of urinary excretion, ACy7 or PBA-(ZW)-CD/ACy7 was injected using the same protocol described above. Urine samples were collected and weighed at 4 and 8 h post injection, followed by centrifugation at 16,000 × *g* for 5 min. Aliquots of the supernatant (100 μL) were loaded into a 96-well plate, and ACy7 absorbance was measured at 740 nm using a UV-vis spectrophotometer (EMax Precision Microplate Reader, Molecular Devices Corp.).

2.4. Fabrication and application of CD/drug inclusion complexes

Preparation of PBA-(ZW)-CD/drug inclusion complexes

PBA-(ZW)-CD/drug inclusion complexes were fabricated using a freeze-drying method [65]. To prepare PBA-(ZW)-CD/DOX, DOX base (1.33 mg, 1.3 equiv.) and PBA-(ZW)-CD (20 mg, 1 equiv.) were dissolved in a co-solvent of DMSO and DDW (80/20, v/v; 3 mL). To prepare PBA-(ZW)-CD/UXT, UXT (2.2 mg, 2.5 equiv.) and PBA-(ZW)-CD (20 mg, 1 equiv.) were dissolved in the same solvent. Each CD/drug mixture was vortexed overnight at RT, followed by freeze-drying at −90 °C. The resulting powder was reconstituted with DDW and filtered using a syringe filter (0.45 μm pore size; Minisart RC 15, Sartorius, Göttingen, Germany) to remove precipitated (*i.e.*, unloaded) DOX base or UXT. The inclusion complex solution was lyophilized again to yield the PBA-(ZW)-CD/drug powder.

In vitro *drug release*

The drug release behavior of PBA-(ZW)-CD/DOX and PBA-(ZW)-CD/UXT was evaluated under pH conditions representing endolysosomes of cancer cells (pH 5.5) and plasma (pH 7.4). The release test was conducted under sink

conditions, wherein aliquots (200 μL) of PBA-(ZW)-CD/drug solution were transferred into dialysis tubes (Mini GeBAflex Tube; MWCO:3.5 kDa; Gene Bio-Application Ltd., Kfar Hanagide, Israel). The tubes were immersed in release media (PBS; pH 5.5, 7.4; 10 mL) and agitated at 50 rpm at 37 °C. Aliquots (200 μL) of the release medium were collected at 2, 4, 6, 8, 12, and 24 h, and the same volume of fresh medium was replenished at each time point. The amount of drug released was determined using high-performance liquid chromatography (HPLC). The amount of DOX in the sample was quantified using a Waters HPLC system (Waters Co., Milford, MA, USA) equipped with a reversed-phase C-18 column (Gemini, 250 × 4.6 mm, 3 μm; Phenomenex, Torrance, CA, USA), a separation module (Waters e2695), and a fluorescence detector (Waters 2475). The mobile phase consisted of 10 mmol L^{-1} phosphate buffer (pH 2.5, adjusted with phosphoric acid) and acetonitrile with 0.1% TEA (70:30, v/v). The excitation and emission wavelengths were 470 nm and 565 nm, respectively. The injection volume and flow rate were set at 20 μL and 0.8 mL min^{-1}, respectively. The DOX retention time was 7.3 min. The amount of UXT in the sample was determined using a Waters HPLC system (Waters Co.) equipped with a Fortis C18 column (250 × 4.6 mm, 5 μm; Fortis Technologies, Ltd., Chesire, UK), autosampler (Waters 717), binary pump (Waters 1525), and UV detector (Waters 2487). The mobile phase was composed of a phosphate buffer (pH 2.5, adjusted with phosphoric acid) and acetonitrile (60:40, v/v). The eluent was monitored at an absorption wavelength of 255 nm. The injection volume

and flow rate were 20 μL and 1 mL min^{-1}, respectively. The UXT retention time was 6.5 min.

Biodistribution studies in heterotopic HT-29 tumor xenograft mouse model

The heterotopic HT-29 xenograft mouse model was prepared as described in *2.3. Biodistribution studies of CD derivatives*. When the tumor volume reached approximately 200 mm^3, the mice were randomly divided into four groups (DOX, UXT, PBA-(ZW)-CD/DOX, and PBA-(ZW)-CD/UXT) and intravenously administered each intervention at a dose of 5 mg kg^{-1}. The mice were sacrificed at 0.5, 2, and 8 h post-injection, and tumor and normal tissues were excised and weighed, followed by tissue homogenization in 1% Triton X-100 (25%, w/v). DOX or UXT was extracted from tissue homogenate (50 μL) using acidified isopropanol (200 μL, containing 0.5 mol L^{-1} HCl) or acetonitrile (200 μL, containing 100 ng mL^{-1} carbamazepine as an internal standard), respectively. The mixture was vortexed for 15 min and centrifuged at 16,000 × *g* for 5 min at 4 °C. The amount of DOX in the tissue homogenate was quantified using the HPLC method described in *In vitro drug release*. The UXT amount was determined by using an LC-MS/MS system equipped with a reversed-phase C-18 column (Synergi™ Max-RP 80 Å, 75 × 4.6 mm, 4 μm; Phenomenex Co.), a 1260 Infinity HPLC system (Agilent Technologies), and 6430 Triple Quad LC/MS system (Agilent Technologies), and the gas temperature, gas flow rate, nebulizer pressure, and capillary

voltage were manually optimized to be 300 °C, 11 L min^{-1}, 15 psi, and 4,000 V, respectively. The mobile phase consisted of 10 mmol L^{-1} ammonium formate buffer and acetonitrile (20:80, v/v). The *m/z* values of precursor/product ions in multiple reaction monitoring mode were set at 433.1/262.1 for UXT, and 237.0/194.0 for carbamazepine. The fragmentor voltage, collision energy, and cell accelerator voltage for UXT and carbamazepine were set to 89 V/15 eV/2 V and 126 V/18 eV/2 V, respectively. The retention times of UXT and carbamazepine were 2.3 and 2.1 min, respectively.

Ex vivo *Matrix-Assisted Laser Desorption/Ionization-Mass Spectrometry Imaging (MALDI-MSI)*

Intratumoral drug distribution was assessed using *ex vivo* MALDI-MSI. When the tumor volume reached approximately 200 mm^3, DOX, UXT, PBA-(ZW)-CD/DOX, or PBA-(ZW)-CD/UXT (10 mg kg^{-1} drug) was intravenously injected into HT-29 tumor-bearing mice. Mice were sacrificed at 30 min, and the resected tumors were immediately frozen and sectioned at 10 μm thickness (CM3050S; Leica Biosystems). Tissue sections were placed onto indium tin oxide-coated glass slides and coated with 10 mg mL^{-1} DHB in a co-solvent of acetonitrile and DDW with 0.1% TFA (1:1, v/v). Mass spectrometry imaging of the tumor tissues was performed using a RapifleX MALDI Tissuetyper (Bruker Daltonics, Billerica, MA, USA).

In vitro *cytotoxicity*

HT-29 cells were cultured as described in *Cellular uptake in HT-29 cells*. HT-29 cells were seeded in a 96-well plate at a density of 5.0×10^3 cells per well and incubated for 24 h at 37 °C. The free drug or PBA-(ZW)-CD/drug inclusion complex was treated at various concentrations (0.005–5 μmol L^{-1} and 0.005–50 μmol L^{-1} for DOX and UXT, respectively), and cell viability was measured after 48 h of incubation using a colorimetric method (CellTiter 96 AQueous One Solution Cell Proliferation Assay, Promega Co., Madison, WI, USA). Similarly, the cytotoxicity of blank PBA-(ZW)-CD was evaluated in HT-29 cells at PBA-(ZW)-CD concentrations of 1–500 μg mL^{-1}. After incubation for 24, 48, and 72 h, cell viability was assessed using the method described above.

Complete blood count

Male BALB/c mice (5 weeks old; Nara Biotech) were intravenously injected with an excess amount of PBA-(ZW)-CD (270 mg kg^{-1}; > 5-fold dose) once or thrice daily. Blood samples (0.5 mL) were collected 24 h post-injection, and a complete blood count test was performed using Scil Vet abc Plus (HORIBA, Kyoto, Japan). The white blood cell count, percentage of lymphocytes, monocytes, and eosinophils, red blood cell count, hematocrit,

mean corpuscular volume, platelet count, and mean platelet volume were recorded.

Single-drug therapy in heterotopic HT-29 tumor xenograft mouse model

The antitumor efficacy of PBA-(ZW)-CD/drug inclusion complexes was evaluated in subcutaneous HT-29 tumor xenograft mice, which were prepared according to the protocol described in *2.3. Biodistribution studies of CD derivatives*. For DOX monotherapy, the mice were randomized into four groups: PBS, PBA-(ZW)-CD (blank carrier), DOX solution, and PBA-(ZW)-CD/DOX, and intravenously administered each intervention at a dose of 5 mg kg^{-1} every three days. The tumor volume and body weight were monitored every other day. The efficacy test for UXT monotherapy was performed using the same protocol, except that UXT solution and PBA-(ZW)-CD/UXT were adopted.

Combination therapy in heterotopic HT-29 tumor xenograft mouse model

Subcutaneous HT-29 tumor-bearing mice were prepared as described in *2.3. biodistribution studies of CD derivatives*. To evaluate the antitumor efficacy of the combination therapy, the mice were randomly divided into six groups: PBS, PBA-(ZW)-CD (blank carrier), DOX solution (3 mg kg^{-1}), UXT solution (3 mg kg^{-1}), DOX + UXT solutions (3 mg kg^{-1} each), PBA-(ZW)-

CD/DOX + PBA-(ZW)-CD/UXT (as a drug, 3 mg kg^{-1} each), and each intervention every three days. The tumor volume and body weight were recorded every other day. On day 14, blood samples (0.5 mL) were collected from the left ventricle and centrifuged at 16,000 × *g* for 5 min to obtain plasma samples. The levels of aspartate transaminase, alanine transaminase, alkaline phosphatase, blood urea nitrogen, and creatinine were analyzed using Fuji Dri-Chem 3500s (Fujifilm Holdings Corp., Tokyo, Japan).

Evaluation of therapeutic efficacy in orthotopic colorectal tumor xenograft mouse model

To establish an orthotopic colorectal tumor xenograft mouse model, luciferase-expressing HT-29 (HT-29/Luc) (2.0×10^6 cells, 20 μL) were inoculated into the cecum of male BALB/c nude mice (5 weeks old; Nara Biotech) under isoflurane anesthesia. Seven days after HT-29/Luc inoculation, d-luciferin (150 mg kg^{-1}) was injected intraperitoneally, and bioluminescence was measured with the IVIS Spectrum In Vivo Imaging System (PerkinElmer) to confirm tumor formation in the cecum region. The mice were randomly divided into three groups and intravenously administered PBS, DOX + UXT solutions (3 mg kg^{-1} for each), or PBA-(ZW)-CD/DOX + PBA-(ZW)-CD/UXT (as a drug, 3 mg kg^{-1} for each). Tumor growth (*via* bioluminescence) and body weight were measured on days 0, 4, 8, 11, and 14. On day 14, the

organs and tissues of interest, including the tumor, heart, lungs, liver, kidneys, and spleen, were dissected and stained with hematoxylin and eosin. Tumor tissues were subjected to terminal deoxynucleotidyl transferase dUTP nick-end labeling staining.

2.5. Statistical analysis

All experiments in this study were performed at least three times, and the data are presented as the mean ± standard deviation. Statistical analyses were conducted using the two-tailed *t*-test or one-way analysis of variance with Tukey's multiple comparison test or Fisher's test. for *post-hoc* analysis. *p*-value < 0.05 was considered to be statistically significant.

3. Results and Discussion

3.1. Design, synthesis, and optimization of CD derivatives

β-CD was selected as the core material to build organic renal-clearable NCs because of its several advantages, including biocompatibility and biodegradability, lack of pharmacological activity and immunogenicity, and a polyfunctional structure exhibiting hydrophobic cavity for host–guest interactions with various compounds, such as drugs and imaging probes [100]. Various charged moieties were introduced to the side chains of β-CD to reduce off-target accumulation, as the surface charge has a significant impact on the *in vivo* fate of NCs, especially those of ultrasmall sizes [51-53, 82, 83]. Sulfobetaine was adopted as a zwitterionic moiety because it can resist non-specific protein adsorption more efficiently than other amino acids [101]. Based on the general understanding of the structure–antifouling efficiency relationship of zwitterionic molecules [102], two types of sulfobetaine derivatives (compounds 2 and 4) were prepared with different numbers of methylene groups between quaternary ammonium and carboxylic acid (Figure 1). Succinic anhydride, betaine hydrochloride, and glycolic acid were used for the preparation of the negative, positive, and uncharged CD derivatives, respectively. Phenylboronic acid (PBA) was chosen as a tumor-targeting probe because it can recognize sialyl epitopes that are overexpressed

in CRC cells [103]. The neutral charge of PBA at physiological pH was also suitable for minimizing the unintended charge effects by targeting ligands on the entire NC structure [104, 105]. Glutamic acid was used as a tri-arm linker to tether both the charged moiety and the targeting ligand to the CD core.

Twenty CD derivatives (CD 1–20) were designed by modifying the charged moiety linked to the amine group of the glutamic acid linker (P1) and spacers between cyclodextrin and glutamic acid (P2), and glutamic acid and PBA (P3) (Figure 2 and 3). Synthesis was performed through the following three main steps: (1) synthesis of PBA–P3 (zero-length or PEG_4)–glutamic acid (compounds **6** and **10**), (2) conjugation of (1) and CD–P2 (zero-length or spacers) (compounds **12**, **19**, **20**, **28**, and **30**), and (3) conjugation of (2) and P1 (charged moieties). Each module (A–F) was conjugated *via* amide coupling, and the detailed synthetic schemes are summarized in Figure 4. Successful syntheses of the intermediates were confirmed using proton nuclear magnetic resonance (^{1}H-NMR) spectroscopy and mass spectrometry (Figures 5–9). The degrees of conjugation of PBA or spacers (PEG_n and caproic acid) to CD intermediates were calculated by comparing integration values of anomeric protons of CD (~4.8 ppm) and distinct signals of the conjugated compounds (8.0 and 1.3 ppm for PEG_n; 1.2–1.5 ppm for caproic acid; and 9.8, 6.8, and 1.3 ppm for PBA). The introduction of PBA was further confirmed *via* the alizarin red S test, wherein the CD intermediates (compounds **11**, **17**, **18**, **27**, and **29**) were nearly heptaconjugated (Figure 10). In synthesis step (3), excess charged moieties were used to convert all the

primary amines on the glutamic acid linker. The fluorescamine assay revealed that more than 98.8% of the primary amines were consumed within 48 h, indicating the complete conjugation of the charged moieties (Figure 11). This result was further supported by the ^{1}H-NMR spectra of the final products, **CD 16–20** (Figure 12).

The foremost requirement for intravenous injections is colloidal stability in the bloodstream. It should be noted that CD derivatives may become more vulnerable to aggregation upon the formation of inclusion complexes with hydrophobic guest molecules. Thus, CD derivatives with poor colloidal stability in phosphate-buffered saline (PBS; high ionic strength condition) or fetal bovine serum (FBS; bloodstream condition) were screened out based on turbidimetric analysis by measuring absorbance at 600 nm (Figure 13, summarized in Figure 14). CD derivatives with no spacers (*i.e.*, zero length) at P2 and P3 (**CD 1**, **2**, **4**, and **5**) exhibited precipitation when dispersed in PBS and FBS. The introduction of a short PEG_4 spacer at P2 was insufficient to secure colloidal stability in PBS (**CD 6**, **7**, **9**, and **10**); **CD 8**, **9**, and **10** were readily dissolved in FBS, while **CD 6** and **7** showed severe aggregation. These results can be attributed to the strong inter- and intramolecular interactions of the zwitterionic moieties rather than the inherent hydrophobicity of the CD molecules [106]. Accordingly, CD derivatives with longer spacers (PEG_8) at P2 (**CD 11**, **13**, **14**, and **15**) were dissolved in PBS and FBS. Interestingly, however, the A_2 module (compound **4**)-conjugated CD derivative (**CD 12**) precipitated in both media, even with

the PEG_8 spacer. Thus, the A_1 module (compound **2**) was selected as the zwitterionic functional group for further study. Next, the length of the PEG spacer was extended to further improve the colloidal stability. For **CD 16**, PBA and A_1 were directly conjugated to glutamic acid and a long PEG_{12}-caproic acid spacer was inserted at P2. In contrast, **CD 17–20** were prepared by inserting a PEG_8-caproic acid spacer at P2 and the PEG_4 spacer at P3, hypothesizing that nearby sulfobetaine could hinder the sialic acid-targeting ability of PBA. As expected, **CD 16–20** were dissolved clearly in both media and exhibited no significant turbidity changes for 48 h, suggesting high colloidal stability after intravenous administration (Figure 13B). Moreover, dynamic light scattering (DLS) analysis revealed that the hydrodynamic diameters (HDs) of **CD 16–20** were of renal-clearable size (5–6.6 nm), and the zeta potential of each CD derivative corresponded to the decorated charged moieties, supporting the successful synthesis of CD derivatives (Table 1).

3.2. Biodistribution of CD derivatives

Adamantyl sulfocyanine 7 (ACy7) was synthesized as a fluorescence probe for the near-infrared fluorescence (NIRF) imaging-assisted biodistribution study of CD derivatives (Figure 15A). Given its high affinity to the hydrophobic cavity of CD, ACy7 was successfully loaded onto **CD 16–20** by

inducing host-guest interactions under aqueous conditions [107, 108], resulting in stable CD/ACy7 inclusion complexes. Although **CD 11** and **14** had decent colloidal stability (Figure 14), gradual precipitation was observed in the presence of ACy7 (Figure 15B), discouraging further evaluation of these two compounds.

Next, free ACy7 and **CD 16–20**/ACy7 inclusion complexes were intravenously administered to a CRC mouse model, and *ex vivo* imaging was performed 24 h post-injection (Figure 16). In this study, HT-29 (human colorectal adenocarcinoma) was utilized because this cell line represents the traits of human CRC, including the high expression of sialyl Lewis A, a well-known target of PBA [109]. Compared to free Acy7, which showed non-selective organ distribution, **CD 16**/ACy7 (zwitterionic) exhibited significantly reduced lung and liver accumulation with increased kidney selectivity. These results imply that zwitterionic CD derivatives may reduce the off-target distribution or retention of cargo molecules and facilitate renal excretion. A similar phenomenon was observed in the case of **CD 17**/ACy7, another zwitterionic inclusion complex, wherein the average fluorescence intensity values of ACy7 in normal tissues were almost at the same levels as those of **CD 16**/ACy7. However, the tumor distribution efficiency of **CD 17**/ACy7 was 2.02-fold higher than that of **CD 16**/ACy7 ($p < 0.001$) (Figure 17**)**, even with similar physicochemical properties (Table 1). This result could be attributed to the insertion of the PEG_4 spacer between the PBA moiety and glutamic acid linker, reducing the possible interference of sulfobetaine in the

PBA–sialic acid interaction (Figure 18A). Although **CD 18**/ACy7, a negatively charged inclusion complex, displayed an overall high tumor-to-background ratio (TBR) comparable to that of **CD 17**/ACy7, the tumor distribution efficiency was 1.46-fold lower ($p < 0.01$) (Figure 17). Conversely, **CD 19**/ACy7 (positively charged) and **CD 20**/ACy7 (neutral) showed comparable tumor distribution efficiencies to **CD 17**/ACy7, but their TBR values were approximately 2-fold lower in all organs (Figure 17 and 18B). Based on high TBR and tumor distribution efficiency, **CD 17**, hepatkis-(6-deoxy-6-((phenylboronic acid-tetraethyleneglycol-L-glutamic acid N^{α}-sulfobetaine)-octaethyleneglycol-caproamide))-β-cyclodextrin (PBA-(ZW)-CD), was selected as an optimized renal clearable CD derivative for further investigations.

3.3. Tumor targetability, pharmacokinetics, and urinary excretion of PBA-(ZW)-CD/ACy7

The structural components of PBA–(ZW)–CD are shown in Figure 19A. The caproic acid linker enhanced hydrophobic interactions with guest molecules [64, 110], and the PEG_8 spacer improved colloidal stability. Sulfobetaine, a zwitterionic functional group, reduces non-specific tissue binding [111, 112]. The PEG_4 spacer between glutamic acid and PBA helped preserve the targeting ability of PBA. These features may translate into improved *in vivo*

distribution profiles (Figure 19B). Thus, we hypothesized that PBA-(ZW)-CD/ACy7 could be rapidly distributed throughout the body and selectively retained in tumor tissues *via* PBA–sialic acid interactions. In addition, the zwitterionic sulfobetaine moiety could reduce non-specific interactions between PBA-(ZW)-CD and normal tissues; thus, the clearance of ACy7 may be accelerated *via* the renal route, further enhancing tumor selectivity.

Prior to verifying the targetability of PBA-(ZW)-CD *in vivo*, enhancement in the cellular uptake of PBA-(ZW)-CD/ACy7 *via* PBA–sialic acid interaction was confirmed in HT-29 cells by fluorescence microscopy (Figure 20A). Notably, the cellular uptake efficiency of PBA-(ZW)-CD/ACy7 was compromised in the presence of free sialic acid, a competitive inhibitor, suggesting the involvement of PBA–sialic acid interactions in the cellular uptake of PBA-(ZW)-CD. Similarly, flow cytometry analyses were performed on HT-29 cells treated with the inclusion complex of adamantyl sulfocyanine 5 (Figure 15A; Figure 20B), and the results corresponded well with the fluorescence microscopy data, supporting the use of PBA as an HT-29 targeting moiety.

The tumor targeting ability of PBA-(ZW)-CD/ACy7 was investigated in HT-29 tumor-xenograft mice using real-time NIRF imaging (Figure 21A). In the early phase (~2 h), intravenously administered ACy7 and PBA-(ZW)-CD/ACy7 were both distributed throughout the body with no tumor selectivity. However, after rapid renal excretion of PBA-(ZW)-CD, which was verified in a preliminary study with sulfocyanine 7-conjugated

PBA-(ZW)-CD (*i.e.*, *via* covalent bond) (Figure 22A), the PBA-(ZW)-CD/ACy7 inclusion complex-treated mice exhibited distinct fluorescence signals in the tumor and kidney regions in whole-body imaging (Figure 21A). Furthermore, the TBR of PBA-(ZW)-CD/ACy7 exceeded 2, the standard cut-off value for tumor detection [113], at 8 h post-injection and continuously increased for the next 16 h, whereas free ACy7 showed TBR values less than 2 throughout the experimental period (Figure 21B). The high TBR of PBA-(ZW)-CD/ACy7 can be attributed to prolonged tumor retention and accelerated elimination from normal tissues. From a clinical perspective, determining the tumor margin is of paramount importance for the accurate surgical resection of CRC, especially in laparoscopic or robot-assisted operations [113-115]. To evaluate the applicability of PBA-(ZW)-CD/ACy7 in image-guided surgery, PBA-(ZW)-CD/ACy7 was injected into the tail vein of an orthotopic CRC model, which was prepared by subserosal inoculation of HT-29 cells in the cecum after laparotomy. At 24 h post-injection, PBA-(ZW)-CD/ACy7 showed high TBR values of approximately 4 against adjacent normal tissues, including the small intestine, colon, and muscle, providing accurate tumor margins for resection (Figure 21C and 21D).

The pharmacokinetic properties of PBA-(ZW)-CD/ACy7 were investigated *via* time-course blood sampling and ACy7 quantification (Table 2 and Figure 23). Exhibiting biphasic decay, free ACy7 and PBA-(ZW)-CD/ACy7 showed similar distribution half-lives ($t_{1/2\alpha}$; 4.2 and 3.0 min, respectively). This result suggests that PBA-(ZW)-CD/ACy7 can be

distributed to the whole body as quickly as free ACy7, as observed in the *in vivo* imaging study (Figure 21A). However, in the elimination phase, PBA-(ZW)-CD/ACy7 had a significantly shorter elimination half-life ($t_{1/2\beta}$; 52.5 min) than free ACy7 (92.5 min). Considering comparable exposure, the reduced $t_{1/2\beta}$ value could result from the lower volume of distribution (V_d) of the inclusion complex (5.6 mL) compared to that of the free dye (7.9 mL), which also implies reduced non-specific binding of ACy7 in normal tissues. Although the total body clearance values of free dye (0.08 mL min^{-1}) and inclusion complex (0.10 mL min^{-1}) were almost the same, the cumulative urinary excretion of PBA-(ZW)-CD/ACy7 was 2.3-fold higher than that of free ACy7, which suggests that PBA-(ZW)-CD may facilitate the renal excretion of cargo molecules (Figure 21E).

3.4. Preparation and characterization of PBA-(ZW)-CD/drug inclusion complexes

PBA-(ZW)-CD/drug inclusion complexes were prepared with two chemotherapeutic agents, doxorubicin (DOX) and ulixertinib (UXT) to assess the potential of CRC-targeted combination therapy. Generally, the use of DOX is discouraged in CRC treatment, as DOX activates the extracellular signal-regulated kinase (ERK)-1/2 signaling pathway and induces drug resistance. However, combination therapy with UXT, a potent first-in-class

ERK1/2 inhibitor, may help overcome DOX resistance and further enhance therapeutic efficacy (Figure 24) [116-120]. As both drugs were poorly soluble in aqueous media, a co-solvent of dimethyl sulfoxide and water was used to solubilize the drugs with PBA-(ZW)-CD to induce host–guest interactions. After lyophilization, water-soluble PBA-(ZW)-CD/drug inclusion complexes were obtained at molar ratios of drug to PBA-(ZW)-CD of approximately 1 and 2 for DOX and UXT, respectively (Figure 25). The drug contents of PBA-(ZW)-CD/DOX and PBA-(ZW)-CD/DOX were 5.10 ± 0.13% and 7.91 ± 0.14%, which were close to the theoretical values of 5.26% and 8.13%, respectively.

The formation of PBA-(ZW)-CD/drug inclusion complexes was investigated using 1H-NMR (Figure 26A). Although the peaks of CD protons engaging in the host–guest interaction (i.e., protons in the CD cavity) overlapped with strong PEG signals at 3.5–3.9 ppm, we could observe slight changes in the chemical shifts of DOX (red arrows) and UXT (blue arrows) after complexation [66, 121]. These intermolecular correlations were further confirmed by rotating frame Overhauser enhancement spectroscopy (ROESY) (Figure 26B). The ROESY spectrum of PBA-(ZW)-CD/DOX revealed dipolar couplings between the aromatic proton Ha of DOX and H1 protons of PBA-(ZW)-CD, indicating that the anthraquinone rings of DOX were internalized in the cyclodextrin cavity. The PBA-(ZW)-CD/UXT spectrum also displayed interactions between the protons Hb, Hc, and Hd of UXT and

the inner cavity protons H2 and H3 of PBA-(ZW)-CD, supporting inclusion complex formation.

The HDs of the inclusion complexes were measured using DLS to confirm whether PBA-(ZW)-CD maintained its renal-clearable size after drug loading (Table 3 and Figure 27A). As shown in the number-weighted HD distribution, PBA-(ZW)-CD/DOX had a mean HD of 13.04 ± 3.85 nm at pH 7.4. The slight increase in HD compared to that of the blank PBA-(ZW)-CD could be attributed to concentration-dependent (*i.e.*, reversible) coordination between the primary amine of DOX and boronic acid of PBA-(ZW)-CD [122]. Since the coordination weakens at acidic pH, the mean HD of PBA-(ZW)-CD/DOX decreased to 7.09 ± 0.26 nm at pH 5.5, which is almost the same value of blank PBA-(ZW)-CD HD (6.58 ± 0.27 nm; Table 1). However, PBA-(ZW)-CD/UXT showed comparable HD distributions at pH 5.5 and 7.4, displaying mean HDs of 6.30 ± 0.11 nm and 6.30 ± 0.09 nm, respectively, which implies the lesser influence of acidity. A similar phenomenon was observed in drug release tests performed at pH 5.5 and 7.4 (Figure 27B). Due to the DOX–boronic acid coordination, the cumulative DOX release from the inclusion complex reached only 4.9 ± 0.9% even after 24 h incubation at pH 7.4. However, at pH 5.5, the cumulative DOX release significantly increased to 21.3 ± 0.1% ($p < 0.005$), which could translate into selective drug exposure to tumor tissues, considering the acidic tumor microenvironment (TME). PBA-(ZW)-CD/UXT also showed statistically significant pH-dependency in its release profile, but the cumulative drug release under each condition

showed only a 10% difference, displaying 38.9 ± 2.8% and 27.9 ± 1.6% at pH 5.5 and 7.4, respectively. The zeta potential of both inclusion complexes increased at acidic pH due to the ionization of the guest drug while maintaining zwitterionic properties at pH 7.4 (Table 3), which also explains the enhanced drug release of both inclusion complexes at pH 5.5.

3.5. Biodistribution of PBA-(ZW)-CD/drug inclusion complexes

The biodistribution of PBA-(ZW)-CD/drug inclusion complexes was assessed in subcutaneous HT-29 tumor xenograft mice in comparison with that of free drugs, wherein the drug amounts deposited in major organs, muscles, and tumors were determined after intravenous administration of the drug solution or inclusion complex at a dose of 5 mg kg^{-1}. As expected from the biodistribution profiles of PBA-(ZW)-CD/ACy7 (Figure 16), DOX exposure to normal tissues (*i.e.*, off-target) in the distribution phase was drastically decreased when treated with PBA-(ZW)-CD/DOX (Figure 28A). Notably, the DOX amount in the heart at 2 h in the inclusion complex group was 6.5-fold lower than that in the free drug group ($p < 0.001$). Moreover, in the muscle tissue, the DOX level of the inclusion complex group was below the detection limit (<200 ng g^{-1} tissue) even at 0.5 h post injection, while the free DOX group exhibited 2.73 ± 0.30 μg g^{-1} tissue. Considering that cardiotoxicity and skeletal muscle atrophy are the major side effects of DOX

that limit its application to CRC [123-126], the improved biodistribution profile *via* PBA-(ZW)-CD complexation could enhance the chances of future clinical translation. In the tumor tissue, although both free DOX and PBA-(ZW)-CD/DOX exhibited similar exposure at 0.5 h, PBA-(ZW)-CD/DOX had prolonged tumor retention compared to free DOX, resulting in 2.0-fold higher DOX accumulation at 8 h ($p < 0.005$).

Unlike DOX, which non-specifically binds to various biomacromolecules, UXT exhibited the expected biodistribution profile when formulated as PBA-(ZW)-CD/UXT (Figure 28B). PBA-(ZW)-CD/UXT showed rapid clearance in the normal tissues, with UXT amounts remaining in the heart, lungs, kidneys, and liver less than 0.65 μg g^{-1} tissue within 2 h, which were 8.0-, 17.0-, 5.6-, and 13.6-fold lower values than those of free UXT solution, respectively. In the tumor tissues, however, PBA-(ZW)-CD/UXT displayed a 2.1-fold higher accumulation of UXT than free UXT at 8 h post-injection ($p < 0.05$). These findings clearly indicate that PBA-(ZW)-CD can enhance the tumor retention of guest drugs and reduce their off-target accumulation in normal tissues, as in the case of PBA-(ZW)-CD/ACy7.

Enhancement of the average drug concentration in tumor tissues could be one of the critical elements for successful tumor-targeted drug delivery. However, one cannot underestimate the importance of homogenous drug distribution throughout the tumor mass, as the presence of cancer cells that are poorly exposed to anticancer agents can result in tumor relapse [127-129]. Conventional NCs utilizing the EPR effect suffer from the issue of

reduced convection in the TME owing to their large particle size [27, 130-132]. PBA-(ZW)-CD/drug inclusion complexes could evade this issue given their ultrasmall size and zwitterionic surface charge. As observed in the *ex vivo* matrix-assisted laser desorption ionization-mass spectrometry imaging (MALDI-MSI) (Figure 29A), the intratumoral DOX (*m/z* 544.6) and UXT (*m/z* 434.7) signals in the inclusion complex-treated group exhibited a comparable spatial intensity distribution (as the coefficient of variation) to those of the solution-treated group, suggesting that PBA-(ZW)-CD/drug was as highly tumor-penetrable as a free drug solution (Figure 29B). In addition, the average intensity values of both drugs were significantly higher in the PBA-(ZW)-CD/drug groups than in the corresponding solution groups (Figure 29C), which correlates well with the biodistribution study performed with tissue homogenates (Figure 28A and 28B).

The unique pharmacokinetic properties of PBA-(ZW)-CD, which are rarely observed in other clinical reports [17], are summarized as follows: (1) PBA-(ZW)-CD may control the biodistribution of cargo molecules in an opposite manner depending on the deposition site, showing decreased and increased clearance in tumor and normal tissues, respectively, and (2) PBA-(ZW)-CD/drug inclusion complexes may penetrate the TME as readily as free drug solutions, promoting homogeneous drug delivery throughout the tumor mass. Based on these findings, we hypothesized that PBA-(ZW)-CD/drug inclusion complexes could simultaneously improve the apparent potency and

reduce the potential toxicity of anticancer agents, enabling high-dose administration and subsequent enhancement of therapeutic efficacy.

3.6. PBA-(ZW)-CD/drug-assisted single-drug and combination therapies in HT-29 tumor xenograft mouse model

Encouraged by the remarkable biodistribution profiles of PBA-(ZW)-CD, the *in vivo* antitumor efficacy of each PBA-(ZW)-CD/drug inclusion complex was evaluated in the heterotopic HT-29 xenograft mouse model. As a preliminary study, the *in vitro* and *in vivo* toxicity of blank PBA-(ZW)-CD was evaluated. In HT-29 cells, PBA-(ZW)-CD showed negligible cytotoxicity at physiologically-relevant concentrations (~500 μg mL^{-1}) (Figure 30). Moreover, single and repeated (three times) intravenous administration of an excess amount of PBA-(ZW)-CD (270 mg kg^{-1} per administration) induced no significant deviation in the complete blood counts of mice without observable changes in vital signs or behavioral expressions of pain (Table 4).

To evaluate the tumor-suppressive efficiency of PBA-(ZW)-CD/DOX and its potential to reduce the adverse effects of DOX, the dose was set at 5 mg kg^{-1}, wherein significant systemic toxicity and cardiotoxicity of DOX have been reported [133, 134]. As shown in Figure 31, the tumor volume of the PBA-(ZW)-CD/DOX group was significantly smaller than that

of the other groups ($p < 0.001$). The body weight of the DOX solution group was significantly lower than that of the other groups, indicating that a high dose of free DOX caused severe systemic toxicity ($p < 0.0001$). However, there was no noticeable change in body weight of the PBA-(ZW)-CD/DOX group during treatment. Similarly, PBA-(ZW)-CD/UXT also showed a significant improvement in tumor growth inhibition at the therapeutic dose (5 mg kg^{-1}) ($p < 0.005$), but systemic toxicity in terms of body weight change was not observed in any group (Figure 32). Since the inclusion complex had a marginally higher cytotoxicity than the corresponding free drug (Table 5 and Figure 33), its highly enhanced antitumor efficacy *in vivo* could mainly result from improved biodistribution.

Next, a combination therapy with PBA-(ZW)-CD/DOX and PBA-(ZW)-CD/UXT was performed in the same mouse model. The mice were divided into six groups, including PBS, blank PBA-(ZW)-CD, DOX or UXT monotherapy (solution), and DOX + UXT combination therapy (solution or inclusion complex), and intravenously injected with each intervention every three days five times, and the doses of DOX and UXT were reduced to 3 mg kg^{-1}, expecting the synergistic effect of DOX and UXT combination. As observed in the tumor growth profile (Figure 34A), the combination of DOX and UXT solutions exhibited enhanced antitumor efficacy on average when compared to monotherapy with each drug, but no statistically significant difference was found between the DOX + UXT solution and DOX solution groups ($p > 0.05$). However, the combination of inclusion complexes showed

dramatically improved tumor growth inhibition compared to the other groups, of which the average tumor volume on day 14 was 2.1-fold smaller than that in the DOX + UXT solution group ($p < 0.05$). A similar tendency was observed in the dissected tumor weight data (Figure 34B), where the PBA-(ZW)-CD/DOX + PBA-(ZW)-CD/UXT group displayed the lowest tumor weight compared to the other groups, showing a 2.9-fold lower average tumor weight on day 14 compared to that of the DOX + UXT solution group ($p < 0.05$). The superior antitumor efficacy of the PBA-(ZW)-CD/drug combination could be explained by the improved drug distribution to the tumor tissue spatially and temporally enough to induce synergistic effects between DOX and UXT. Meanwhile, the mice in all groups did not lose body weight significantly during the treatment (Figure 35) and showed no abnormal changes in blood biochemistry (Table 6), indicating negligible systemic toxicity.

3.7. PBA-(ZW)-CD/drug combination therapy in orthotopic CRC mouse model

Antitumor efficacy of the PBA-(ZW)-CD/drug-assisted combination therapy was evaluated in an orthotopic CRC model. One week after the inoculation of luciferase-expressing HT-29 (HT-29/Luc) cells into the cecum, the mice

were intravenously administered PBS (no intervention), DOX + UXT (solution), or PBA-(ZW)-CD/DOX + PBA-(ZW)-CD/UXT every three days for five times at a dose of 3 mg kg^{-1} for each drug. Bioluminescence imaging revealed that both solution- and inclusion complex-based combination therapies significantly reduced tumor growth compared to no intervention (Figure 36A). Notably, PBA-(ZW)-CD/drug combination therapy had a much higher tumor inhibitory efficacy than solution therapy, displaying a 4.2-fold lower bioluminescence intensity on day 14 ($p < 0.005$) (Figure 36B).

Unlike the heterotopic model prepared by the subcutaneous injection of HT-29 cell suspension, the orthotopic CRC model prepared *via* laparotomy exhibited lower tolerability to solution-based combination therapy, with the average body weight reduced to 88.9% of the non-intervention (PBS) group ($p < 0.01$) (Figure 36C). However, no weight loss was observed in the PBA-(ZW)-CD/drug combination group, implying that PBA-(ZW)-CD reduced the systemic toxicity of ACT after surgical resection. At the end of the efficacy test, tumor tissues and major organs, including the heart, kidneys, liver, lungs, and spleen, were dissected and subjected to hematoxylin and eosin staining. As shown in Figure 37, no detrimental changes were observed in normal tissues, indicating that PBA-(ZW)-CD can minimize the dose-limiting toxicity of anticancer agents. Terminal deoxynucleotidyl transferase dUTP nick-end labeling staining was also performed on the tumor tissues (Figure 37), which revealed that PBA-(ZW)-CD/drug combination therapy induced a

higher degree of apoptosis than solution-based combination therapy. This result correlated well with the antitumor efficacy data (Figure 34A and 36B).

4. Conclusions

In this study, renal-clearable zwitterionic CD nanocarriers, namely PBA-(ZW)-CD, were delicately tailored for CRC-selective imaging and drug delivery. Twenty CD derivatives were prepared by modifying the charged moieties and spacers to improve their colloidal stability and *in vivo* pharmacokinetic behavior. CRC targetability, organ distribution, and renal clearance of CD derivatives were screened in the form of ACy7 inclusion complexes, from which PBA-(ZW)-CD was selected as the optimized structure with enhanced tumor selectivity and reduced off-target accumulation. Given its high biocompatibility, PBA-(ZW)-CD/drug inclusion complexes of DOX and UXT were fabricated and applied in combination therapy for CRC. Notably, PBA-(ZW)-CD enhanced the tumor retention of drugs, while facilitating their elimination in normal tissues. Additionally, the improved antitumor efficacies of PBA-(ZW)-CD/drug-assisted single-drug and combination therapies were demonstrated in various CRC models. Therefore, PBA-(ZW)-CD may be used as a promising CRC-targeting nanoplatform with high potential for clinical translation.

5. References

[1] V. Schirrmacher, From chemotherapy to biological therapy: A review of novel concepts to reduce the side effects of systemic cancer treatment (Review), Int. J. Oncol., 54 (2019) 407-419.

[2] W.T. Iams, J. Porter, L. Horn, Immunotherapeutic approaches for small-cell lung cancer, Nat. Rev. Clin. Oncol., 17 (2020) 300-312.

[3] P. Jaaks, E.A. Coker, D.J. Vis, O. Edwards, E.F. Carpenter, S.M. Leto, L. Dwane, F. Sassi, H. Lightfoot, S. Barthorpe, D. van der Meer, W.N. Yang, A. Beck, T. Mironenko, C. Hall, J. Hall, I. Mali, L. Richardson, C. Tolley, J. Morris, F. Thomas, E. Lleshi, N. Aben, C.H. Benes, A. Bertotti, L. Trusolino, L. Wessels, M.J. Garnett, Effective drug combinations in breast, colon and pancreatic cancer cells, Nature, 603 (2022) 166-173.

[4] M.J. Grant, R.S. Herbst, S.B. Goldberg, Selecting the optimal immunotherapy regimen in driver-negative metastatic NSCLC, Nat. Rev. Clin. Oncol., 18 (2021) 625-644.

[5] A.D. Wagner, W. Grothe, J. Haerting, G. Kleber, A. Grothey, W.E. Fleig, Chemotherapy in advanced gastric cancer: A systematic review and meta-analysis based on aggregate data, J. Clin. Oncol., 24 (2006) 2903-2909.

[6] T. Morrow, M. Siegel, S. Boone, G. Lawless, W. Carter, Chemotherapy dose intensity determination as a quality of care measure for managed care organizations in the treatment of early-stage breast cancer, Am. J. Med. Qual., 17 (2002) 218-224.

[7] J.P. Guastalla, 3rd, V. Dieras, The taxanes: toxicity and quality of life considerations in advanced ovarian cancer, Br. J. Cancer, 89 (2003) S16-22.

[8] F.M. de Man, A.K.L. Goey, R.H.N. van Schaik, R.H.J. Mathijssen, S. Bins, Individualization of irinotecan treatment: a review of pharmacokinetics, pharmacodynamics, and pharmacogenetics, Clin. pharmacokinet., 57 (2018) 1229-1254.

[9] R. Sun, J. Xiang, Q. Zhou, Y. Piao, J. Tang, S. Shao, Z. Zhou, Y.H. Bae, Y. Shen, The tumor EPR effect for cancer drug delivery: Current status, limitations, and alternatives, Adv. Drug Deliv. Rev, 191 (2022) 114614.

[10] Y. Shi, R. van der Meel, X. Chen, T. Lammers, The EPR effect and beyond: Strategies to improve tumor targeting and cancer nanomedicine treatment efficacy, Theranostics, 10 (2020) 7921-7924.

[11] T.M. Allen, P.R. Cullis, Liposomal drug delivery systems: from concept to clinical applications, Adv. Drug Deliv. Rev, 65 (2013) 36-48.

[12] Y. Gao, D.R. Gao, J. Shen, Q.W. Wang, A review of mesoporous silica nanoparticle delivery systems in chemo-based combination cancer therapies, Front. Chem., 8 (2020) 598722.

[13] T. Vangijzegem, D. Stanicki, S. Laurent, Magnetic iron oxide nanoparticles for drug delivery: applications and characteristics, Expert Opin Drug Deliv, 16 (2019) 69-78.

[14] C.K. Kim, P. Ghosh, V.M. Rotello, Multimodal drug delivery using gold nanoparticles, Nanoscale, 1 (2009) 61-67.

[15] A. Gagliardi, E. Giuliano, E. Venkateswararao, M. Fresta, S. Bulotta, V. Awasthi, D. Cosco, Biodegradable polymeric nanoparticles for drug delivery to solid tumors, Front. pharmacol., 12 (2021) 601626.

[16] S.M. Rafiyath, M. Rasul, B. Lee, G. Wei, G. Lamba, D. Liu, Comparison of safety and toxicity of liposomal doxorubicin vs. conventional anthracyclines: a meta-analysis, Exp. Hematol. Oncol, 1 (2012) 10.

[17] D.X. Sun, S. Zhou, W. Gao, What went wrong with anticancer nanomedicine design and how to make it right, ACS Nano, 14 (2020) 12281-12290.

[18] K. Park, The beginning of the end of the nanomedicine hype, J. Control. Release, 305 (2019) 221-222.

[19] S. Wilhelm, A.J. Tavares, Q. Dai, S. Ohta, J. Audet, H.F. Dvorak, W.C.W. Chan, Analysis of nanoparticle delivery to tumours, Nat. Rev. Mater., 1 (2016) 16014.

[20] T. Lammers, Macro-nanomedicine: Targeting the big picture, J. Control. Release, 294 (2019) 372-375.

[21] S. Sindhwani, A.M. Syed, J. Ngai, B.R. Kingston, L. Maiorino, J. Rothschild, P. MacMillan, Y.W. Zhang, N.U. Rajesh, T. Hoang, J.L.Y. Wu, S. Wilhelm, A. Zilman, S. Gadde, A. Sulaiman, B. Ouyang, Z. Lin, L.S. Wang, M. Egeblad, W.C.W. Chan, The entry of nanoparticles into solid tumours, Nat. Mater., 19 (2020) 566-575.

[22] D. Rosenblum, N. Joshi, W. Tao, J.M. Karp, D. Peer, Progress and challenges towards targeted delivery of cancer therapeutics, Nat.

Commun., 9 (2018) 1410.

[23] J. Park, Y. Choi, H. Chang, W. Um, J.H. Ryu, I.C. Kwon, Alliance with EPR Effect: Combined strategies to improve the EPR effect in the tumor microenvironment, Theranostics, 9 (2019) 8073-8090.

[24] J.A. Nagy, S.H. Chang, S.C. Shih, A.M. Dvorak, H.F. Dvorak, Heterogeneity of the tumor vasculature, Semin Thromb Hemost, 36 (2010) 321-331.

[25] T. Ojha, V. Pathak, Y. Shi, W.E. Hennink, C.T.W. Moonen, G. Storm, F. Kiessling, T. Lammers, Pharmacological and physical vessel modulation strategies to improve EPR-mediated drug targeting to tumors, Adv. Drug Deliv. Rev, 119 (2017) 44-60.

[26] S.H. Lee, O.K. Park, J. Kim, K. Shin, C.G. Pack, K. Kim, G. Ko, N. Lee, S.H. Kwon, T. Hyeon, Deep tumor penetration of drug-loaded nanoparticles by click reaction-assisted immune cell targeting strategy, J. Am. Chem. Soc., 141 (2019) 13829-13840.

[27] C.L. Waite, C.M. Roth, Nanoscale drug delivery systems for enhanced drug penetration into solid tumors: current progress and opportunities, Crit. Rev. Biomed. Eng., 40 (2012) 21-41.

[28] C.Q. Peng, M.X. Yu, J.T. Hsieh, P. Kapur, J. Zheng, Correlating anticancer drug delivery efficiency with vascular permeability of renal clearable versus non-renal clearable nanocarriers, Angew. Chem., Int. Ed., 58 (2019) 12076-12080.

[29] R.H. Grantab, I.F. Tannock, Penetration of anticancer drugs through

tumour tissue as a function of cellular packing density and interstitial fluid pressure and its modification by bortezomib, BMC Cancer, 12 (2012) 214.

[30] M. Yu, J. Zheng, Clearance pathways and tumor targeting of imaging nanoparticles, ACS Nano, 9 (2015) 6655-6674.

[31] H.S. Choi, W. Liu, P. Misra, E. Tanaka, J.P. Zimmer, B.I. Ipe, M.G. Bawendi, J.V. Frangioni, Renal clearance of quantum dots, Nat. Biotechnol., 25 (2007) 1165-1170.

[32] S.D. Li, L. Huang, Stealth nanoparticles: High density but sheddable PEG is a key for tumor targeting, J. Control. Release, 145 (2010) 178-181.

[33] Z.Q. Cao, S.Y. Jiang, Super-hydrophilic zwitterionic poly(carboxybetaine) and amphiphilic non-ionic poly(ethylene glycol) for stealth nanoparticles, Nano Today, 7 (2012) 404-413.

[34] L. Salvioni, M.A. Rizzuto, J.A. Bertolini, L. Pandolfi, M. Colombo, D. Prosperi, Thirty years of cancer nanomedicine: success, frustration, and hope, Cancers, 11 (2019) 1855.

[35] E. Blanco, H. Shen, M. Ferrari, Principles of nanoparticle design for overcoming biological barriers to drug delivery, Nat. Biotechnol., 33 (2015) 941-951.

[36] M.X. Yu, J. Zheng, Clearance pathways and tumor targeting of imaging nanoparticles, ACS Nano, 9 (2015) 6655-6674.

[37] M. Nurunnabi, Z. Khatun, K.M. Huh, S.Y. Park, D.Y. Lee, K.J. Cho, Y.K.

Lee, In vivo biodistribution and toxicology of carboxylated graphene quantum dots, ACS Nano, 7 (2013) 6858-6867.

[38] B. Li, L.A. Lane, Probing the biological obstacles of nanomedicine with gold nanoparticles, Wiley Interdiscip. Rev. Nanomed., 11 (2019) e1542.

[39] Y.N. Zhang, W. Poon, A.J. Tavares, I.D. McGilvray, W.C.W. Chan, Nanoparticle-liver interactions: cellular uptake and hepatobiliary elimination, J. Control. Release, 240 (2016) 332-348.

[40] M. Longmire, P.L. Choyke, H. Kobayashi, Clearance properties of nano-sized particles and molecules as imaging agents: considerations and caveats, Nanomedicine, 3 (2008) 703-717.

[41] Y.H. Cheng, C.L. He, J.E. Riviere, N.A. Monteiro-Riviere, Z.M. Lin, Meta-analysis of nanoparticle delivery to tumors using a physiologically based pharmacokinetic modeling and simulation approach, ACS Nano, 14 (2020) 3075-3095.

[42] T. Lammers, Macro-nanomedicine: targeting the big picture, J. Control. Release, 294 (2019) 372-375.

[43] J.B. Liu, M.X. Yu, C. Zhou, J. Zheng, Renal clearable inorganic nanoparticles: a new frontier of bionanotechnology, Mater Today, 16 (2013) 477-486.

[44] C. Zhou, M. Long, Y.P. Qin, X.K. Sun, J. Zheng, Luminescent gold nanoparticles with efficient renal clearance, Angew. Chem., Int. Ed., 50 (2011) 3168-3172.

[45] C. Zhou, G.Y. Hao, P. Thomas, J.B. Liu, M.X. Yu, S.S. Sun, O.K. Oz,

X.K. Sun, J. Zheng, Near-infrared emitting radioactive gold nanoparticles with molecular pharmacokinetics, Angew. Chem., Int. Ed., 51 (2012) 10118-10122.

[46] J.B. Liu, M.X. Yu, C. Zhou, S.Y. Yang, X.H. Ning, J. Zheng, Passive tumor targeting of renal-clearable luminescent gold nanoparticles: long tumor retention and fast normal tissue clearance, J. Am. Chem. Soc., 135 (2013) 4978-4981.

[47] A.A. Burns, J. Vider, H. Ow, E. Herz, O. Penate-Medina, M. Baumgart, S.M. Larson, U. Wiesner, M. Bradbury, Fluorescent silica nanoparticles with efficient urinary excretion for nanomedicine, Nano Lett., 9 (2009) 442-448.

[48] A. Ruggiero, C.H. Villa, E. Bander, D.A. Rey, M. Bergkvist, C.A. Batt, K. Manova-Todorova, W.M. Deen, D.A. Scheinberg, M.R. McDevitt, Paradoxical glomerular filtration of carbon nanotubes, Proc Natl Acad Sci U S A, 107 (2010) 12369-12374.

[49] C.Q. Peng, Y.Y. Huang, J. Zheng, Renal clearable nanocarriers: Overcoming the physiological barriers for precise drug delivery and clearance, J. Control. Release, 322 (2020) 64-80.

[50] C. Peng, J. Xu, M. Yu, X. Ning, Y. Huang, B. Du, E. Hernandez, P. Kapur, J.T. Hsieh, J. Zheng, Tuning the in vivo transport of anticancer drugs using renal-clearable gold nanoparticles, Angew. Chem., Int. Ed., 58 (2019) 8479-8483.

[51] J. Liu, M. Yu, X. Ning, C. Zhou, S. Yang, J. Zheng, PEGylation and

zwitterionization: pros and cons in the renal clearance and tumor targeting of near-IR-emitting gold nanoparticles, Angew. Chem., Int. Ed., 52 (2013) 12572-12576.

[52] H. Kang, W.R. Stiles, Y. Baek, S. Nomura, K. Bao, S. Hu, G.K. Park, M.J. Jo, H. I, J.L. Coll, B.P. Rubin, H.S. Choi, Renal clearable theranostic nanoplatforms for gastrointestinal stromal tumors, Adv. Mater., 32 (2020) e1905899.

[53] H. Kang, J. Gravier, K. Bao, H. Wada, J.H. Lee, Y. Baek, G. El Fakhri, S. Gioux, B.P. Rubin, J.L. Coll, H.S. Choi, Renal clearable organic nanocarriers for bioimaging and drug delivery, Adv. Mater., 28 (2016) 8162-8168.

[54] H. Wang, D.Q. Yu, J. Fang, C.C. Cao, Z. Liu, J.S. Ren, X.G. Qu, Renal-clearable porphyrinic metal-organic framework nanodots for enhanced photodynamic therapy, ACS Nano, 13 (2019) 9206-9217.

[55] H.S. Choi, W. Liu, F. Liu, K. Nasr, P. Misra, M.G. Bawendi, J.V. Frangioni, Design considerations for tumour-targeted nanoparticles, Nat. Nanotechnol., 5 (2010) 42-47.

[56] C. Zhou, M. Long, Y. Qin, X. Sun, J. Zheng, Luminescent gold nanoparticles with efficient renal clearance, Angew. Chem., Int. Ed., 50 (2011) 3168-3172.

[57] H. Huang, W. Feng, Y. Chen, J.L. Shi, Inorganic nanoparticles in clinical trials and translations, Nano Today, 35 (2020) 100972.

[58] W.N. Missaoui, R.D. Arnold, B.S. Cummings, Toxicological status of

nanoparticles: What we know and what we don't know, Chem.-Biol. Interact., 295 (2018) 1-12.

[59] J.R. Lakkakula, R.W. Macedo Krause, A vision for cyclodextrin nanoparticles in drug delivery systems and pharmaceutical applications, Nanomedicine (Lond), 9 (2014) 877-894.

[60] B. Gidwani, A. Vyas, A comprehensive review on cyclodextrin-based carriers for delivery of chemotherapeutic cytotoxic anticancer drugs, Biomed Res. Int, 2015 (2015) 198268.

[61] R. Challa, A. Ahuja, J. Ali, R.K. Khar, Cyclodextrins in drug delivery: An updated review, AAPS PharmSciTech, 6 (2005) E329-357

[62] J. Szejtli, Introduction and general overview of cyclodextrin chemistry, Chem. Rev., 98 (1998) 1743-1753.

[63] E.M.M. Del Valle, Cyclodextrins and their uses: a review, Process Biochem, 39 (2004) 1033-1046.

[64] A. Okamatsu, K. Motoyama, R. Onodera, T. Higashi, T. Koshigoe, Y. Shimada, K. Hattori, T. Takeuchi, H. Arima, Folate-appended beta-cyclodextrin as a promising tumor targeting carrier for antitumor drugs in vitro and in vivo, Bioconjugate Chem, 24 (2013) 724-733.

[65] S.M.L. Gontijo, P.P.G. Guimaraes, C.T.R. Viana, A.M.L. Denadai, A.D.M. Gomes, P.P. Campos, S.P. Andrade, R.D. Sinisterra, M.E. Cortes, Erlotinib/hydroxypropyl-beta-cyclodextrin inclusion complex: characterization and in vitro and in vivo evaluation, J. Incl. Phenom. Macrocycl. Chem., 83 (2015) 267-279.

[66] C. Yuan, Z.Y. Jin, X.M. Xu, Inclusion complex of astaxanthin with hydroxypropyl-beta-cyclodextrin: UV, FTIR, ^{1}H NMR and molecular modeling studies, Carbohy. Polym., 89 (2012) 492-496.

[67] B. Vaidya, V. Parvathaneni, N.S. Kulkarni, S.K. Shukla, J.K. Damon, A. Sarode, D. Kanabar, J.V. Garcia, S. Mitragotri, A. Muth, V. Gupta, Cyclodextrin modified erlotinib loaded PLGA nanoparticles for improved therapeutic efficacy against non-small cell lung cancer, Int. J. Biol. Macromol., 122 (2019) 338-347.

[68] H.Z. Bai, J.W. Wang, C.U. Phan, Q. Chen, X.R. Hu, G.Q. Shao, J. Zhou, L.H. Lai, G.P. Tang, Cyclodextrin-based host-guest complexes loaded with regorafenib for colorectal cancer treatment, Nat. Commun., 12 (2021) 759.

[69] A.A. Sandilya, U. Natarajan, M.H. Priya, Molecular view into the cyclodextrin cavity: structure and hydration, ACS Omega, 5 (2020) 25655-25667.

[70] S. Jacob, A.B. Nair, Cyclodextrin complexes: Perspective from drug delivery and formulation, Drug Develop Res, 79 (2018) 201-217.

[71] S.M. Simoes, A. Rey-Rico, A. Concheiro, C. Alvarez-Lorenzo, Supramolecular cyclodextrin-based drug nanocarriers, Chem. Commun., 51 (2015) 6275-6289.

[72] W. Xu, X. Li, L. Wang, S. Li, S. Chu, J. Wang, Y. Li, J. Hou, Q. Luo, J. Liu, Design of cyclodextrin-based functional systems for biomedical applications, Front Chem, 9 (2021) 635507.

[73] R. Namgung, Y. Mi Lee, J. Kim, Y. Jang, B.H. Lee, I.S. Kim, P. Sokkar, Y.M. Rhee, A.S. Hoffman, W.J. Kim, Poly-cyclodextrin and poly-paclitaxel nano-assembly for anticancer therapy, Nat. Commun., 5 (2014) 3702.

[74] J.M. Benito, M. Gomez-Garcia, C. Ortiz Mellet, I. Baussanne, J. Defaye, J.M. Garcia Fernandez, Optimizing saccharide-directed molecular delivery to biological receptors: design, synthesis, and biological evaluation of glycodendrimer-cyclodextrin conjugates, J. Am. Chem. Soc., 126 (2004) 10355-10363.

[75] H. Kim, J. Han, J.H. Park, Cyclodextrin polymer improves atherosclerosis therapy and reduces ototoxicity, J. Control. Release, 319 (2020) 77-86.

[76] C. Phan, Z.Y. Zheng, J.W. Wang, Q.W. Wang, X.R. Hu, G.P. Tang, H.Z. Bai, Enhanced antitumour effect for hepatocellular carcinoma in the advanced stage using a cyclodextrin-sorafenib-chaperoned inclusion complex, Biomater. Sci., 7 (2019) 4758-4768.

[77] Y. Kubota, M. Fukuda, M. Muroguchi, K. Koizumi, Absorption, distribution and excretion of beta-cyclodextrin and glucosyl-beta-cyclodextrin in rats, Biol. Pharm. Bull., 19 (1996) 1068-1072.

[78] Y.L. Luo, R.X. Rong, J.M. Li, X. Chen, S.S. Wang, X.L. Li, K.R. Wang, Effective renal clearance and photothermal therapy of a cyclodextrin-modified quaterrylene derivative, Acs Appl Bio Mater, 3 (2020) 3390-3400.

[79] J.G. Huang, S. Weinfurter, P.C. Pinto, M. Pretze, B. Kranzlin, J. Pill, R. Federica, R. Perciaccante, L. Della Ciana, R. Masereeuw, N. Gretz, Fluorescently labeled cyclodextrin derivatives as exogenous markers for real-time transcutaneous measurement of renal function, Bioconjugate Chem, 27 (2016) 2513-2526.

[80] J.G. Huang, Y. Lyu, J.C. Li, P.H. Cheng, Y.Y. Jiang, K.Y. Pu, A renal-clearable duplex optical reporter for real-time imaging of contrast-induced acute kidney injury, Angew. Chem., Int. Ed., 58 (2019) 17796-17804.

[81] J.G. Huang, C. Xie, X.D. Zhang, Y.Y. Jiang, J.C. Li, Q.L. Fan, K.Y. Pu, Renal-clearable molecular semiconductor for second near-infrared fluorescence imaging of kidney dysfunction, Angew. Chem., Int. Ed., 58 (2019) 15120-15127.

[82] H. Kang, S. Rho, W.R. Stiles, S. Hu, Y. Baek, D.W. Hwang, S. Kashiwagi, M.S. Kim, H.S. Choi, Size-dependent EPR effect of polymeric manoparticles on tumor targeting, Adv. Healthc. Mater., 9 (2020) 1901223.

[83] H.S. Choi, S.L. Gibbs, J.H. Lee, S.H. Kim, Y. Ashitate, F.B. Liu, H. Hyun, G. Park, Y. Xie, S. Bae, M. Henary, J.V. Frangioni, Targeted zwitterionic near-infrared fluorophores for improved optical imaging, Nat. Biotechnol., 31 (2013) 148-153.

[84] F.P.R. Verbeek, J.R. van der Vorst, Q.R.J.G. Tummers, M.C. Boonstra, K.E. de Rooij, C.W.G.M. Lowik, A.R.P.M. Valentijn, C.J.H. van de

Velde, H.S. Choi, J.V. Frangioni, A.L. Vahrmeijer, Near-infrared fluorescence imaging of both colorectal cancer and ureters using a low-dose integrin targeted probe, Ann. Surg. Oncol. 21 (2014) S528-S537.

[85] A.M. Sofias, Y.C. Toner, A.E. Meerwaldt, M.M.T. van Leent, G. Soultanidis, M. Elschot, H. Gonai, K. Grendstad, A. Flobak, U. Neckmann, C. Wolowczyk, E.L. Fisher, T. Reiner, C.D. Davies, G. Bjorkoy, A.J.P. Teunissen, J. Ochando, C. Perez-Medina, W.J.M. Mulder, S. Hak, Tumor targeting by αvβ3-integrin-specific lipid nanoparticles occurs via phagocyte hitchhiking, ACS Nano, 14 (2020) 7832-7846.

[86] K.M. McNeeley, A. Annapragada, R.V. Bellamkonda, Decreased circulation time offsets increased efficacy of PEGylated nanocarriers targeting folate receptors of glioma, Nanotechnology, 18 (2007) 385101.

[87] A.J. Shuhendler, P. Prasad, M. Leung, A.M. Rauth, R.S. DaCosta, X.Y. Wu, A novel solid lipid nanoparticle formulation for active targeting to tumor αvβ3 integrin receptors reveals cyclic RGD as a double-edged sword, Adv. Healthc. Mater., 1 (2012) 600-608.

[88] W.W. Cheng, T.M. Allen, Targeted delivery of anti-CD19 liposomal doxorubicin in B-cell lymphoma: a comparison of whole monoclonal antibody, Fab' fragments and single chain Fv, J. Control. Release, 126 (2008) 50-58.

[89] Y. Zhang, J. Cao, Z. Yuan, Strategies and challenges to improve the performance of tumor-associated active targeting, J Mater Chem B, 8 (2020) 3959-3971.

[90] Z. Zhao, A. Ukidve, J. Kim, S. Mitragotri, Targeting strategies for tissue-specific drug delivery, Cell, 181 (2020) 151-167.

[91] F. Bray, J. Ferlay, I. Soerjomataram, R.L. Siegel, L.A. Torre, A. Jemal, Global cancer statistics 2018: GLOBOCAN estimates of incidence and mortality worldwide for 36 cancers in 185 countries, CA: Cancer J. Clin., 68 (2018) 394-424.

[92] A. Carrato, Adjuvant treatment of colorectal cancer, Gastrointest Cancer Res., 2 (2008) S42-46.

[93] N.J. McCleary, A.B. Benson, 3rd, R. Dienstmann, Personalizing adjuvant therapy for stage II/III colorectal cancer, Am. Soc. Clin. Oncol. Educ. Book, 37 (2017) 232-245.

[94] H. Jalaeikhoo, M. Zokaasadi, A. Khajeh-Mehrizi, M. Rajaeinejad, S.A. Mousavi, M. Vaezi, H.K. Fumani, M. Keyhani, K. Alimoghaddam, A. Ghavamzadeh, Effectiveness of adjuvant chemotherapy in patients with Stage II colorectal cancer: A multicenter retrospective study, J Res Med Sci, 24 (2019) 39.

[95] J. Taieb, C. Gallois, Adjuvant chemotherapy for stage III colon cancer, Cancers, 12 (2020) 2679.

[96] M.S. Braun, M.T. Seymour, Balancing the efficacy and toxicity of chemotherapy in colorectal cancer, Ther. Adv. Med. Oncol., 3 (2011) 43-52.

[97] Y.H. Xie, Y.X. Chen, J.Y. Fang, Comprehensive review of targeted therapy for colorectal cancer, Signal Transduct Target Ther., 5 (2020) 22.

[98] R. Dwivedi, P. Aggarwal, N.S. Bhavesh, K.J. Kaur, Design of therapeutically improved analogue of the antimicrobial peptide, indolicidin, using a glycosylation strategy, Amino Acids, 51 (2019) 1443-1460.

[99] H. Kasashima, A. Duran, T. Cid-Diaz, Y. Muta, H. Kinoshita, E. Batlle, M.T. Diaz-Meco, J. Moscat, Mouse model of colorectal cancer: orthotopic co-implantation of tumor and stroma cells in cecum and rectum, STAR Protocols, 2 (2021) 100297.

[100] J.M. Benito, M. Gomez-Garcia, C.O. Mellet, I. Baussanne, J. Defaye, J.M.G. Fernandez, Optimizing saccharide-directed molecular delivery to biological receptors: design, synthesis, and biological evaluation of glycodendrimer - cyclodextrin conjugates, J. Am. Chem. Soc., 126 (2004) 10355-10363.

[101] Q. Shao, S.Y. Jiang, Influence of charged groups on the properties of zwitterionic moieties: a molecular simulation study, J. Phys. Chem. B, 118 (2014) 7630-7637.

[102] E. van Andel, S.C. Lange, S.P. Pujari, E.J. Tijhaar, M.M.J. Smulders, H.F.J. Savelkoul, H. Zuilhof, Systematic comparison of zwitterionic and non-zwitterionic antifouling polymer brushes on a bead-based platform, Langmuir, 35 (2019) 1181-1191.

[103] S. Deshayes, H. Cabral, T. Ishii, Y. Miura, S. Kobayashi, T. Yamashita, A. Matsumoto, Y. Miyahara, N. Nishiyama, K. Kataoka, Phenylboronic acid-installed polymeric micelles for targeting sialylated epitopes in

solid tumors, J. Am. Chem. Soc., 135 (2013) 15501-15507.

[104] J.Y. Lee, S.J. Chung, H.J. Cho, D.D. Kim, Phenylboronic acid-decorated chondroitin sulfate A-based theranostic nanoparticles for enhanced tumor targeting and penetration, Adv. Funct. Mater., 25 (2015) 3705-3717.

[105] H. Liu, Y. Li, K. Sun, J. Fan, P. Zhang, J. Meng, S. Wang, L. Jiang, Dual-responsive surfaces modified with phenylboronic acid-containing polymer brush to reversibly capture and release cancer cells, J. Am. Chem. Soc., 135 (2013) 7603-7609.

[106] L.D. Blackman, P.A. Gunatillake, P. Cass, K.E.S. Locock, An introduction to zwitterionic polymer behavior and applications in solution and at surfaces, Chem. Soc. Rev., 48 (2019) 757-770.

[107] H.W. Ooi, J.M.M. Kocken, F.L.C. Morgan, A. Malheiro, B. Zoetebier, M. Karperien, P.A. Wieringa, P.J. Dijkstra, L. Moroni, M.B. Baker, Multivalency enables dynamic supramolecular host-guest hydrogel formation, Biomacromolecules, 21 (2020) 2208-2217.

[108] D.W. Lee, J. Jo, D. Jo, J. Kim, J.J. Min, D.H. Yang, H. Hyun, Supramolecular assembly based on host-guest interaction between beta-cyclodextrin and adamantane for specifically targeted cancer imaging, J Ind Eng Chem, 57 (2018) 37-44.

[109] X.D. Xu, H. Cheng, W.H. Chen, S.X. Cheng, R.X. Zhuo, X.Z. Zhang, In situ recognition of cell-surface glycans and targeted imaging of cancer cells, Sci. Rep., 3 (2013) 2679.

[110] A. Okamatsu, K. Motoyama, R. Onodera, T. Higashi, T. Koshigoe, Y. Shimada, K. Hattori, T. Takeuchi, H. Arima, Design and evaluation of folate-appended α-, β-, and γ-cyclodextrins having a caproic acid as a tumor selective antitumor drug carrier in vitro and in vivo, Biomacromolecules, 14 (2013) 4420-4428.

[111] H. Hyun, M. Henary, T. Gao, L. Narayana, E.A. Owens, J.H. Lee, G. Park, H. Wada, Y. Ashitate, J.V. Frangioni, H.S. Choi, 700-nm zwitterionic near-infrared fluorophores for dual-channel image-guided surgery, Mol. Imaging Biol, 18 (2016) 52-61.

[112] Q. Shao, S. Jiang, Influence of charged groups on the properties of zwitterionic moieties: a molecular simulation study, J. Phys. Chem. B, 118 (2014) 7630-7637.

[113] H.A. Galema, R.P.J. Meijer, L.J. Lauwerends, C. Verhoef, J. Burggraaf, A.L. Vahrmeijer, M. Hutteman, S. Keereweer, D.E. Hilling, Fluorescence-guided surgery in colorectal cancer; a review on clinical results and future perspectives, Eur. J. Surg. Oncol., 48 (2022) 810-821.

[114] K.R. Tringale, J. Pang, Q.T. Nguyen, Image-guided surgery in cancer: A strategy to reduce incidence of positive surgical margins, Wiley Interdiscip Rev Syst Biol Med, 10 (2018) e1412.

[115] P.D. Garjio, O.M. Sáez, M. Caldera, A. L López, A.M. Lacy, F.B. Lacy, Wang, Applications of indocyanine green fluorescence imaging in colorectal surgery: a narrative review, Ann. Laparosc. Endosc. Surg., 7 (2022) 22-38

[116] A. Shukla, J.M. Hillegass, M.B. MacPherson, S.L. Beuschel, P.M. Vacek, H.I. Pass, M. Carbone, J.R. Testa, B.T. Mossman, Blocking of ERK1 and ERK2 sensitizes human mesothelioma cells to doxorubicin, Molecular Cancer, 9 (2010) 314.

[117] I.C. Salaroglio, E. Mungo, E. Gazzano, J. Kopecka, C. Riganti, ERK is a pivotal player of chemo-immune-resistance in cancer, Int. J. Mol. Sci., 20 (2019) 2505.

[118] C. Christowitz, T. Davis, A. Isaacs, G. van Niekerk, S. Hattingh, A.M. Engelbrecht, Mechanisms of doxorubicin-induced drug resistance and drug resistant tumour growth in a murine breast tumour model, BMC Cancer, 19 (2019) 757.

[119] R. Ortiz, F. Quinonero, B. Garcia-Pinel, M. Fuel, C. Mesas, L. Cabeza, C. Melguizo, J. Prados, Nanomedicine to overcome multidrug resistance mechanisms in colon and pancreatic cancer: recent progress, Cancers (Basel), 13 (2021) 2058.

[120] D.H. Kim, C.H. Jeong, W.N. Cheng, H.C. Kwon, D.H. Kim, K.H. Seo, Y. Choi, S.G. Han, Effects of kefir on doxorubicin-induced multidrug resistance in human colorectal cancer cells, J. Funct. Foods, 78 (2021) 104371.

[121] H. Hamdi, R. Abderrahim, F. Meganem, Spectroscopic studies of inclusion complex of beta-cyclodextrin and benzidine diammonium dipicrate, Spectrochim. Acta A Mol. Biomol. Spectrosc., 75 (2010) 32-36.

[122] S. Lv, Y. Wu, K. Cai, H. He, Y. Li, M. Lan, X. Chen, J. Cheng, L. Yin, High drug loading and sub-quantitative loading efficiency of polymeric micelles driven by donor-receptor coordination interactions, J. Am. Chem. Soc., 140 (2018) 1235-1238.

[123] A.E. Hiensch, K.A. Bolam, S. Mijwel, J.A.L. Jeneson, A.D.R. Huitema, O. Kranenburg, E. van der Wall, H. Rundqvist, Y. Wengstrom, A.M. May, Doxorubicin-induced skeletal muscle atrophy: elucidating the underlying molecular pathways, Acta Physiol., 229 (2020) e13400.

[124] H.C. Ou, P.M. Chu, Y.T. Huang, H.C. Cheng, W.C. Chou, H.L. Yang, H.I. Chen, K.L. Tsai, Low-level laser prevents doxorubicin-induced skeletal muscle atrophy by modulating AMPK/SIRT1/PCG-1alpha-mediated mitochondrial function, apoptosis and up-regulation of pro-inflammatory responses, Cell Biosci., 11 (2021) 200.

[125] P.A. Henriksen, Anthracycline cardiotoxicity: an update on mechanisms, monitoring and prevention, Heart, 104 (2018) 971-977.

[126] Z. Tian, Y. Yang, Y. Yang, F. Zhang, P. Li, J. Wang, J. Yang, P. Zhang, W. Yao, X. Wang, High cumulative doxorubicin dose for advanced soft tissue sarcoma, BMC Cancer, 20 (2020) 1139.

[127] O. Tredan, C.M. Galmarini, K. Patel, I.F. Tannock, Drug resistance and the solid tumor microenvironment, J. Natl. Cancer Inst., 99 (2007) 1441-1454.

[128] S. Torok, M. Rezeli, O. Kelemen, A. Vegvari, K. Watanabe, Y. Sugihara, A. Tisza, T. Marton, I. Kovacs, J. Tovari, V. Laszlo, T.H. Helbich, B.

Hegedus, T. Klikovits, M.A. Hoda, W. Klepetko, S. Paku, G. Marko-Varga, B. Dome, Limited tumor tissue drug penetration contributes to primary resistance against angiogenesis inhibitors, Theranostics, 7 (2017) 400-412.

[129] A. Ziemys, K. Yokoi, M. Kai, Y.T. Liu, M. Kojic, V. Simic, M. Milosevic, A. Holder, M. Ferrari, Progression-dependent transport heterogeneity of breast cancer liver metastases as a factor in therapeutic resistance, J. Control. Release, 291 (2018) 99-105.

[130] H. Cabral, Y. Matsumoto, K. Mizuno, Q. Chen, M. Murakami, M. Kimura, Y. Terada, M.R. Kano, K. Miyazono, M. Uesaka, N. Nishiyama, K. Kataoka, Accumulation of sub-100 nm polymeric micelles in poorly permeable tumours depends on size, Nat. Nanotechnol., 6 (2011) 815-823.

[131] Q. Zhou, S. Shao, J. Wang, C. Xu, J. Xiang, Y. Piao, Z. Zhou, Q. Yu, J. Tang, X. Liu, Z. Gan, R. Mo, Z. Gu, Y. Shen, Enzyme-activatable polymer-drug conjugate augments tumour penetration and treatment efficacy, Nat. Nanotechnol., 14 (2019) 799-809.

[132] R.K. Jain, T. Stylianopoulos, Delivering nanomedicine to solid tumors, Nat. Rev. Clin. Oncol., 7 (2010) 653-664.

[133] M.K. Shim, J. Park, H.Y. Yoon, S. Lee, W. Um, J.H. Kim, S.W. Kang, J.W. Seo, S.W. Hyun, J.H. Park, Y. Byun, I.C. Kwon, K. Kim, Carrier-free nanoparticles of cathepsin B-cleavable peptide-conjugated doxorubicin prodrug for cancer targeting therapy, J. Control. Release,

294 (2019) 376-389.

[134] S. Yang, M.K. Shim, W.J. Kim, J. Choi, G.H. Nam, J. Kim, J. Kim, Y. Moon, H.Y. Kim, J. Park, Y. Park, I.S. Kim, J.H. Ryu, K. Kim, Cancer-activated doxorubicin prodrug nanoparticles induce preferential immune response with minimal doxorubicin-related toxicity, Biomaterials, 272 (2021) 120791.

Table 1. Physicochemical properties of five candidates with high colloidal stability.

Physicochemical property	CD 16	CD 17	CD 18	CD 19	CD 20
Net charge	Zwitterionic	Zwitterionic	Negative	Positive	Neutral
Molecular weight [g mol^{-1}]	9,304	9,788	9,039	9,032	8,745
Hydrodynamic diameter [nm]	6.19 ± 0.19	6.58 ± 0.27	5.05 ± 0.08	6.15 ± 0.15	6.08 ± 0.09
Zeta potential [mV]	0.95 ± 0.64	0.65 ± 0.48	-7.17 ± 0.33	18.5 ± 0.27	-0.11 ± 0.25

Table 2. Pharmacokinetic parameters of free ACy7 and PBA-(ZW)-CD/ACy7 after intravenous injection at an ACy7 dose of 1 μmol kg^{-1}. Data are presented as the mean ± SD (n = 3, *p < 0.05). Abbreviations: $t_{1/2\alpha}$, distribution half-life; $t_{1/2\beta}$, elimination half-life; AUC_{last}, Area under the curve from time 0 to the time of the last sampling; Cl, total body clearance; and V_d, volume of distribution.

Parameters	ACy7	PBA-(ZW)-CD/ACy7
$t_{1/2\alpha}$ (min)	4.2 ± 1.4	3.0 ± 0.5
$t_{1/2\beta}$ (min)	92.5 ± 15.9	52.5 ± 16.7*
AUC_{last} (%ID min g^{-1})	1098.6 ± 141.0	941.1 ± 39.0
Cl (mL min^{-1})	0.08 ± 0.01	0.10 ± 0.01
V_d (mL)	7.9 ± 0.6	5.6 ± 1.3*

Table 3. Physicochemical properties, including number-weighted size distribution, mean hydrodynamic diameter (HD), and zeta potential, of inclusion complexes at pH 5.5 and 7.4.

Physicochemical properties	PBA-(ZW)-CD/DOX		PBA-(ZW)-CD/UXT	
	pH 5.5	pH 7.4	pH 5.5	pH 7.4
HD [nm]	7.09 ± 0.26	13.04 ± 3.85	6.30 ± 0.11	6.30 ± 0.09
Zeta potential [mV]	7.5 ± 0.7	2.0 ± 0.8	4.4 ± 0.7	1.7 ± 0.7

Table 4. Complete blood counts of male BALB/c mice (5 weeks old) after intravenous administration of excess PBA-(ZW)-CD (270 mg kg^{-1} day^{-1}, once or three times daily). Data are presented as the mean ± SD (n = 4). Abbreviations: WBC, white blood cell count; LYM, lymphocyte; MON, monocyte; EOS, eosinophil; RBC, red blood cell count; HCT, hematocrit; MCV, mean corpuscular volume; PLT, blood platelet count; and MPV, mean platelet volume.

Parameters [unit]	No Treatment	PBA-(ZW)-CD (270 mg kg^{-1} × 1 dose)	PBA-(ZW)-CD (270 mg kg^{-1} × 3 doses)
WBC [$10^3/mm^3$]	3.53 ± 0.38	3.08 ± 0.04	3.17 ± 0.87
LYM [%]	73.43 ± 4.44	68.15 ± 10.43	72.28 ± 1.97
MON [%]	8.00 ± 0.94	7.43 ± 1.73	7.00 ± 0.833
EOS [%]	3.13 ± 1.04	6.88 ± 2.27	4.45 ± 2.07
RBC [%]	9.05 ± 1.91	8.90 ± 0.87	9.27 ± 2.28
HCT [%]	49.83 ± 10.74	48.50 ± 5.17	51.05 ± 13.38
MCV [μm^3]	55.26 ± 0.43	54.50 ± 0.50	54.75 ± 1.09
PLT [$10^3/mm^3$]	730.00 ± 314.97	874.50 ± 231.66	505.75 ± 321.99
MPV [μm^3]	7.50 ± 0.87	7.05 ± 0.77	7.98 ± 0.70

Table 5. *In vitro* antitumor efficacies of free drug and PBA-(ZW)-CD/drug inclusion complexes in HT-29 cells. Half-maximal inhibitory concentration (IC_{50}) values are presented. Data are presented as the mean ± SD (n = 6).

Formulations	IC_{50} (μmol L^{-1})
Free DOX	1.39 ± 0.19
PBA-(ZW)-CD/DOX	0.48 ± 0.01
Free UXT	0.39 ± 0.05
PBA-(ZW)-CD/UXT	0.24 ± 0.06

Table 6. Blood biochemistry parameters after five rounds of treatment (3 mg kg^{-1} as each drug) (refer to Figure 34A). Data are presented as the mean ± SD (n = 8). Abbreviations: ALT, alanine transaminase; AST, aspartate transaminase; ALP, alkaline phosphatase; BUN, blood urea nitrogen; and SCr, serum creatinine.

Parameters	PBS	PBA-(ZW)-CD	DOX solution	UXT solution	DOX + UXT solution	PBA-(ZW)-CD/DOX + PBA-(ZW)-CD/UXT
ALT [U L^{-1}]	19.0 ± 2.4	21 ± 2.9	23.3 ± 3.8	20.3 ± 1.6	21.3 ± 3.0	22.5 ± 2.9
AST [U L^{-1}]	48.0 ± 14.3	52.0 ± 12.4	78.0 ± 40.9	67.3 ± 46.7	46.5 ± 18.8	52.8 ± 12.8
ALP [U L^{-1}]	341.0 ± 32.4	320.8 ± 30.7	333.5 ± 20.4	296.8 ± 43.5	323.3 ± 52.5	322.8 ± 45.2
BUN [mg dL^{-1}]	18.0 ± 2.5	19.7 ± 2.0	16.7 ± 1.2	20.5 ± 2.2	18.6 ± 1.5	16.0 ± 2.9
SCr [mg dL^{-1}]	0.1 ± 0.01	0.1 ± 0.03	0.1 ± 0.01	0.1 ± 0.05	0.1 ± 0.02	0.1 ± 0.01

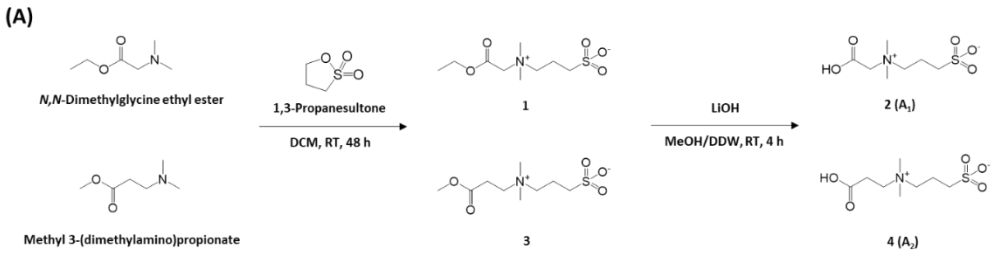
(A)
N,N-Dimethylglycine ethyl ester
1,3-Propanesultone
DCM, RT, 48 h
1
LiOH
MeOH/DDW, RT, 4 h
2 (A1)
Methyl 3-(dimethylamino)propionate
3
4 (A2)

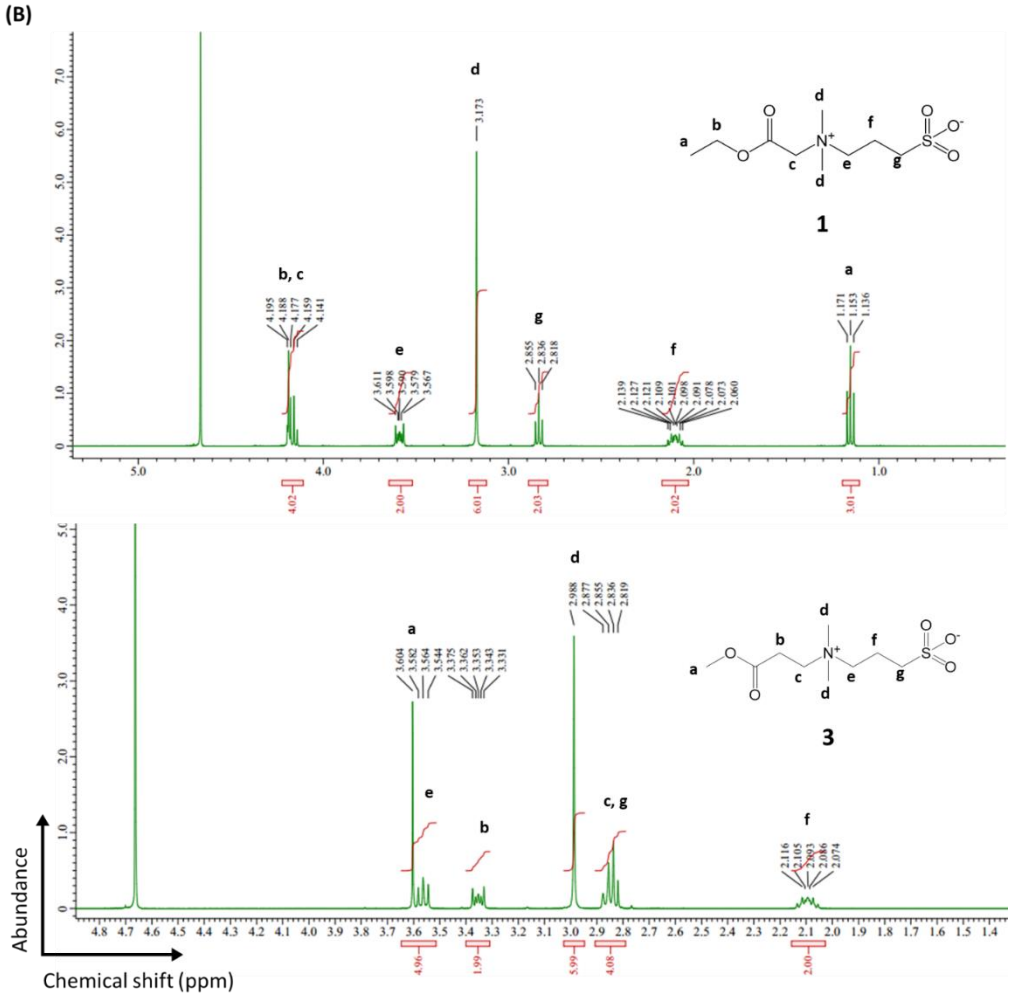
(B)
1
3
Abundance
Chemical shift (ppm)

(Continued)

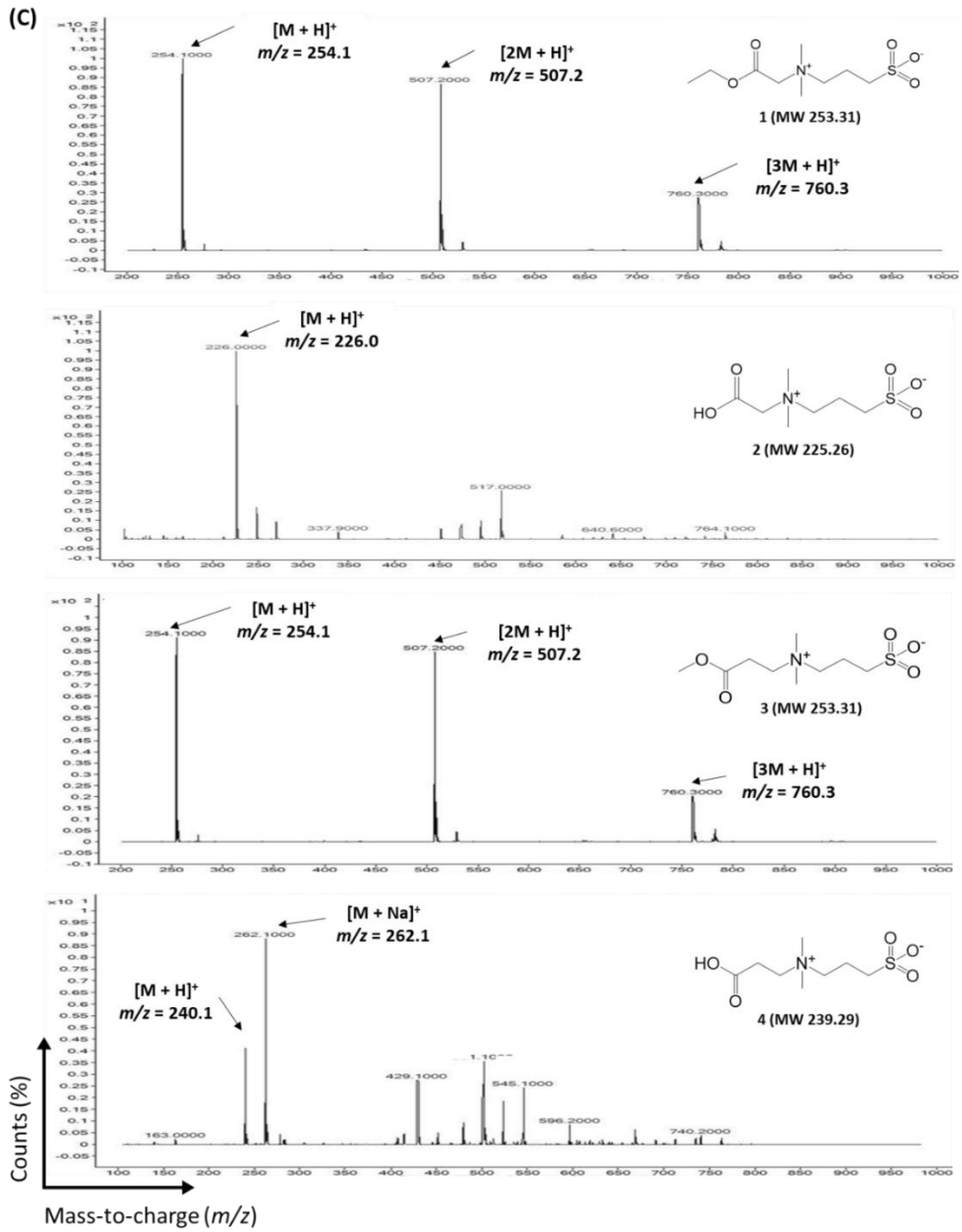

Figure 1. Synthesis of sulfobetaine **2** (A_1) and **4** (A_2) that have one and two methylene groups between quaternary ammonium and carboxylic acid, respectively. (A) Synthetic schemes of compounds **1**–**4**, (B) Proton nuclear magnetic resonance (^{1}H-NMR) spectra of compounds **1** and **3**, and (C) electrospray ionization-mass spectrometry (ESI-MS) spectra of compounds **1**–**4** are presented. Samples were dissolved in D_2O for ^{1}H-NMR analysis.

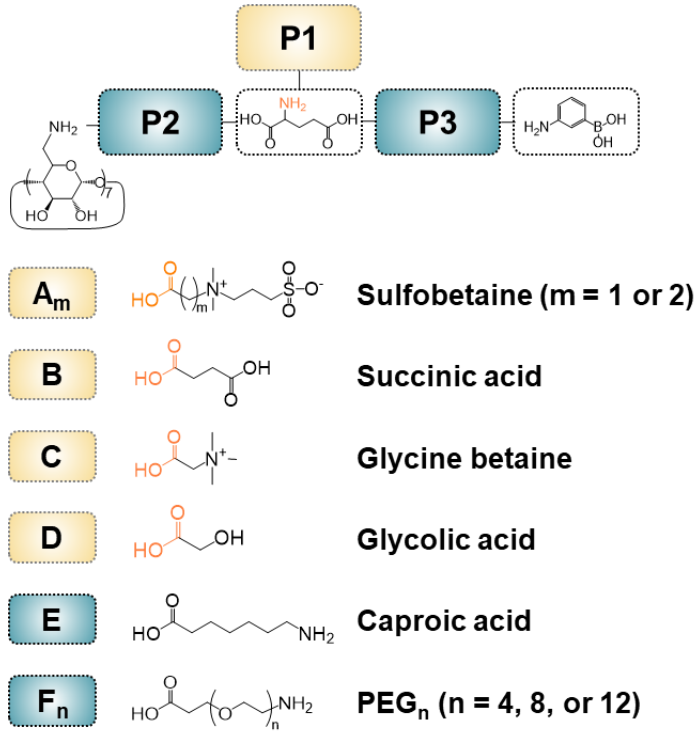

Figure 2. Schematic view of CD derivatization. The carboxylic acid of charged moieties (A_m, B, C, and D) was linked to the amine group of glutamic acid linker *via* amide bond formation (orange color) (P1). Various spacers (E and F_n) were introduced between CD ring and glutamic acid linker (P2) and glutamic acid and PBA moiety (P3).

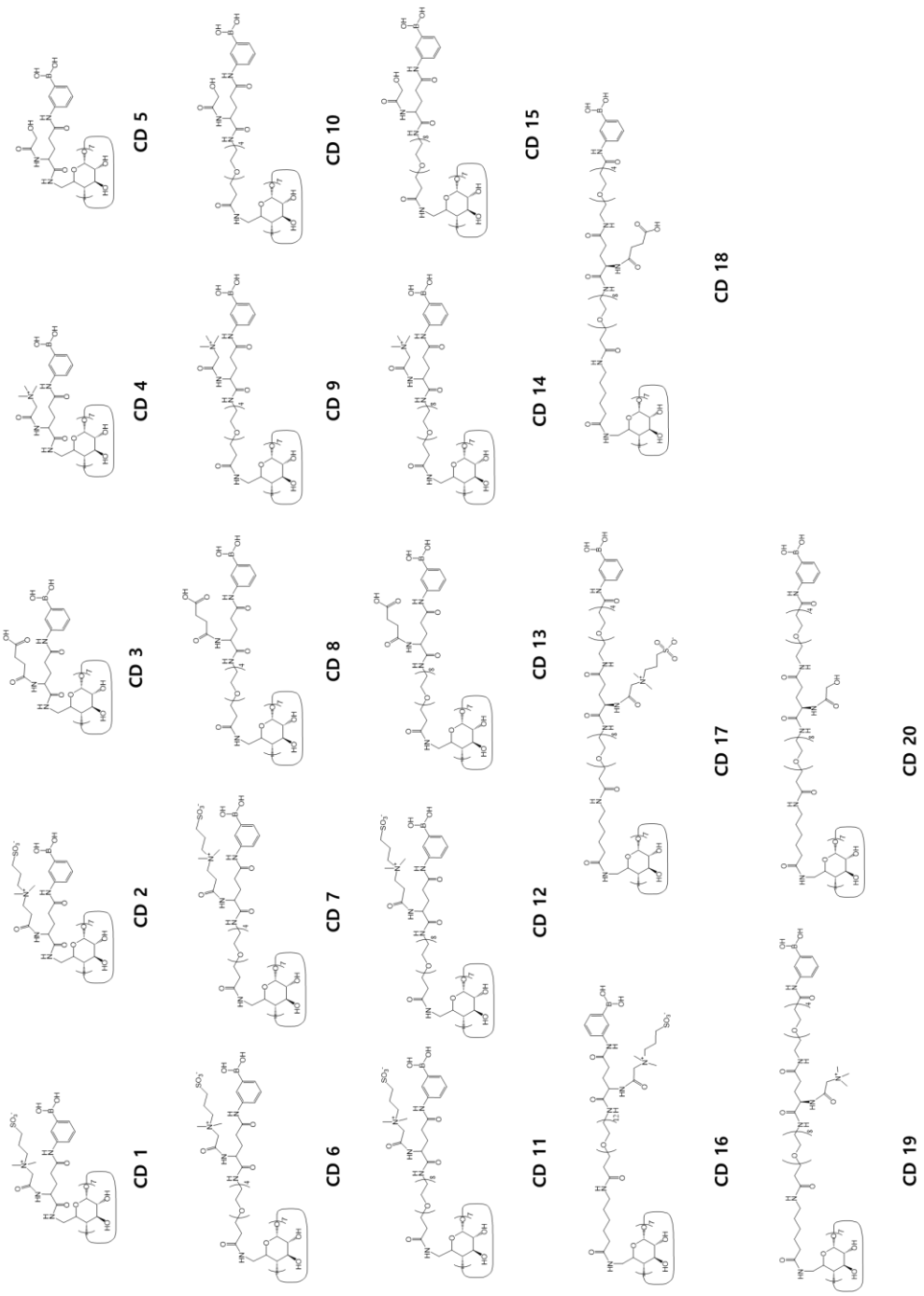

Figure 3. Structures of cyclodextrin derivatives (**CD 1–20)**.

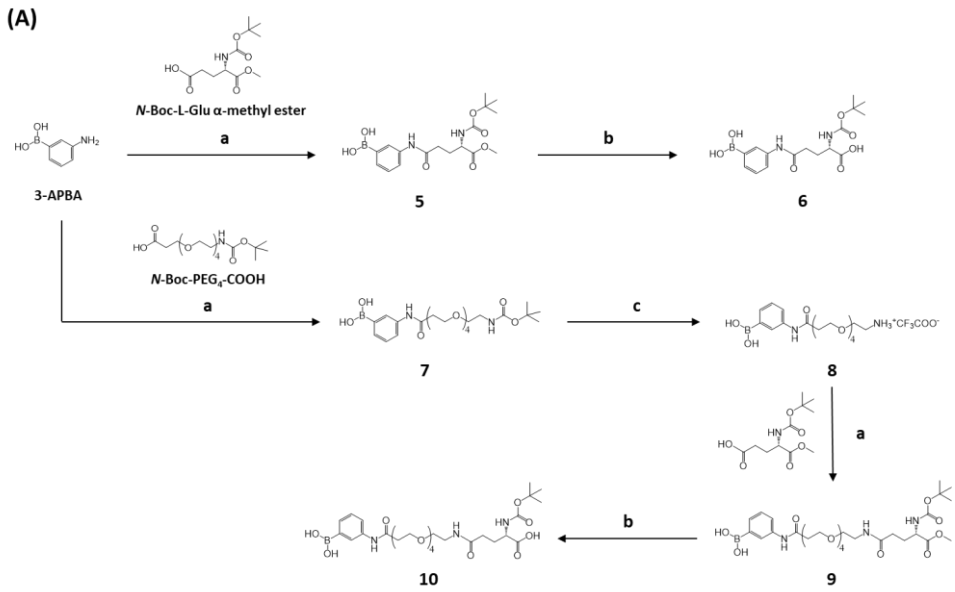
(A)
N-Boc-L-Glu α-methyl ester
a
3-APBA
5
b
6
N-Boc-PEG4-COOH
a
7
c
8
a
9
b
10

(Continued)

(B)

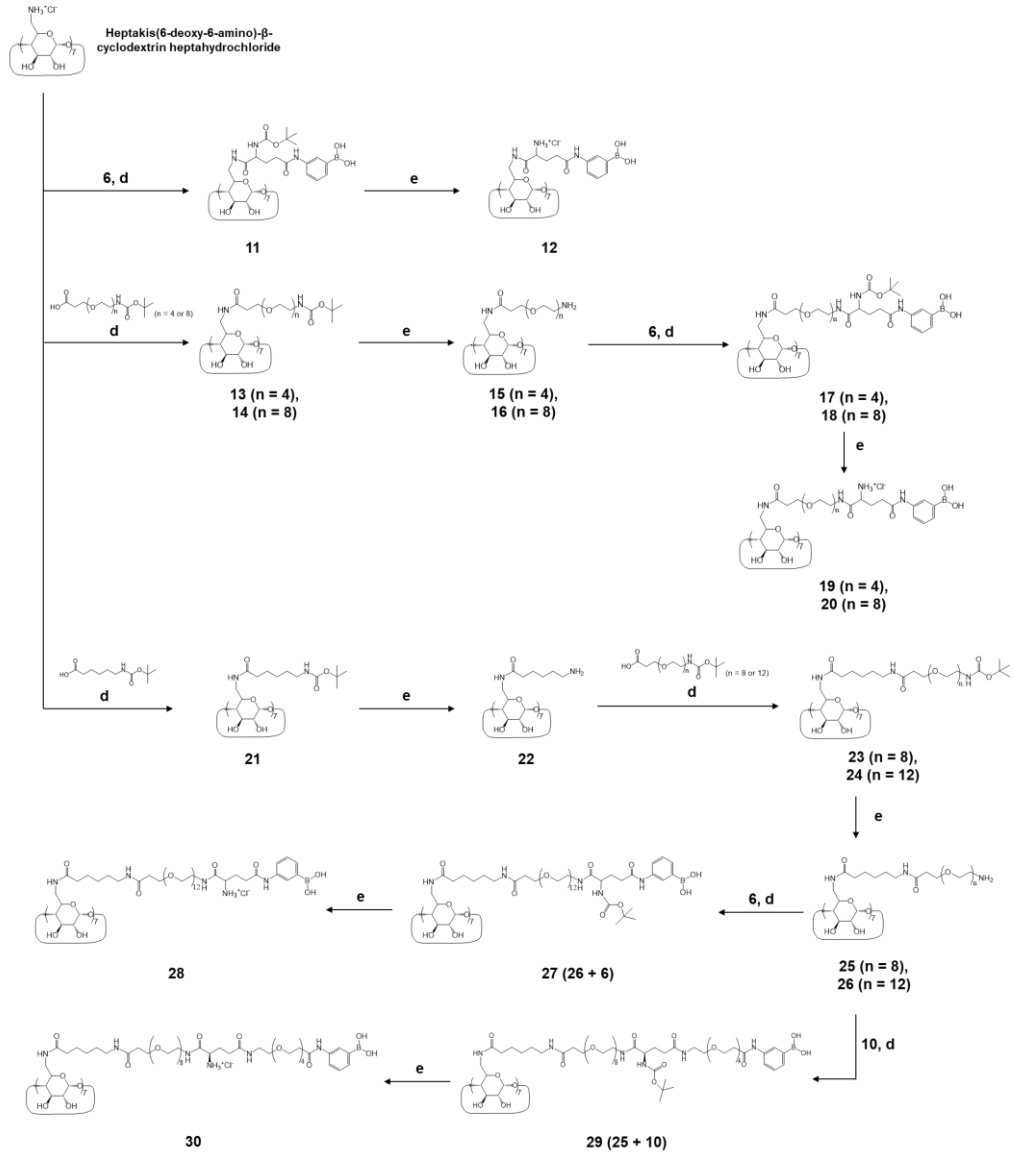
Heptakis(6-deoxy-6-amino)-β-cyclodextrin heptahydrochloride
6, d
e
11
12
d
(n = 4 or 8)
13 (n = 4),
14 (n = 8)
15 (n = 4),
16 (n = 8)
6, d
17 (n = 4),
18 (n = 8)
e
19 (n = 4),
20 (n = 8)
d
21
e
22
d
(n = 8 or 12)
23 (n = 8),
24 (n = 12)
e
25 (n = 8),
26 (n = 12)
6, d
27 (26 + 6)
e
28
10, d
29 (25 + 10)
e
30

(Continued)

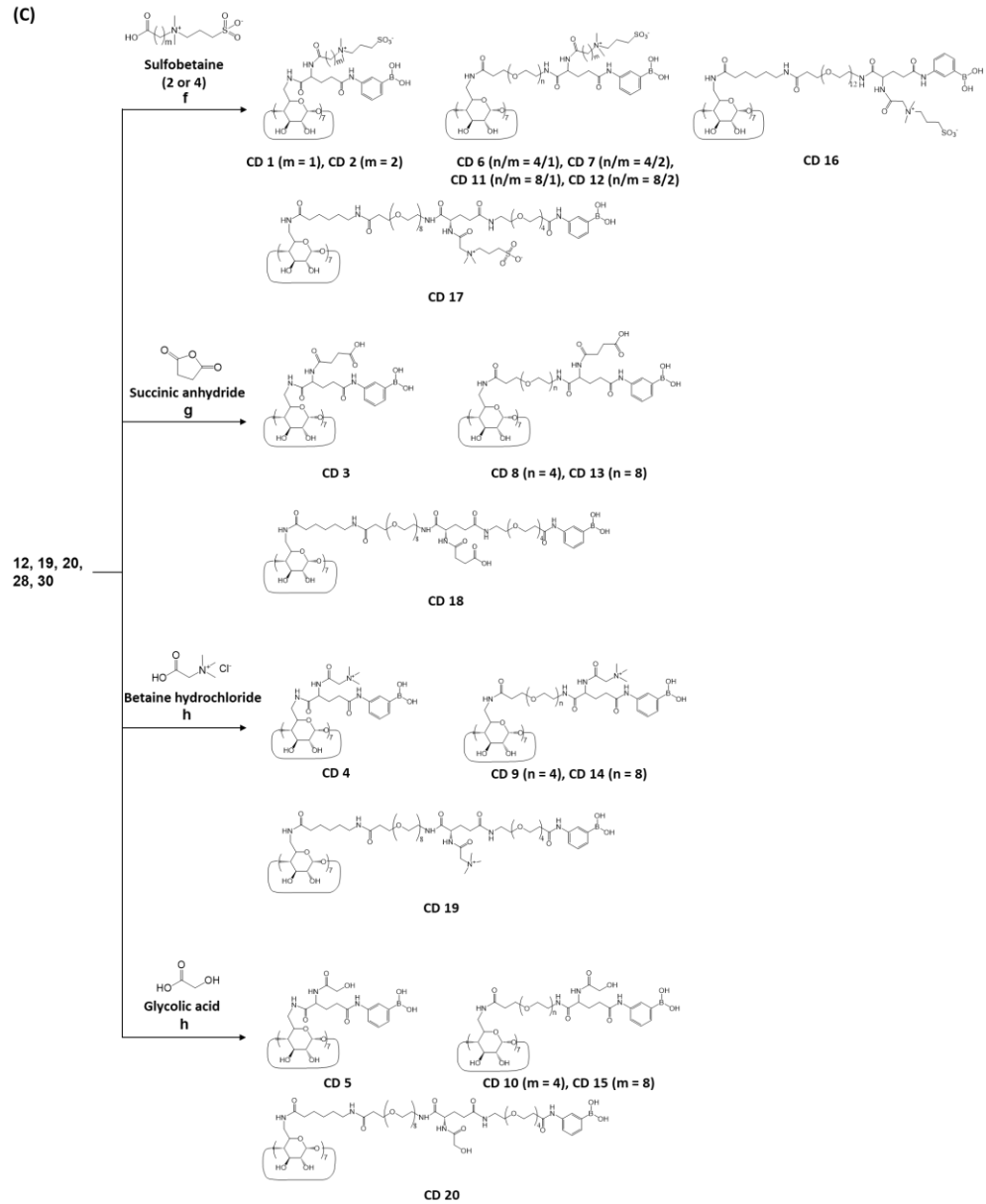

Figure 4. Synthetic schemes of cyclodextrin derivatives (**CD 1–20**). (A) Preparation of PBA moieties (compounds **6** and **10**). (B) Synthesis of PBA-conjugated CD intermediates (compounds **12**, **19**, **20**, **28**, and **30**). (C) Conjugation of charged moieties to CD intermediates to obtain **CD 1–20**. Reagents and conditions: a) *N*-([dimethylamino]-1*H*-1,2,3-triazolo-[4,5-*b*]pyridin-1-ylmethylene)-*N*-methylmethanaminium hexafluorophosphate *N*-oxide (HATU)/*N*,*N*-diisopropylethylamine (DIPEA) in *N*,*N*-

dimethylformamide (DMF), room temperature (RT), 30 h; b) LiOH in MeOH/double-deionized water (DDW), RT, 4 h; c) Trifluoroacetic acid (TFA) in dichloromethane (DCM), RT, 1 h; d) *O*-(benzotriazol-1-yl)-*N*,*N*,*N'*,*N'*-tetramethyluronium hexafluorophosphate (HBTU)/DIPEA in dimethyl sulfoxide (DMSO)/DMF, RT, 48 h; e) TFA/ACN, RT, 1.5 h; f) EDC/NHS in 2-(*N*-morpholino)ethanesulfonic acid (MES) buffer, 37 °C, 48 h; g) Triethylamine (TEA) in DMSO, RT, 48 h; and h) EDC/NHS/TEA in DMSO, RT, 48 h.

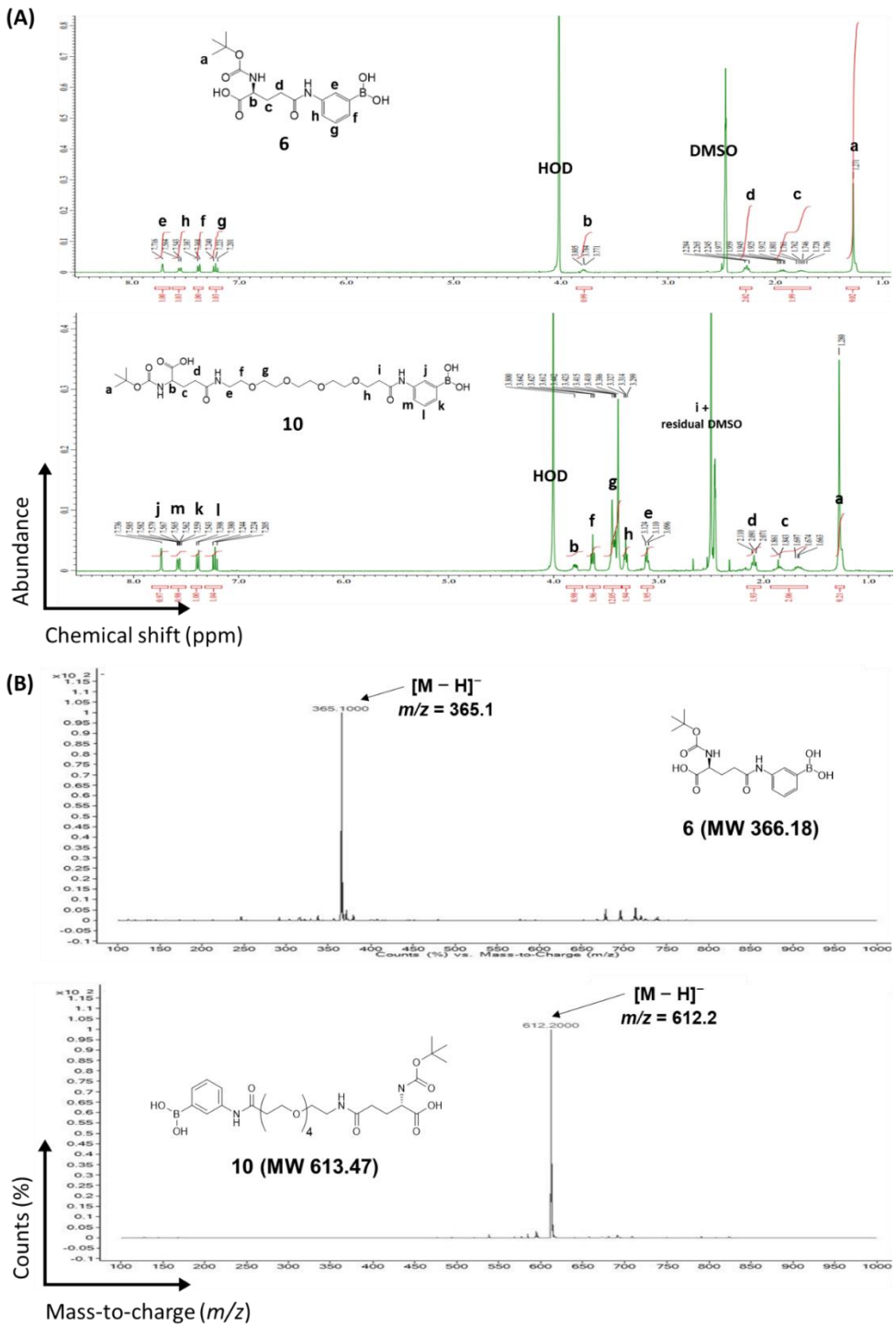

Figure 5. ^{1}H-NMR (A) and ESI-MS (B) spectra of compounds **6** and **10**. Samples were dissolved in DMSO-d_6/D_2O for ^{1}H-NMR analysis.

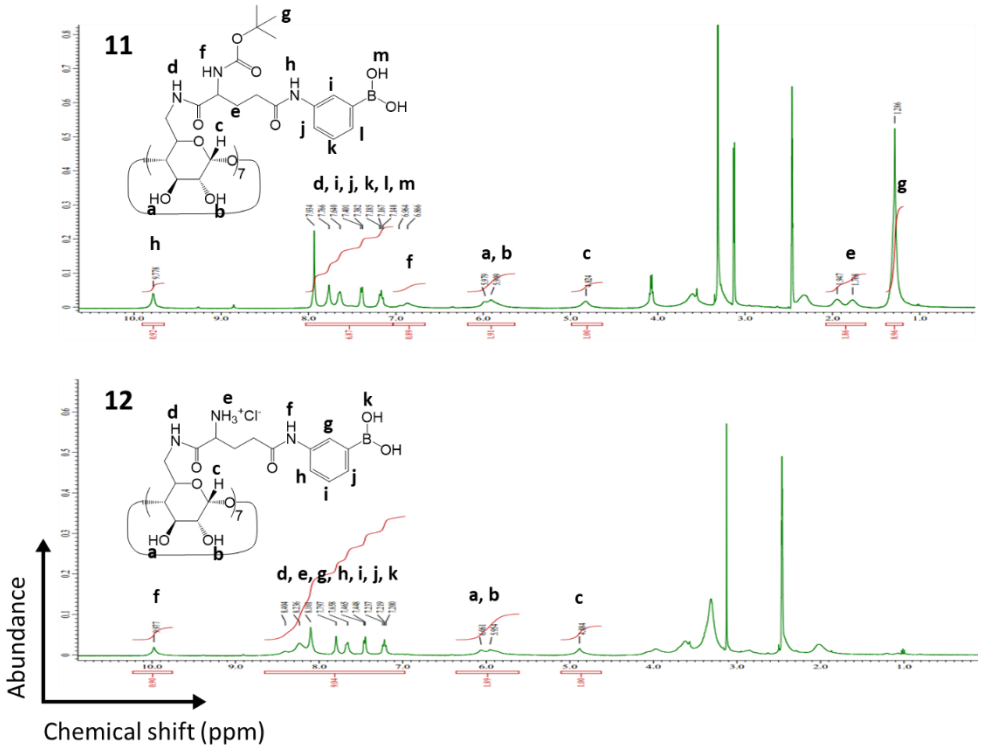

Figure 6. ^{1}H-NMR spectra of CD intermediates without spacers in the P2 position (compounds **11** and **12**). Samples were dissolved in DMSO-d_6 for ^{1}H-NMR analysis.

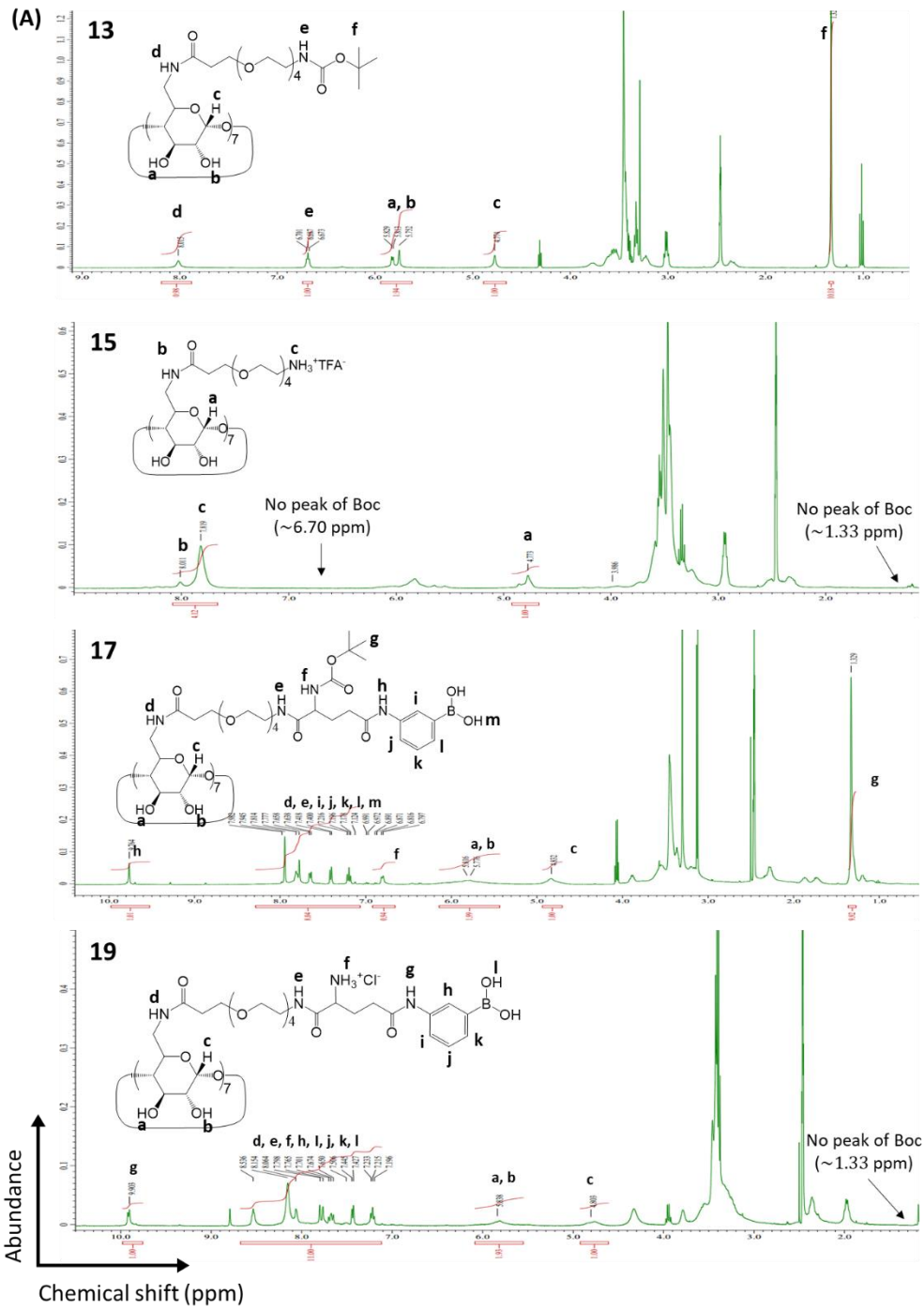
(A)
13
15
17
19
No peak of Boc
(~6.70 ppm)
No peak of Boc
(~1.33 ppm)
No peak of Boc
(~1.33 ppm)
Abundance
Chemical shift (ppm)

(Continued)

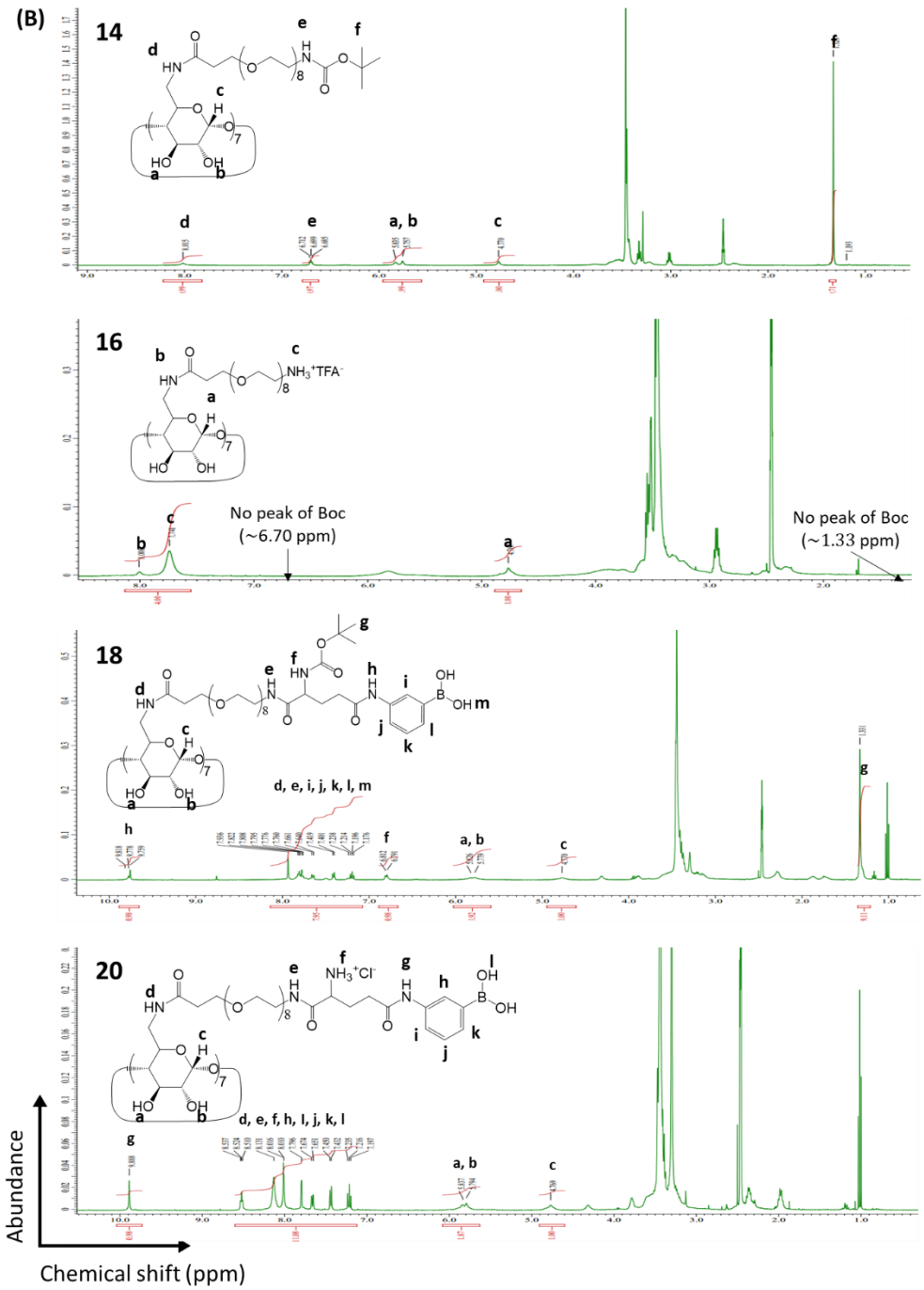

Figure 7. ^{1}H-NMR spectra of CD intermediates with PEG_4 (A; compounds **13**, **15**, **17**, and **19**) or PEG_8 (B; compounds **14**, **16**, **18**, and **20**) spacer in the P2 position. Samples were dissolved in DMSO-d_6 for ^{1}H-NMR analysis.

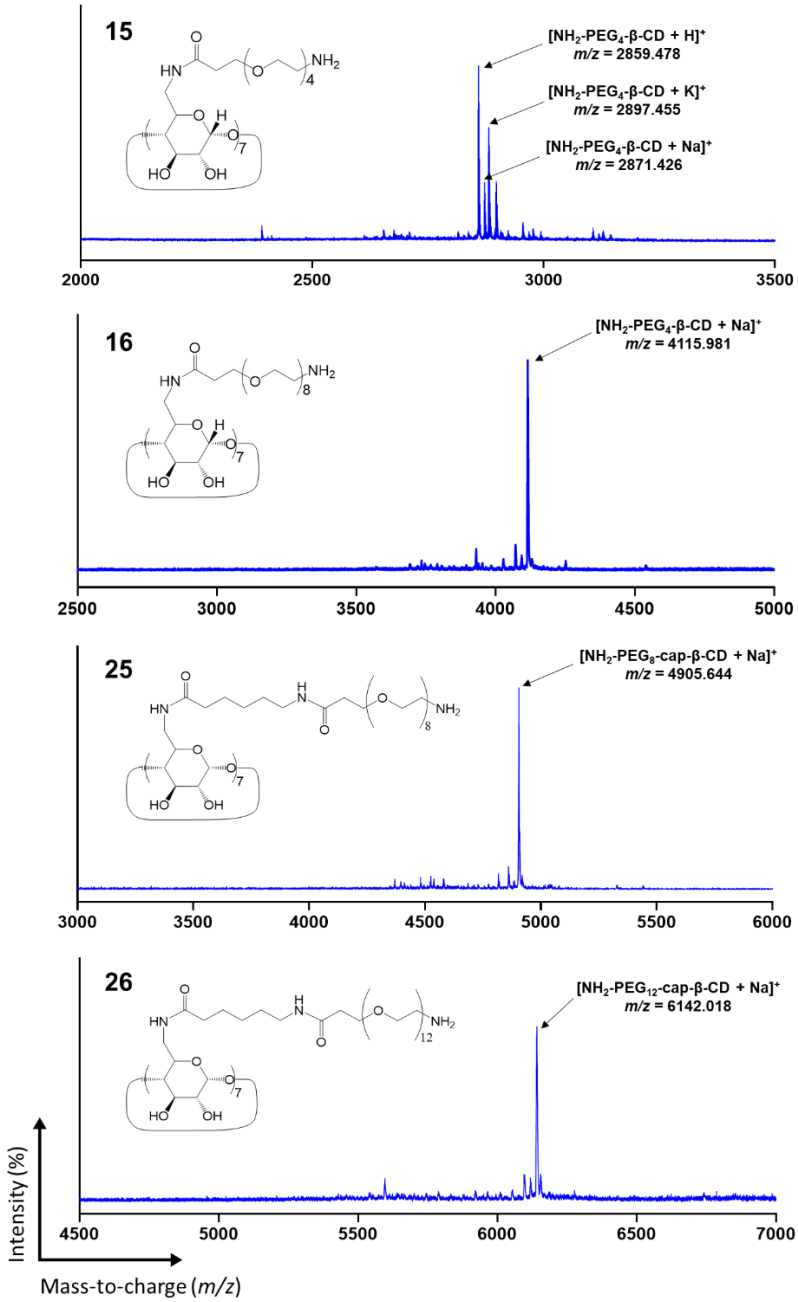

Figure 8. Matrix-assisted laser desorption/ionization time-of-flight (MALDI-TOF) spectra of CD intermediates conjugated with PEG (compounds **15** and **16**) or caproic acid-PEG spacers (compounds **25** and **26**) in the P2 position. Heptaconjugation of spacers was confirmed by the mass-to-charge ratio (*m/z*) of each CD derivative.

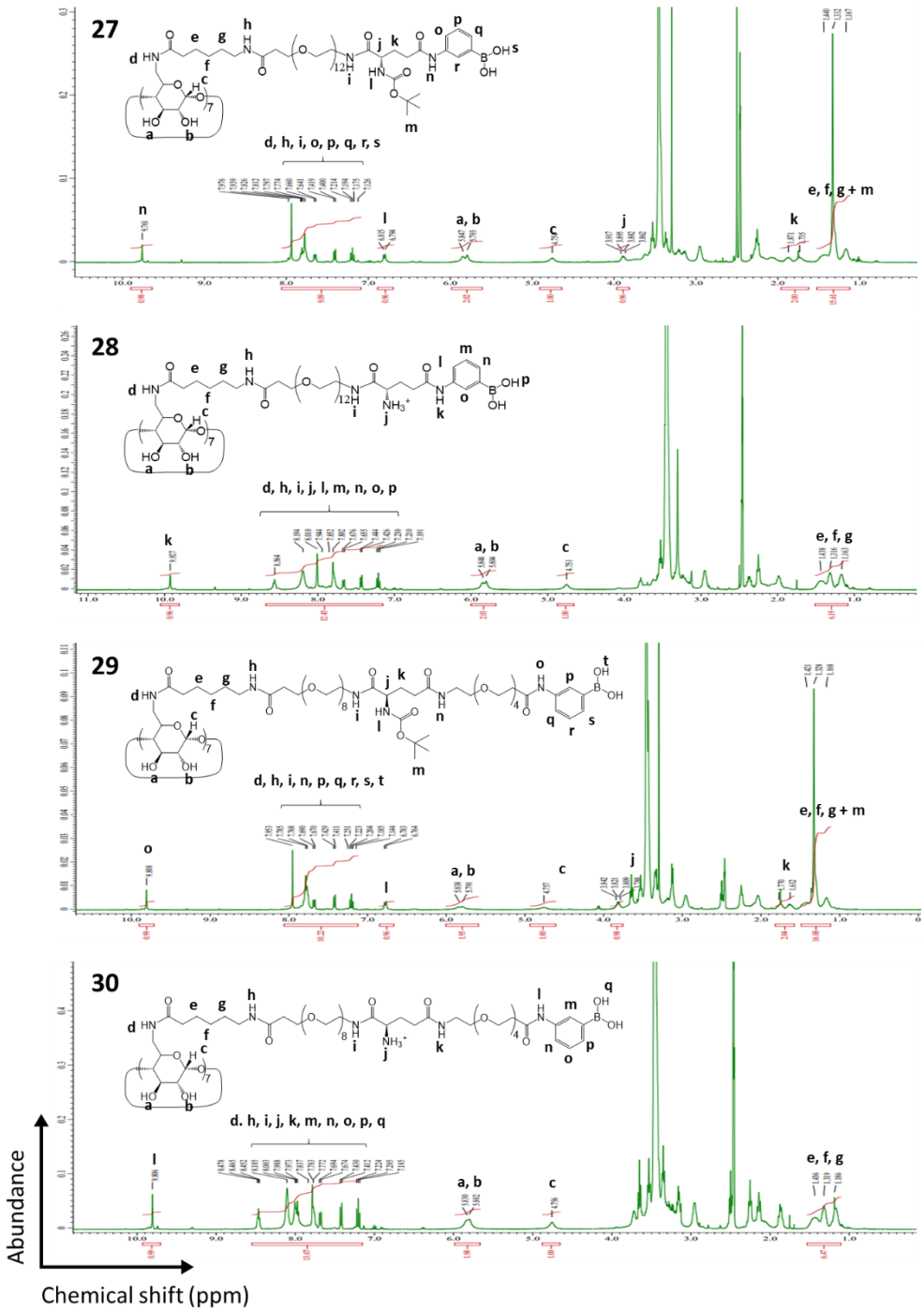

Figure 9. ^{1}H-NMR spectra of CD intermediates with the caproic acid-PEG spacer in the P2 position (compounds **27**, **28**, **29**, and **30**). Samples were dissolved in DMSO-d_6 for ^{1}H-NMR analysis.

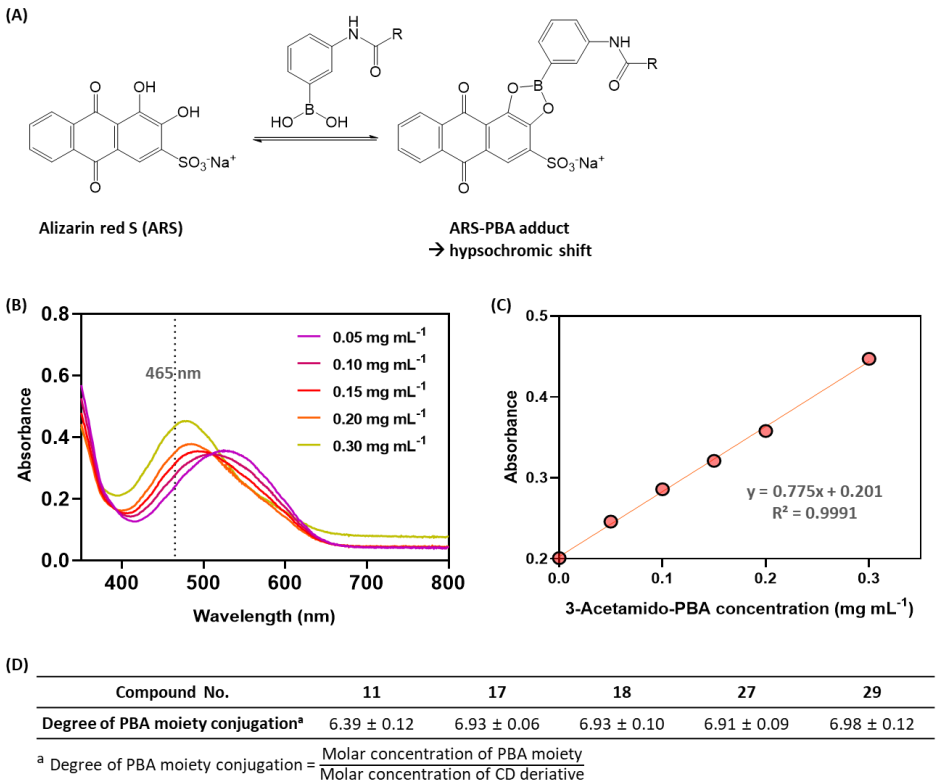

(D)

Compound No.	11	17	18	27	29
Degree of PBA moiety conjugation[a]	6.39 ± 0.12	6.93 ± 0.06	6.93 ± 0.10	6.91 ± 0.09	6.98 ± 0.12

[a] Degree of PBA moiety conjugation = $\frac{\text{Molar concentration of PBA moiety}}{\text{Molar concentration of CD deriative}}$

Figure 10. (A) Degree of PBA moiety conjugation was determined based on alizarin red S (ARS)–PBA moiety interaction. (B) Upon increasing PBA concentration, the absorption spectrum of ARS was blue-shifted by forming the ARS–PBA adduct. (C) A linear relationship was observed between the ARS absorbance at 465 nm and standard (3-acetamido-PBA) concentration within 0.05–0.30 mg mL^{-1}. (D) Degree of PBA moiety conjugation of compounds **11**, **17**, **18**, **27**, and **29** was approximately 7, indicating heptaconjugation of CD arms.

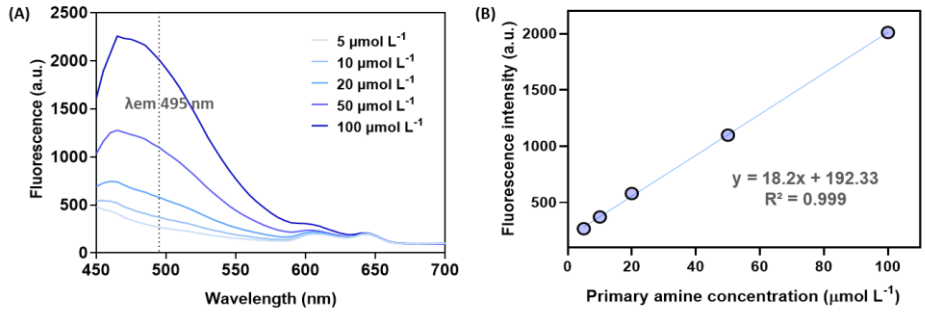

(C)

CD derivative No.	CD 16	CD 17	CD 18	CD 19	CD 20
Charged moiety conjugation (%)[a]	99.27 ± 0.033	98.94 ± 0.14	99.86 ± 0.038	98.86 ± 0.075	98.81 ± 0.074

[a] Charged moiety conjugation (%) = $\frac{\text{Molarity of CD derivative} \times 7 - \text{Molarity of unreacted primary amine}}{\text{Molarity of CD derivative} \times 7} \times 100\ (\%)$

Figure 11. Percentage of charged moiety conjugation was determined by quantifying the residual amines *via* fluorescamine assay. (A) Fluorescence spectra of fluorescamine at various concentrations of L-serine (5–100 μmol L^{-1}). (B) Calibration curve was obtained by measuring the fluorescence intensity at $\lambda_{ex}/\lambda_{em}$ of 395/495 nm. (D) Charged moiety conjugation of **CD 16–20** was higher than 98.8%, indicating complete conjugation.

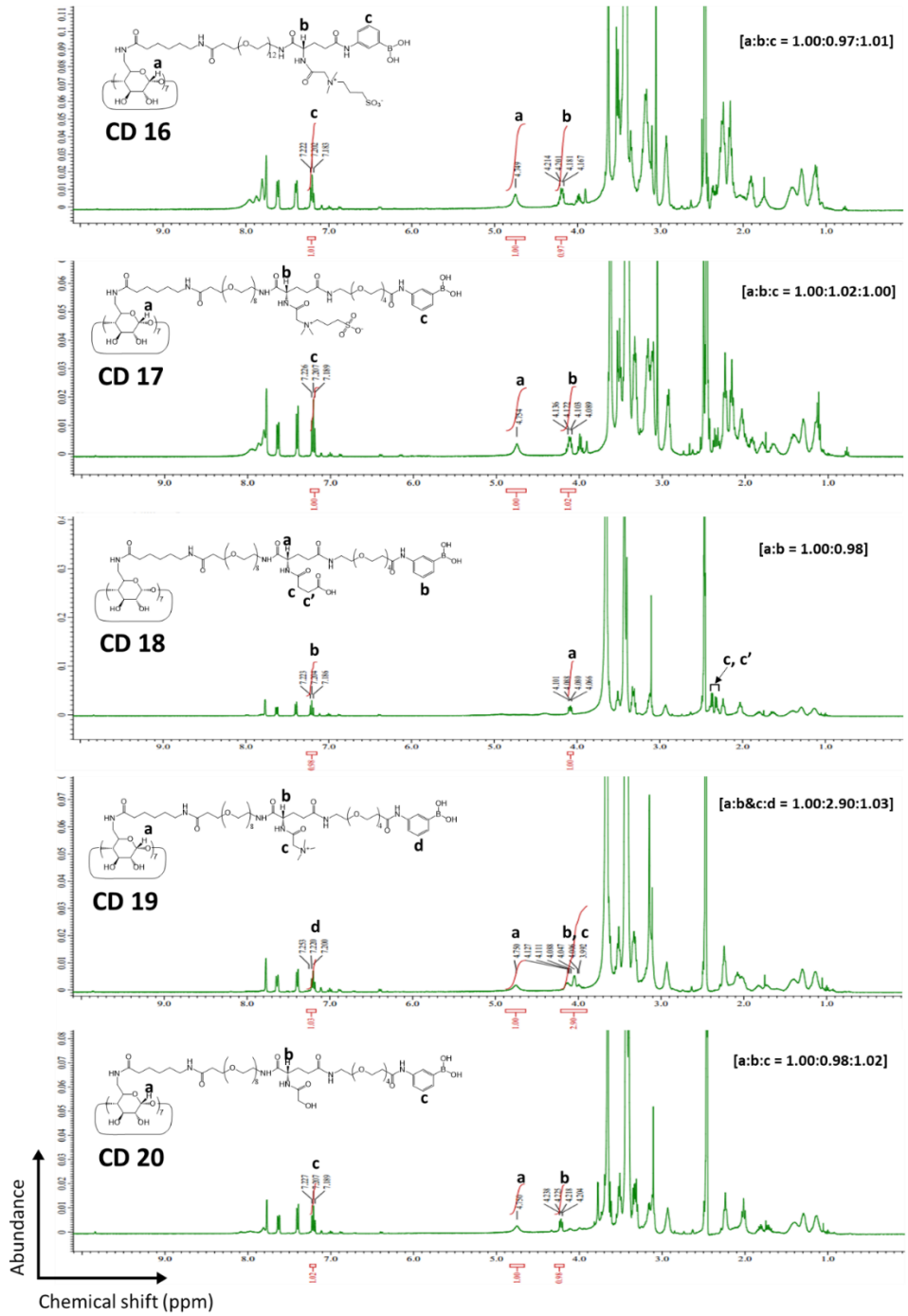

Figure 12. ^{1}H-NMR spectra of **CD16–20**. Samples were dissolved in DMSO-d_6/D_2O (9:1, v/v). Signal of Glu α-position proton appeared at 4.1–4.2 ppm.

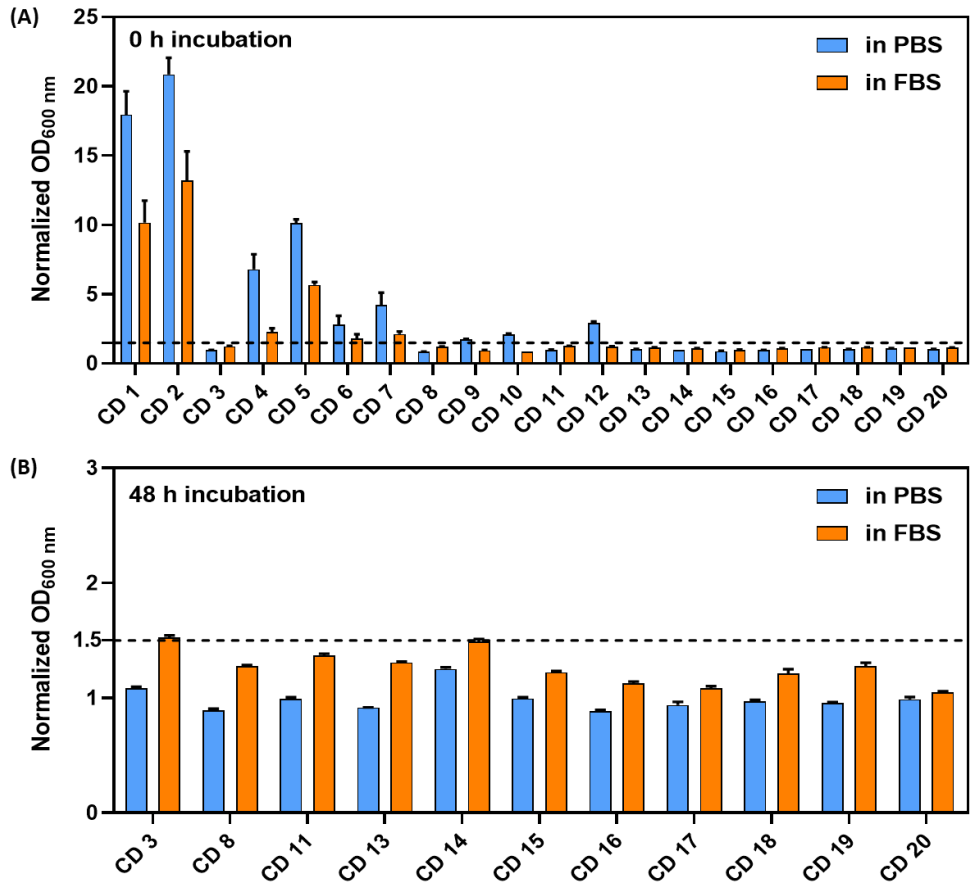

Figure 13. Solubility screening of CD derivatives *via* turbidimetric analysis. Normalized absorbance values at 600 nm ($OD_{600\ nm}$) of CD derivatives were measured after 0 h (A) or 48 h (B) incubation in PBS or FBS at a **CD 1–20** concentration of 1 mmol L^{-1}. The cut-off value of $OD_{600\ nm}$ for judging precipitation or aggregation was set at 1.5 (dashed line).

	P1	P2	P3
CD 1	A_1		
CD 2	A_2		
CD 3	B		
CD 4	C		
CD 5	D		
CD 6	A_1	F_4	
CD 7	A_2	F_4	
CD 8	B	F_4	
CD 9	C	F_4	
CD 10	D	F_4	
CD 11	A_1	F_8	
CD 12	A_2	F_8	
CD 13	B	F_8	
CD 14	C	F_8	
CD 15	D	F_8	
CD 16	A_1	F_{12}	
CD 17	A_1	E-F_8	F_4
CD 18	B	E-F_8	F_4
CD 19	C	E-F_8	F_4
CD 20	D	E-F_8	F_4

Insoluble in FBS and PBS
Soluble in FBS, insoluble in PBS
Soluble in FBS and PBS

Figure 14. Relationship between CD structure and colloidal stability. Turbidimetry-based solubility test was performed on CD derivatives dispersed in FBS or PBS at 1 mmol L^{-1} concentration.

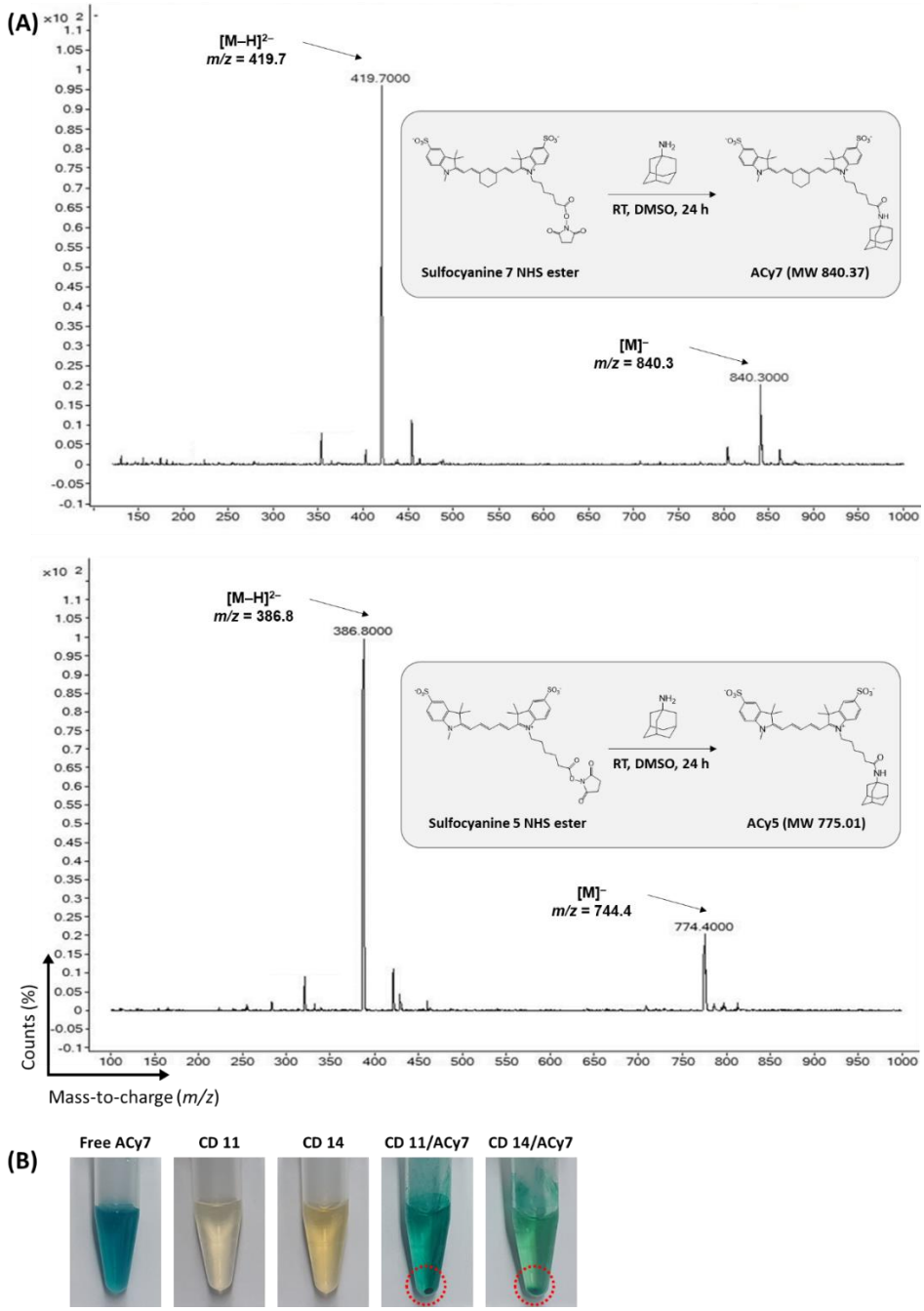

Figure 15. (A) Synthetic schemes and ESI-MS spectra of adamantyl sulfocyanine (ACy)-7 and ACy5. (B) Visual appearance of free ACy7, **CD 11**, **CD 14**, and their inclusion complexes. Both **CD 11** and **14** exhibited precipitation in the presence of ACy7 (dashed circles). Concentrations of ACy7 and CD derivatives were both 200 μmol L^{-1} in all samples.

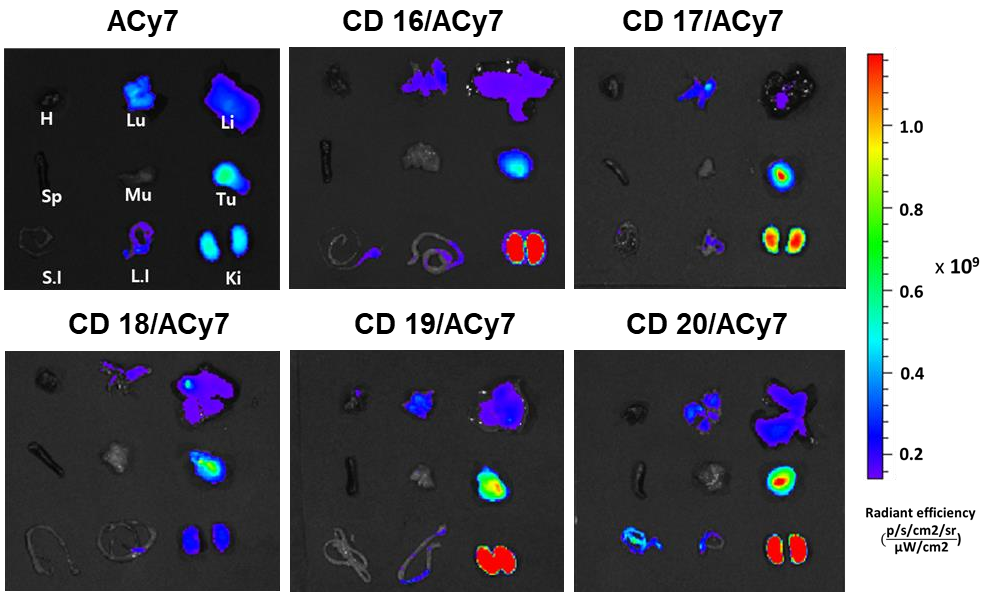

Figure 16. Biodistribution of **CD 16–20**/adamantyl sulfocyanine 7 (ACy7) inclusion complexes. *Ex vivo* near-infrared fluorescence (NIRF) images of tumors and major organs resected from HT-29 tumor-bearing mice 24 h after the intravenous injection of free ACy7 or inclusion complexes. Abbreviations: H, heart; Lu, lungs; Li, liver; Sp, spleen; Mu, muscle; Tu, tumor; S.I, small intestine; L.I, large intestine; and Ki, kidneys.

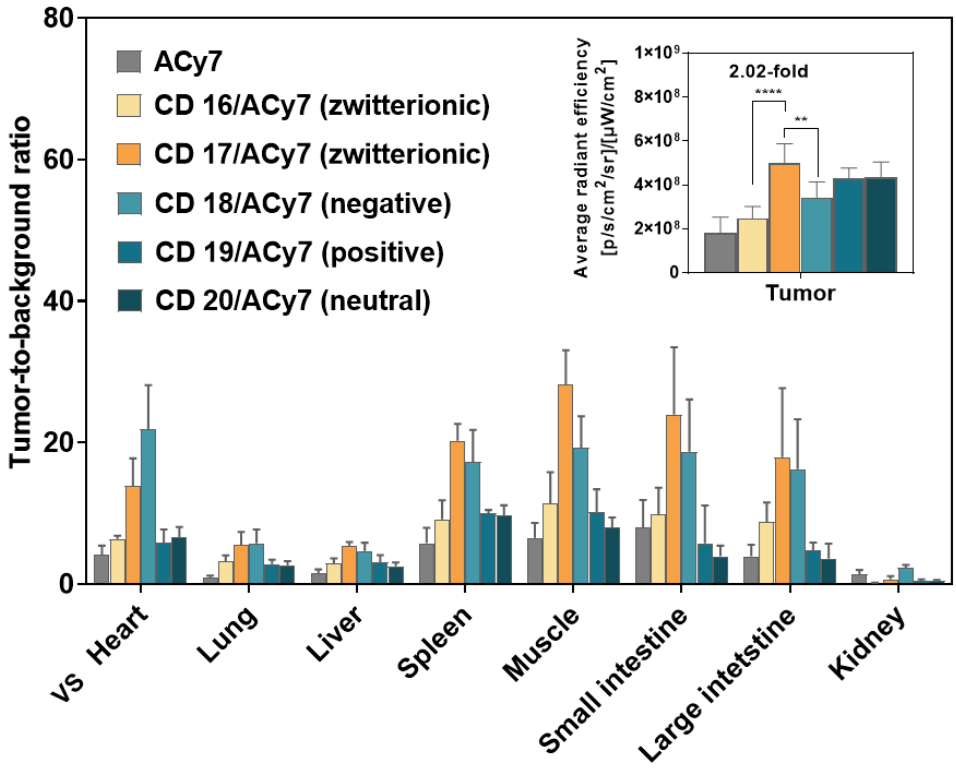

Figure 17. Tumor-to-background ratios of **CD 16–20**/ACy7 in each organ. Radiant efficiency values in tumor tissues are presented in the inset.

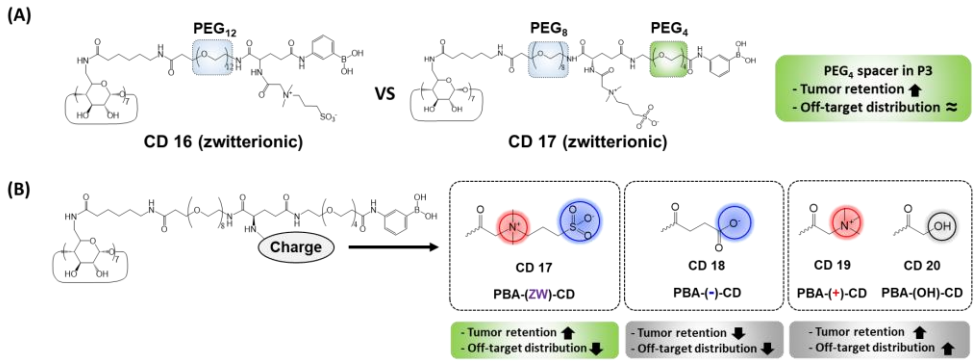

Figure 18. (A) Addition of the PEG_4 spacer in the P3 position significantly improved the tumor accumulation of zwitterionic CD derivatives, presumably reducing the interference of sulfobetaine in PBA–target interactions. (B) Among four differently charged CD derivatives, only the zwitterionic CD derivative (**CD 17**, PBA-(ZW)-CD) exhibited enhanced tumor retention and reduced off-target accumulation simultaneously.

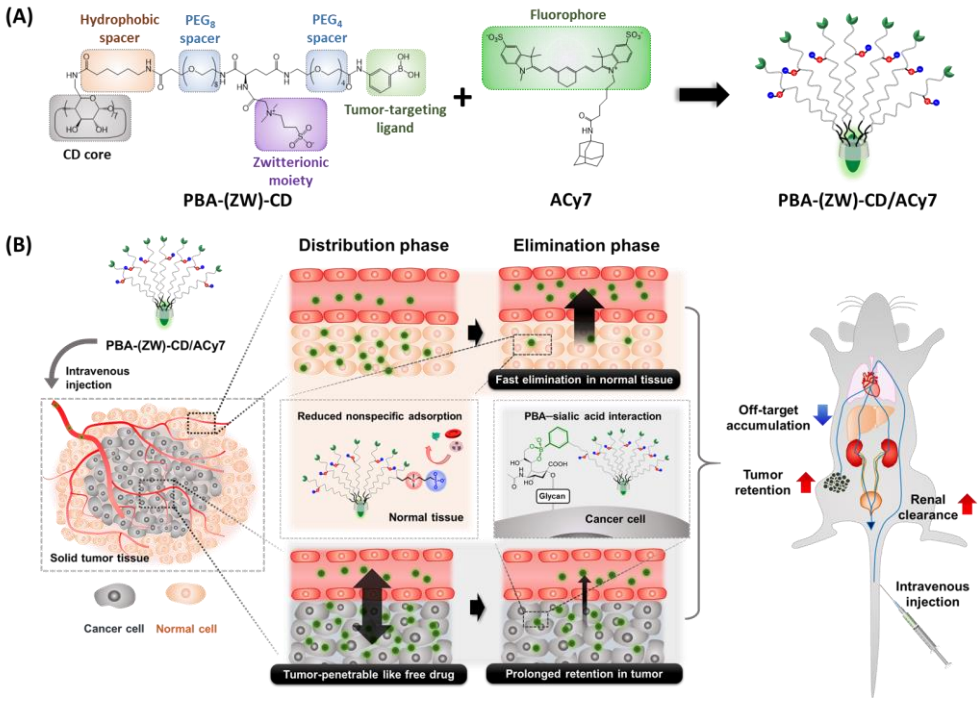

Figure 19. (A) Structural components of PBA-(ZW)-CD/ACy7, including hydrophobic linker (caproic acid), PEG spacers, zwitterionic moiety (sulfobetaine), and tumor-targeting ligand (PBA). (B) Schematic illustration of the *in vivo* behavior of PBA-(ZW)-CD/ACy7 accounting for enhanced tumor retention and reduced off-target accumulation.

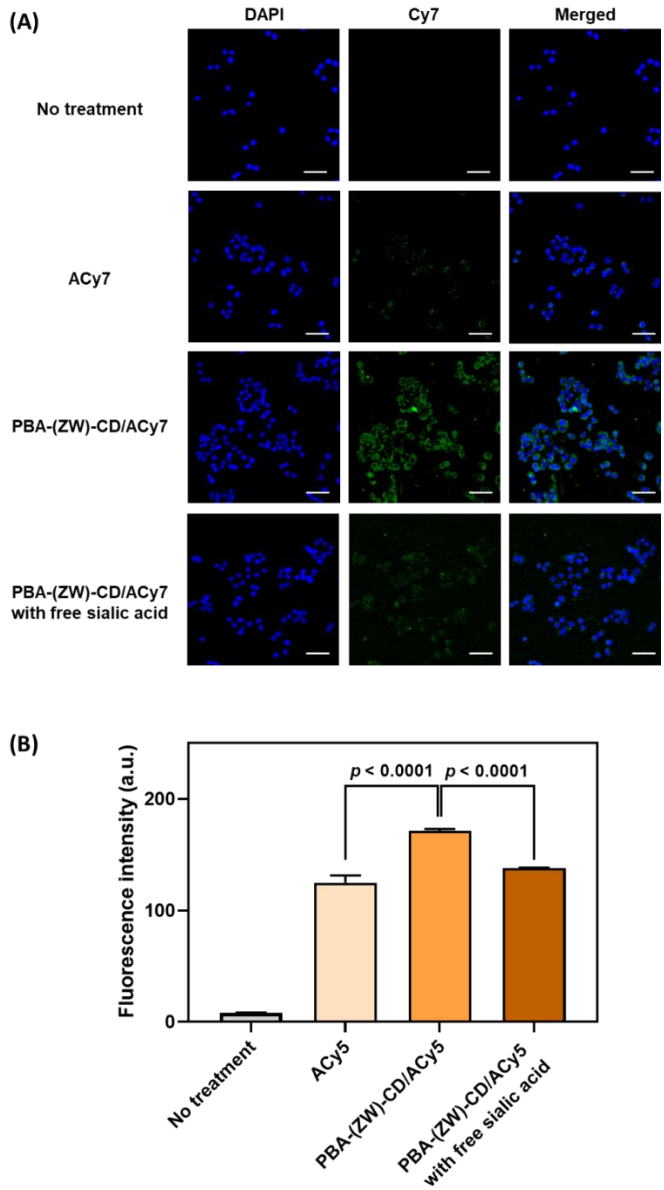

Figure 20. Cellular uptake of PBA-(ZW)-CD inclusion complexes. (A) Fluorescence images of HT-29 cells after 2 h incubation with ACy7 or PBA-(ZW)-CD/ACy7 at an ACy7 concentration of 10 μmol L^{-1}. The length of the scale bar is 50 μm. (B) Flow cytometry analysis of HT-29 cells incubated with ACy5 or PBA-(ZW)-CD/ACy5 for 2 h at an ACy5 concentration of 10 μmol L^{-1}. Free sialic acid (500 μmol L^{-1}) was used in both assays as a competitive inhibitor for PBA–sialic acid interaction.

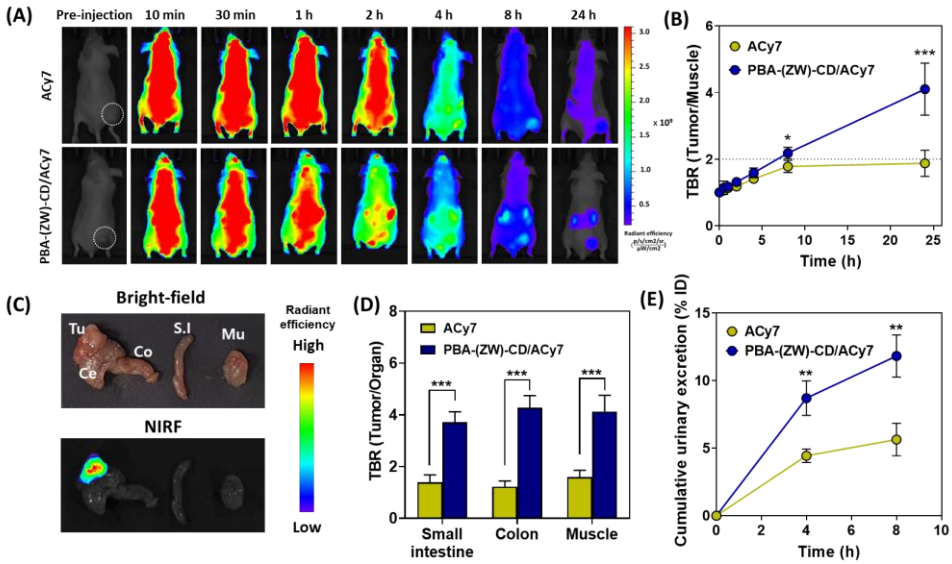

Figure 21. Tumor targetability and urinary excretion of PBA-(ZW)-CD/ACy7. (A) *In vivo* real-time NIRF imaging after intravenous administration of ACy7 or PBA-(ZW)-CD/ACy7 to heterotopic (subcutaneous) HT-29 tumor-bearing mice (dashed circles indicate tumors) and (B) corresponding time-course changes in the tumor-to-background ratio (TBR). Data are presented as the mean ± standard deviation (SD) (n = 4). (C) *Ex vivo* NIRF images of HT-29 tumors (located at cecum [Ce] wall, colon [Co], small intestine [S.I], and muscle [Mu]), resected from orthotopic (subserosal) HT-29 tumor-xenografted mice 24 h after the intravenous injection of PBA-(ZW)-CD/ACy7. (D) TBR was measured in the colon, small intestine, and muscle tissues. Data are presented as the mean ± SD (n = 4). (E) Cumulative urinary excretion (% ID) of free ACy7 and PBA-(ZW)-CD/ACy7. Data are presented as the mean ± SD (n = 3). *p < 0.05, **p < 0.01, and ***p < 0.001.

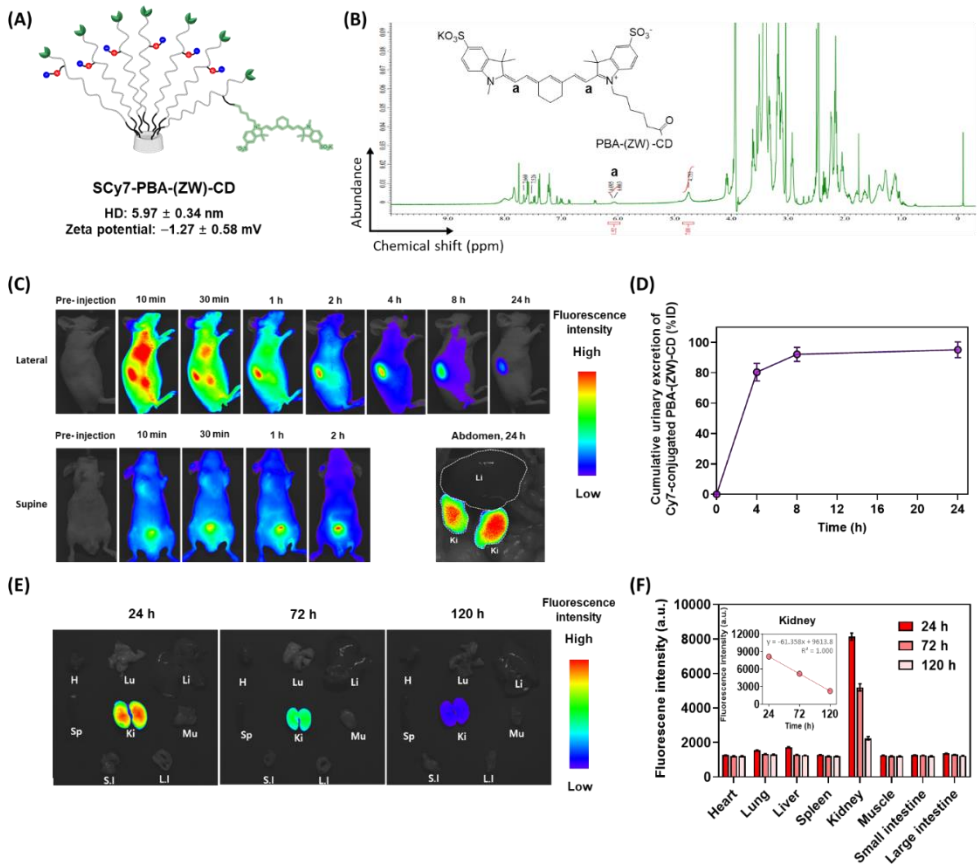

Figure 22. Real-time tracing of PBA-(ZW)-CD after intravenous injection. SCy7-NHS (1 equiv.) was conjugated to one arm of compound **30**, and sulfobetaine was conjugated to the remaining six arms following the *General procedure for sulfobetaine conjugation* to obtain a SCy7-conjugated **CD 17** derivative (SCy7-PBA-(ZW)-CD). (A) SCy7-PBA-(ZW)-CD displayed hydrodynamic diameter (HD) and zeta potential values comparable to those of PBA-(ZW)-CD. (B) ^{1}H-NMR analysis of SCy7-PBA-(ZW)-CD was performed in DMSO-d_6/D_2O (9:1, v/v). (C) SCy7-PBA-(ZW)-CD (1 μmol kg^{-1}) was intravenously administered to male BALB/c nude mice (5 weeks old), and near-infrared fluorescence (NIRF) imaging was performed according to the method described in *2.3. biodistribution studies of CD derivatives.* In lateral view images, as the whole-body fluorescence signals gradually decreased, the kidney signals became dominant. Meanwhile, supine view images revealed that the fluorescence intensity gradually increased in

the bladder, implying the renal excretion of SCy7-PBA-(ZW)-CD. (D) Cumulative urinary excretion of SCy7-PBA-(ZW)-CD exceeded 80% of the initial dose (ID) within 4 h, reaching 95.2 ± 5.2% ID at 24 h, suggesting the preferential renal clearance of PBA-(ZW)-CD. (E) In an *ex vivo* imaging study, the SCy7-PBA-(ZW)-CD signal was mainly observed in the kidneys with negligible signals (*i.e.*, autofluorescence level) detected in other organs, including the lungs, liver, and spleen at 120 h. Abbreviations: H, heart; Lu, lungs; Li, liver; Sp, spleen; Mu, muscles; S.I, small intestine; L.I, large intestine; and Ki, kidneys. (F) Kidney signals also decreased linearly (fluorescence intensity (a.u.) = –61.4 × elapsed time (h) + 9613.8; R^2 = 1.000), expected to reach the autofluorescence level within 136.3 h. Collectively, these results indicate that PBA-(ZW)-CD structure can evade mononuclear phagocyte system uptake (reduced distribution to the liver, lungs, and spleen), minimize the non-specific tissue binding, and be readily excreted *via* kidneys.

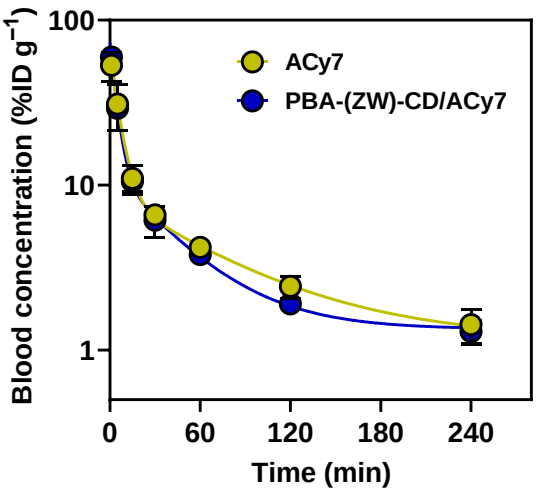

Figure 23. ACy7 blood concentration versus time profiles of free ACy7 and PBA-(ZW)-CD/ACy7 after intravenous administration at an ACy7 dose of 1 μmol kg^{-1}.

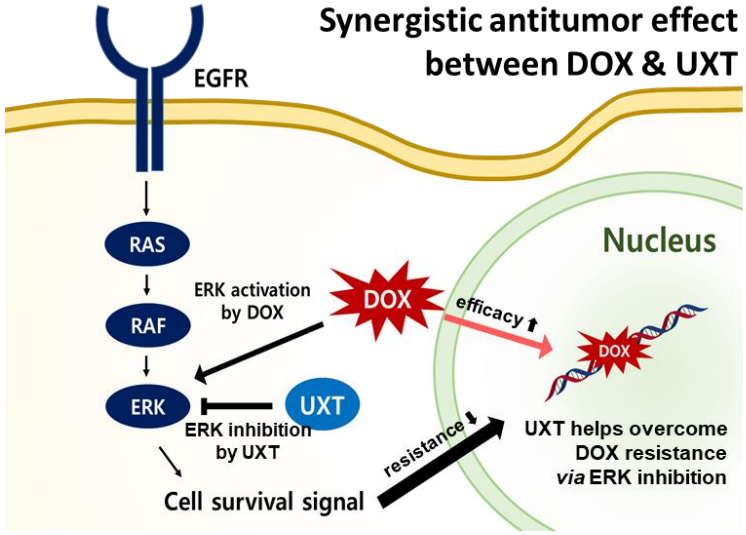

Figure 24. Schematic illustration of synergistic antitumor efficacy by DOX and UXT combination. UXT, a potent ERK inhibitor, may counteract the DOX-induced ERK activation and consequent drug resistance.

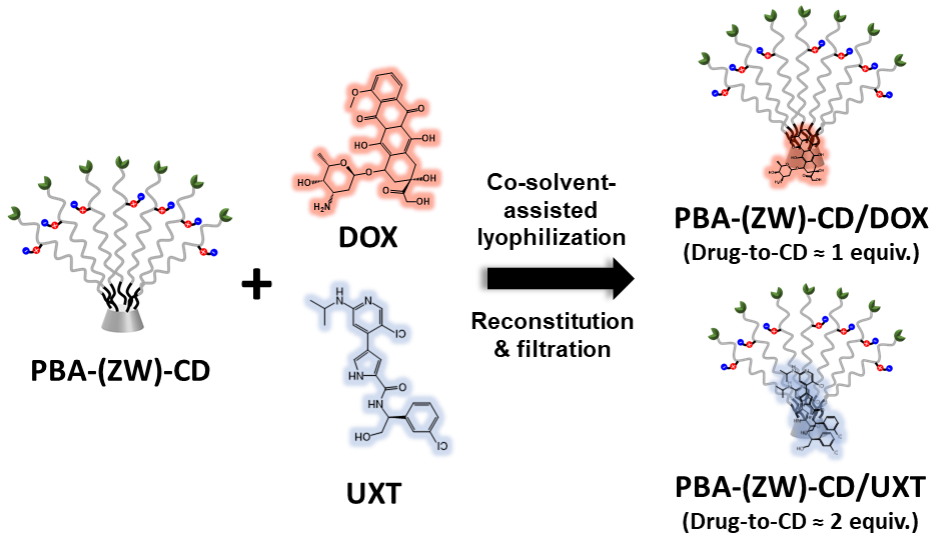

Figure 25. Preparation of PBA-(ZW)-CD/DOX and PBA-(ZW)-CD/UXT inclusion complexes via lyophilization.

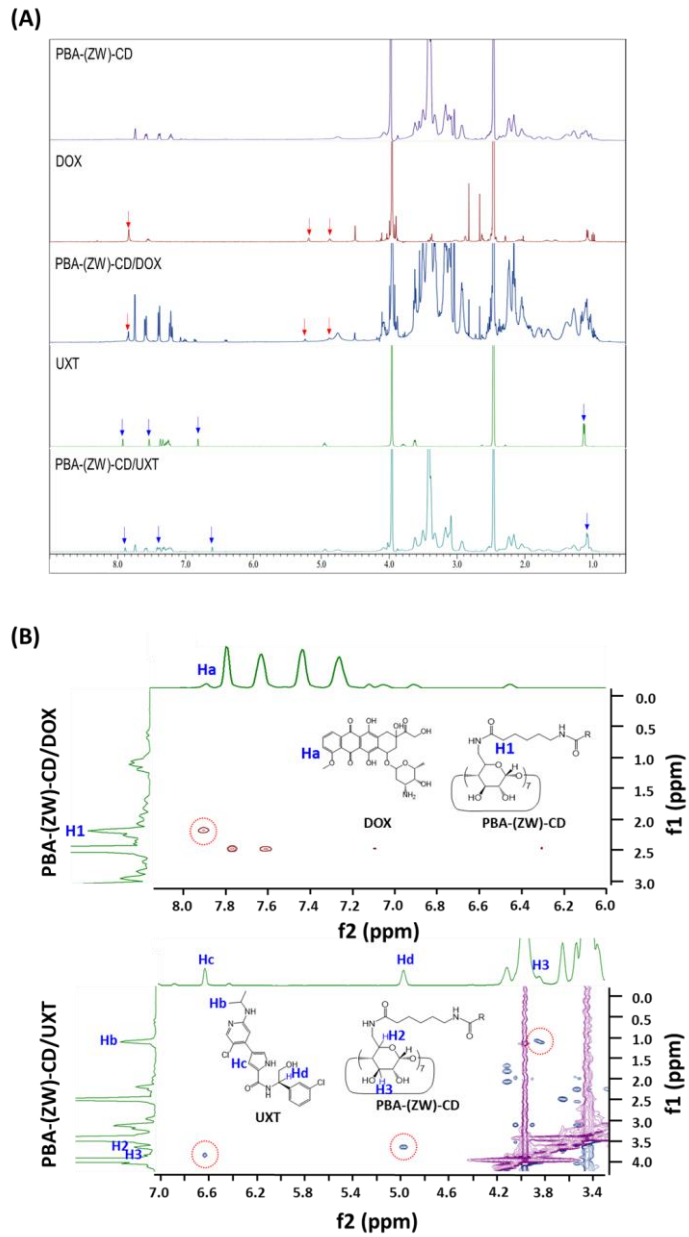

Figure 26. (A) Proton nuclear magnetic resonance (^{1}H-NMR) spectra of free drugs and inclusion complexes. Slight changes in the chemical shifts of DOX (red arrows) and UXT (blue arrows) were observed after complexation. All samples were dissolved in dimethyl sulfoxide (DMSO)-d_6/D_2O (80:20, v/v). (B) ROESY spectra of PBA-(ZW)-CD/DOX and PBA-(ZW)-CD/UXT in DMSO-d_6/D_2O (80:20, v/v). Dashed circles indicate dipolar couplings supporting the inclusion complex formation.

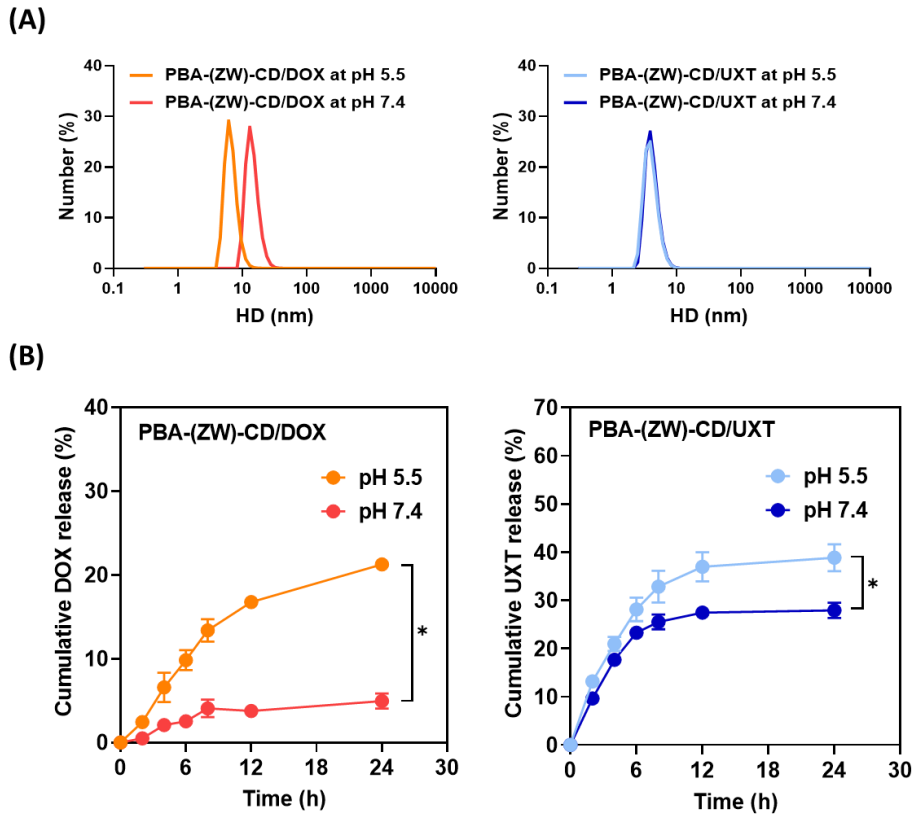

Figure 27. (A) Number-weighted size distribution of inclusion complexes at pH 5.5 and 7.4. (B) Drug release profiles of PBA-(ZW)-CD/DOX and PBA-(ZW)-CD/UXT inclusion complexes at pH 5.5 and 7.4 (n = 3, *p < 0.005).

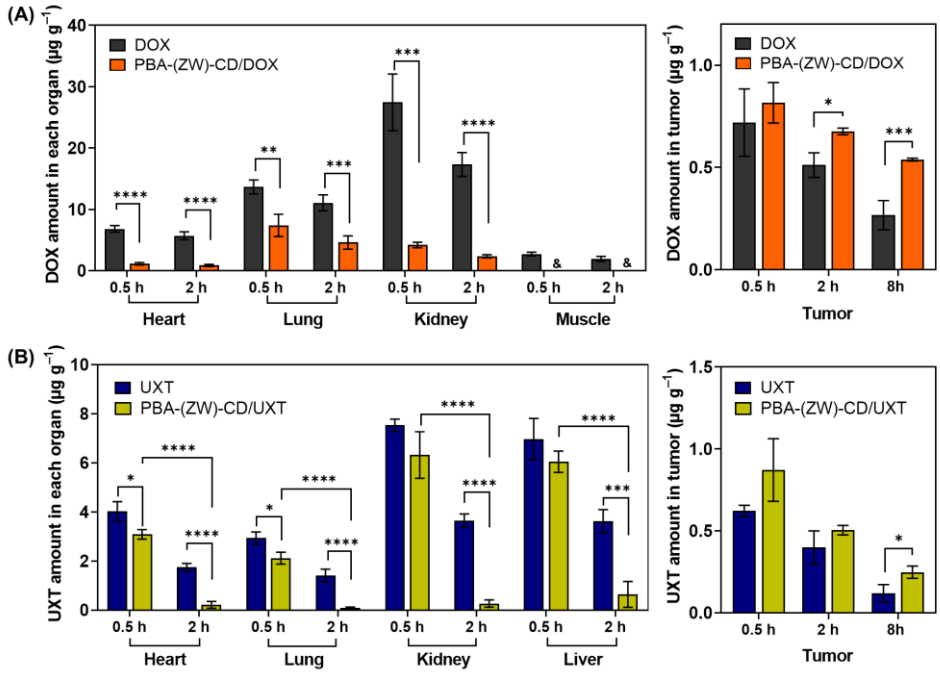

Figure 28. Biodistribution of PBA-(ZW)-CD/drug inclusion complexes. (A) DOX distribution in normal tissues related to drug adverse effects and tumor after the intravenous injection of DOX solution or PBA-(ZW)-CD/DOX at a DOX dose of 5 mg kg^{-1} (n = 3). (B) UXT distribution in normal tissues, including mononuclear phagocyte system (MPS)-rich organs, and tumor after the intravenous administration of UXT solution and PBA-(ZW)-CD/UXT at a UXT dose of 5 mg kg^{-1} (n = 3). [&] below the detection limit (< 200 ng g^{-1} tissue).

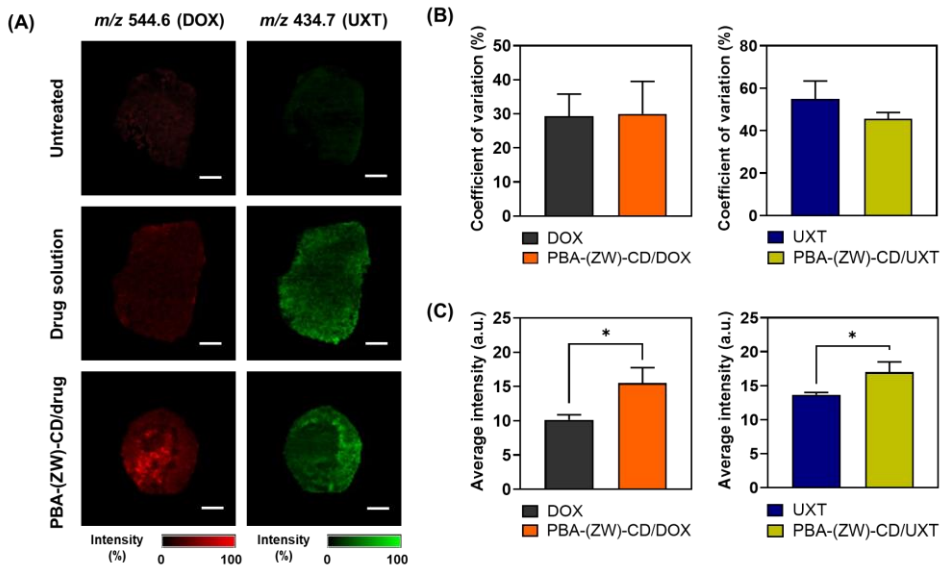

Figure 29. Intratumoral distribution of PBA-(ZW)-CD/drug inclusion complexes. (A) Matrix assisted laser desorption/ionization-mass spectrometry imaging (MALDI-MSI) study of tumor tissues dissected at 30 min post-injection of drug solution or PBA-(ZW)-CD/drug inclusion complex (n = 3). Intratumoral mass spectrometry (MS) signals corresponding to DOX (*m/z* 544.6, pseudocolored in red) and UXT (*m/z* 434.7, pseudocolored in green) are presented. The length of scale bar is 1 mm. The spatial signal distributions as coefficient of variation (B) and area-averaged signal intensity (C) were also evaluated *via* image analysis. *$p < 0.05$, **$p < 0.01$, ***$p < 0.005$, and ****$p < 0.001$.

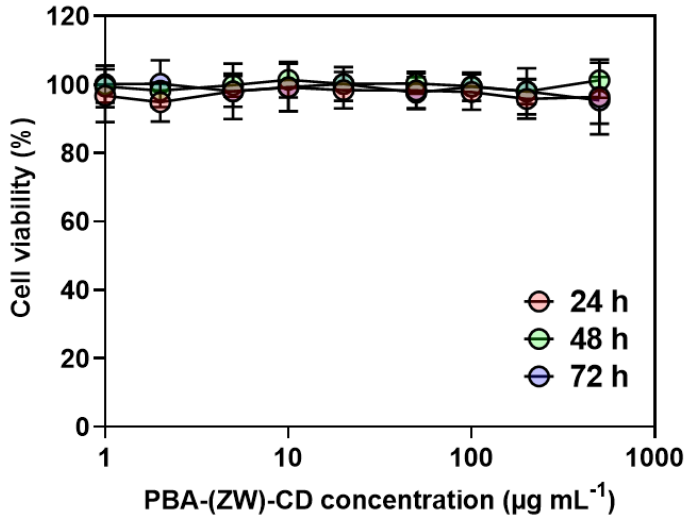

Figure 30. *In vitro* toxicity studies of blank PBA-(ZW)-CD. HT-29 cell viability after 24, 48, and 72 h incubation with PBA-(ZW)-CD at various concentrations (1–500 µg mL^{-1}).

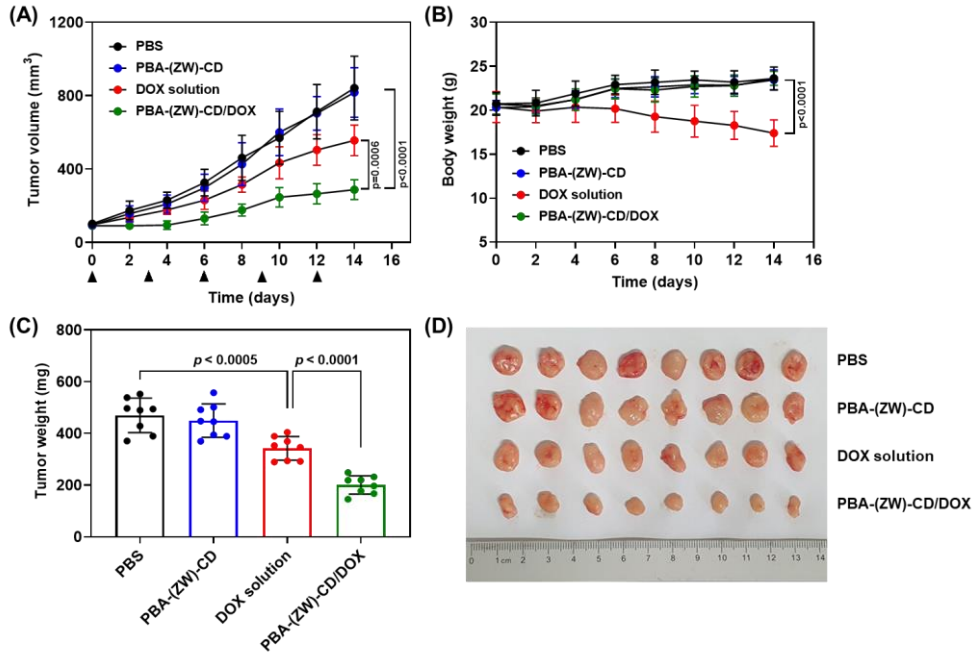

Figure 31. PBA-(ZW)-CD/doxorubicin (DOX)-assisted single-drug therapy in heterotopic HT-29 xenograft mice (n = 8). (A) Tumor growth profiles over 14 days. PBS, blank PBA-(ZW)-CD, DOX solution, or PBA-(ZW)-CD/DOX (as DOX, 5 mg kg^{-1}) was administered intravenously every three days. (B) Body weight of each mouse was monitored during the experimental period. (C) On day 14, the tumor tissues of mice were resected and weighed. (D) Digital images of excised tumors. Data are presented as mean values ± SD. Statistically significant differences were determined using ANOVA and Tukey's test.

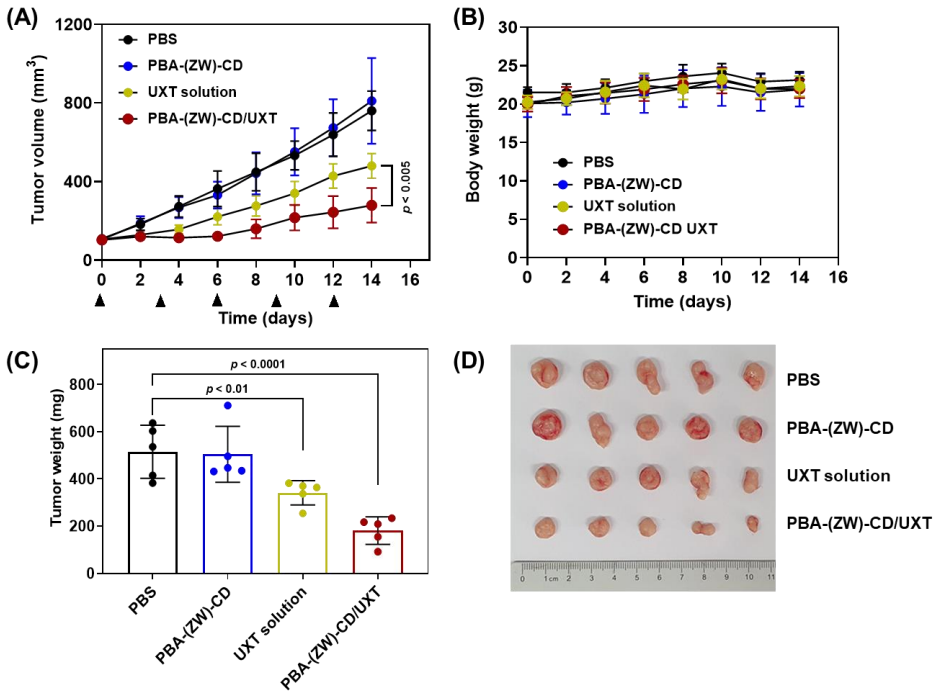

Figure 32. PBA-(ZW)-CD/UXT-assisted single-drug therapy in heterotopic HT-29 xenograft mice (n = 5). (A) Tumor growth profiles over 14 days. PBS, blank PBA-(ZW)-CD, UXT solution, or PBA-(ZW)-CD/UXT was intravenously administered at a UXT dose of 5 mg kg^{-1} every three days. (B) Body weight of each mouse was monitored every other day. (C) On day 14, the tumor tissues of mice were resected and weighed. (D) Digital images of excised tumors. Data are presented as mean values ± SD. Statistically significant differences were determined using ANOVA and Fisher's test.

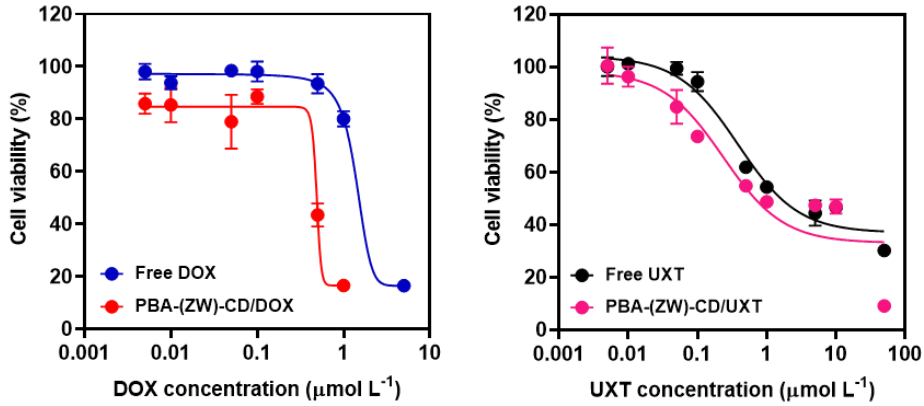

Figure 33. Cell viability profiles of free drug and PBA-(ZW)-CD/drug inclusion complexes in HT-29 cells at 48 h incubation. Data are presented as the mean ± SD (n = 6).

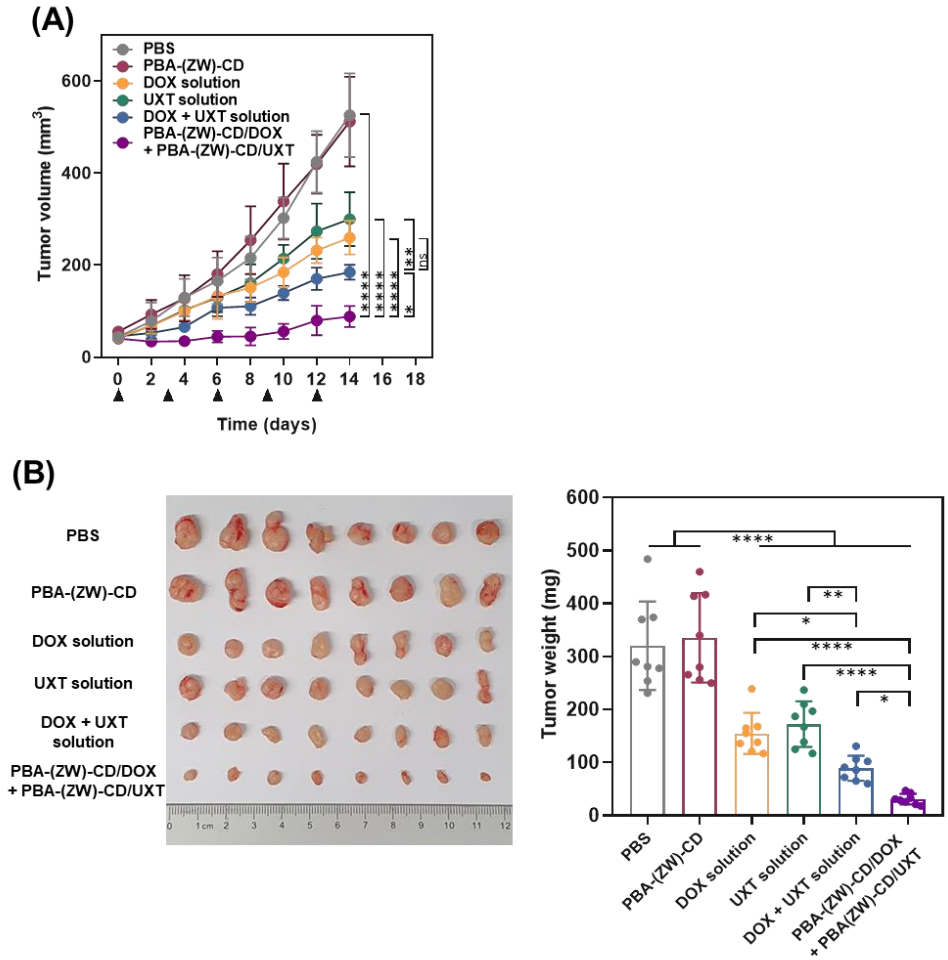

Figure 34. PBA-(ZW)-CD/drug-assisted combination therapy in colorectal cancer (CRC) models. (A) Tumor growth profile of heterotopic HT-29 xenograft mice treated with PBS, blank PBA-(ZW)-CD, DOX solution, UXT solution, DOX + UXT solution, or PBA-(ZW)-CD/DOX + PBA-(ZW)-CD/UXT (as drug, 3 mg kg^{-1} for each) intravenously every three days (n = 8). (B) On day 14, the tumor tissues were resected and weighed. Data are presented as the mean ± SD. *p < 0.05, **p < 0.01, ***p < 0.005, and ****p < 0.001. ^{ns}p > 0.05, not significant.

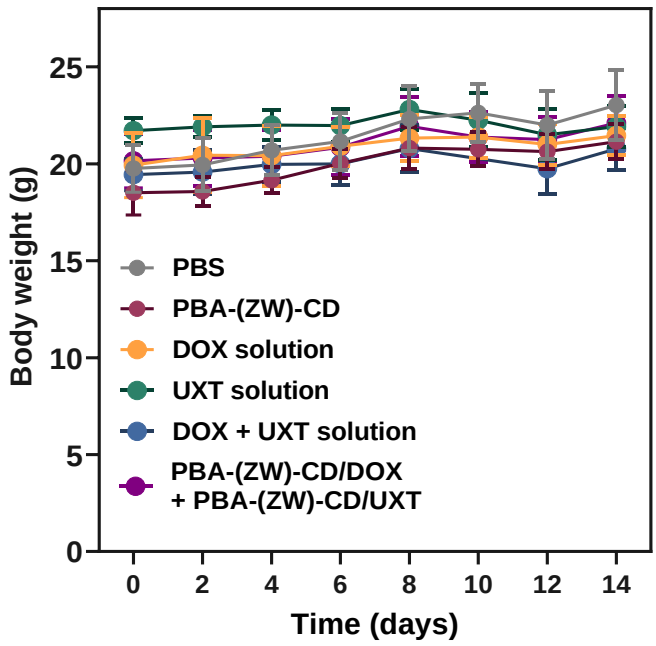

Figure 35. Body weight changes of heterotopic HT-29 xenograft mice during the experimental period (n = 8).

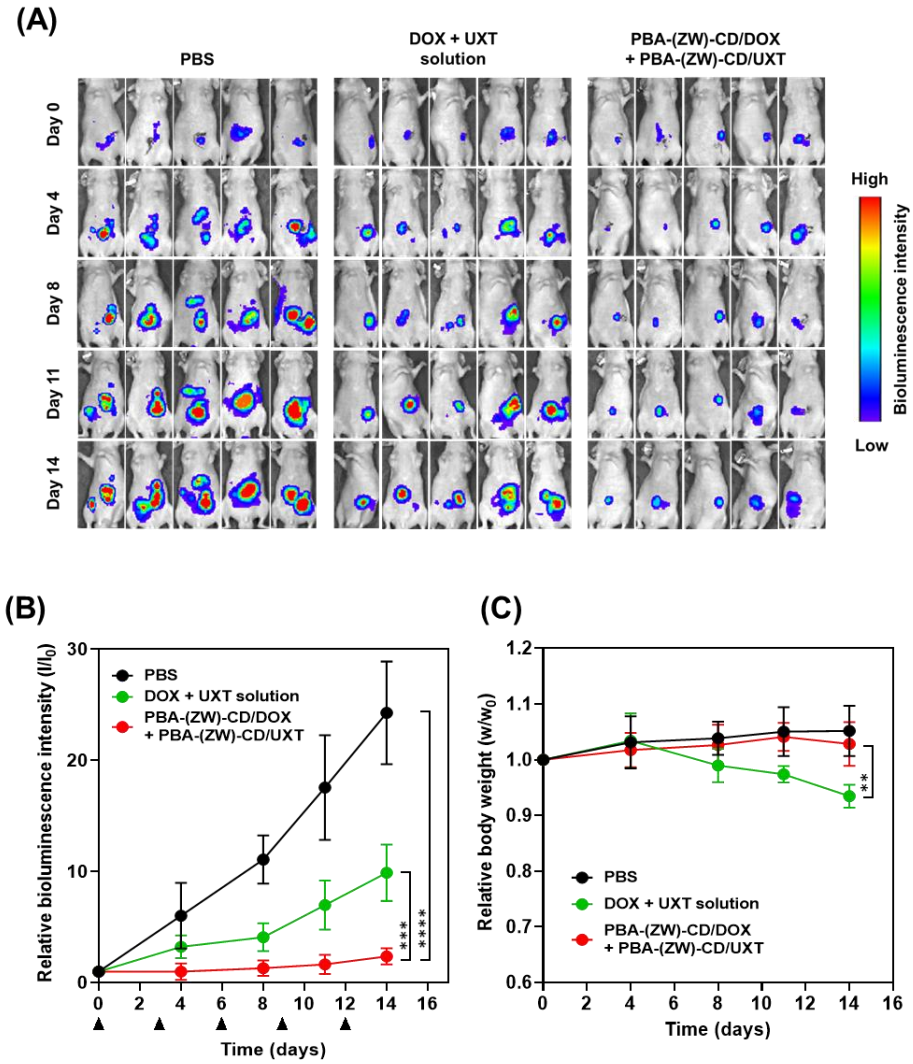

Figure 36. (A) *In vivo* bioluminescence images of orthotopic CRC model prepared via the inoculation of HT-29/Luc cells into BALB/c nude mice (n = 5). (B) Relative bioluminescence intensity (I/I_0; compared to day 0) vs. time profile of PBS, DOX + UXT, and PBA-(ZW)-CD/DOX + PBA-(ZW)-CD/UXT groups. Mice were intravenously administered with each intervention (as drug, 3 mg kg^{-1} for each) every three days. (C) Body weight change of each mouse was recorded. Data are presented as the mean ± SD. *p < 0.05, **p < 0.01, ***p < 0.005, and ****p < 0.001. ^{ns}p > 0.05, not significant.

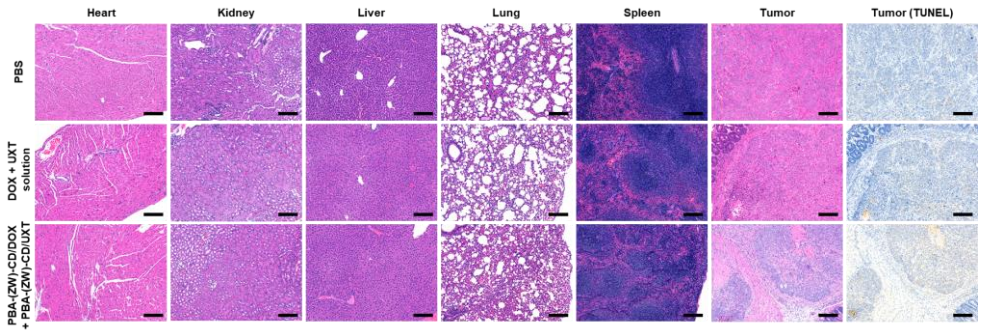

Figure 37. Hematoxylin and eosin (tumor and organs) and terminal deoxynucleotidyl transferase dUTP nick-end labeling (TUNEL; tumor) staining images of tissues dissected on day 14. The length of the scale bar is 200 μm.

국문초록

종양 표적화 항암제 전달 시스템은 항암제를 선택적으로 종양에 전달하기 위해 고안된 제형으로써, EPR(Enhanced permeability and retention) 효과가 발견된 이래로 이 효과를 활용할 수 있는 10-200 nm 크기의 나노 제형을 중심으로 연구되어 왔다. 그러나 최근에 EPR 이론을 기반으로 설계된 나노 제형들의 종양 표적 효율이 약물 수용액에 비해 유의미하게 높지 않으며, 오히려 고전적인 나노 제형의 크기가 비표적 조직에 대한 나노 제형의 축적을 유발한다는 사실이 보고되었다. 나노 제형의 비표적 축적(Off-target accumulation)은 나노 제형이 종양으로 분포하는 것을 저해할 뿐만 아니라 장기적인 독성 문제를 야기하기 때문에 신규 나노 제형의 임상 적용을 저해하는 주요 요인으로 알려져 있다. 따라서 종양 표적화 나노 제형의 임상 적용 가능성을 높이기 위해서는 고전적인 나노 제형의 낮은 종양 표적 효율과 비표적 효과를 극복하는 것이 중요하며, 이를 위해 EPR 이론 기반의 나노 제형 설계 패러다임을 벗어난 새로운 제형 설계 전략이 필요하다. 본 연구의 목적은 나노 약물 전달체의 구조 최적화를 통해 종양 표적 효율을 높임과 동시에 비표적 효과를 최소화할 수 있는 항암제 전달 시스템을 합성하고 평가하는 것이었다. 비표적 효과의 주요 원인인 Mononuclear Phagocyte System (MPS)를 효과적으로 회피하기 위해 신장 배설 가능한 크기(<8 nm)인 베타-사이클로덱스트린 기반의 나노제형을

고안하였으며, 나노제형의 종양 표적 효율을 높이기 위해서 종양 표적화 잔기로써 Phenylboronic acid 작용기를 도입하였다. 가장 이상적인 생체 분포를 가지는 종양 표적화 나노 제형을 선별하기 위해 총 20 가지의 베타-사이클로덱스트린 유도체를 합성하였다. 20 가지 유도체 중에서 수용액 상에서의 안정성이 높으며 크기가 비슷한 5 가지 베타-사이클로덱스트린 유도체 (CD16-20)를 선별하였으며, 이 유도체들을 대상으로 대장암 종양 이종 이식 마우스 모델에서 생체 분포 평가를 시행하였다. 베타-사이클로덱스트린 유도체의 Linker 구조에 따라 포접된 형광 물질 (ACy7)은 상이한 생체 분포를 보였으며, 형광 물질의 종양 분포를 높임과 동시에 비표적 효과를 감소시킨 CD17 (PBA-(ZW)-CD)를 최적의 유도체로 선정하였다. PBA-(ZW)-CD에 형광 물질을 포접한 경우에 orthotopic CRC mouse model에서 3.7 이상의 tumor-to-background ratio를 보였으며, 이는 임상적으로 종양 진단 시 필요한 contrast index (2 - 2.5)를 크게 상회하는 수치이다. PBA-(ZW)-CD의 항암제 전달 효율을 평가하기 위해서 소수성 항암제인 doxorubicin과 ulixertinib을 PBA-(ZW)-CD에 각각 포접하여 포접화합물을 제조하였다. 제조된 포접화합물과 약물 수용액을 각각 대장암 종양 이종 이식 마우스 모델에 투여한 후 약물의 생체 분포를 비교하였다. PBA-(ZW)-CD에 포접된 소수성 항암제들의 종양 잔류는 항암제 용액 투여군보다 유의미하게 더 높은 반면, 정상 장기에서의 항암제 제거는 촉진되어 비표적 잔류가 더 낮은 양상을 보였다. 또 PBA-(ZW)-CD/약물 포접화합물은 작은 크기에 의해 종양

심부로의 침투가 약물 수용액만큼 효율적임을 확인하였다. 최종적으로 대장암 종양 이종 이식 마우스 모델에서 PBA-(ZW)-CD/약물 포접화합물의 항암화학치료효과를 평가하였으며, 항암제 용액 투여군 대비 향상된 종양 억제 효과와 낮은 전신 독성을 확인하였다. 종합적으로, 신장으로 배설 가능한 크기의 나노 제형에서 구조 최적화를 통하여 항암제의 종양 저류를 상승시킴과 동시에 비표적잔류를 감소시킬 수 있는 생체 적합한 나노 약물 전달체를 확립할 수 있었다. 본 연구에서 제시된 종양 표적화 나노 제형의 설계 전략은 고전적인 나노 제형의 한계점들을 극복하고 임상 적용 가능한 나노 제형을 설계하는데 유용하게 적용될 수 있을 것이라 생각된다.

주요어: 베타-사이클로덱스트린, 신장 배설, 양쪽이온성, 종양 저류, 비표적 축적, 대장암

학 번: 2017-24147